IGNITION IN SOLID ENERGETIC MATERIALS DUE TO ELECTRICAL DISCHARGE

Dr. Richard J. Lee

19970320 001

REPORT DOCUMENTATION PAGE

Public reporting burden for this collection of information is estimated to average 1 hour per response, including the time for reviewing instructions, searching existing data sources, gathering and maintaining the data needed, and completing and reviewing the collection of information. Send comments regarding the burden estimate or any other aspect of this collection of information, including suggestion for reducing this burden, to Washington Headquarters Services, Directorate for Information Operations and Reports. 1215 Jefferson Davis Highway, Suite 1204, Arlington, VA 22202-4302, and to the Office of Management and Budget, Paperwork Reduction project (0704-0188), Washington, DC 20503.

1. AGENCY USE ONLY (Leave Blank)	2. REPORT DATE 25 October 1996	3. REPORT TYPE AND DATES COVERED Final Report

4. TITLE AND SUBTITLE

IGNITION IN SOLID ENERGETIC MATERIALS DUE TO ELECTRICAL DISCHARGE

5. FUNDING NUMBERS

Technology Investment Program

6. AUTHOR(S)

Dr. Richard J. Lee

7. PERFORMING ORGANIZATIONS NAME(S) AND ADDRESS(ES)

Indian Head Division
Naval Surface Warfare Center
Indian Head, MD 20640-5035

8. PERFORMING ORGANIZATION REPORT NUMBER

IHTR 1925

9. SPONSORING/MONITORING AGENCY NAME(S) AND ADDRESS(ES)

Indian Head Division
Naval Surface Warfare Center
Code TDE, Stephen E. Mitchell
Indian Head, MD 20640-5035

10. SPONSORING/MONITORING AGENCY REPORT NUMBER

11. SUPPLEMENTARY NOTES

12a. DISTRIBUTION/AVAILABILITY STATEMENT

Approved for public release; distribution unlimited.

12b. DISTRIBUTION CODE

13. ABSTRACT (Maximum 200 words)

Fatal mishaps have been blamed on accidental ignition of solid rocket propellant by electrostatic discharge (ESD). Despite study of this problem since the first incident in 1985 involving a Pershing II motor stage, our understanding of ESD ignition remains limited. To determine the physics of electrically-induced ignition, the temperature, density, and size of electrical arc channels have been quantified during electrical discharge experiments on a composite solid propellant.

To simulate the discharge in ESD scenarios involving insulated motors, short duration electrical discharges (50 to 400 ns) were employed. The lowest ignition energy for these experiments was 160 ± 1.4 mJ. Measurements from pressure transducers and infrared detectors were consistent with a relatively slow thermally-induced reaction rather than prompt ignition from a shock wave. A high-speed framing camera observed expansion of the arc channel as electrical energy was deposited. An analytical model was adapted to predict arc channel expansion for various discharge profiles. An ignition model based on energy transport, via radiation and thermal conduction, from the plasma to the surrounding energetic constituents is proposed. A one-dimensional thermal-chemical kinetics code, XCHEM, was used to demonstrate the importance of radiation in the ignition model.

14. SUBJECT TERMS
ESD Ignition Ignition Modeling
Arc Channel
Energetic Material

15. NUMBER OF PAGES
129

16. PRICE CODE

17. SECURITY CLASSIFICATION OF REPORT UNCLASSIFIED	18. SECURITY CLASSIFICATION OF THIS PAGE UNCLASSIFIED	19. SECURITY CLASSIFICATION OF ABSTRACT UNCLASSIFIED	20. LIMITATION OF ABSTRACT SAR

FOREWORD

The work reported herein was performed at the Indian Head Division, Naval Surface Warfare Center, Silver Spring, MD as part of an on-going effort to determine the physics of ignition due to electrostatic discharge. The sponsor, Mr. Stephen Mitchell, Code TDE, funded the work through the Technology Investment Program, an Indian Head Division self-funded program which funds fundamental and applied research in areas related to the Division's mission of providing a full spectrum of energetic materials science and technology.

Approved by:

William Wilson
Manager, Shock Response Branch

Released by:

Kenneth L. Tomasello
Director, Chemistry and Detonics Division

CONTENTS

TABLE OF CONTENTS (continued)

LIST OF ILLUSTRATIONS

LIST OF ILLUSTRATIONS (continued)

LIST OF TABLES

ACKNOWLEDGEMENT

Chapter 1

INTRODUCTION

The study of ignition from an electrical discharge has historically been a safety issue. (For this report, ignition is defined as the onset of an exothermic reaction that eventually becomes self sustaining.) Early studies were performed on powdered energetic materials, e.g., explosives and propellants at relatively low packing densities. Electrical energy was stored on a capacitor and transferred to the sample either by a closing switch or an approaching needle electrode. Both techniques produced a highly localized electrical current-carrying channel, i.e., an electrical arc channel, through test samples. These tests were and still are used to provide a relative ranking of the sensitivity for different energetic materials. The motivation for these studies was to determine the relative hazards associated with an inadvertent discharge from a statically-charged person.

The interest in understanding more fundamental aspects of electrostatic discharge (ESD) ignition was raised due to a fatal accident with a Pershing II rocket motor section in 1985.[1] This accident, which claimed the life of several service men, marks a turning point in ESD ignition research. The accident demonstrated that solid energetic materials at densities approaching theoretical maximum were susceptible to accidental ESD ignition. Electrostatic energy was stored on the insulating case when the motor section was lifted from pads located in its shipping container. (This charging effect, known as triboelectrification, is common when two dissimilar materials are separated after having been in intimate contact with one another.) An electrical discharge was induced in the propellant when the charged region of the case inadvertently came in contact with the grounded metallic shipping container.

Immediately following this incident, a concerted effort was made to investigate ignition due to an internal discharge in solid, aluminized energetic materials. These materials are usually composites comprised mostly of energetic crystals (explosives and oxidizers), fine metal particles, and a binder. Typical explosive compounds are TNT ($C_7H_5N_3O_6$), PETN ($C_5H_8N_4O_{12}$), RDX ($C_3H_6N_6O_6$) and HMX ($C_4H_8N_8O_8$). A common oxidizer is ammonium perchlorate (AP) (NH_4ClO_4). The metals loading in an energetic material can be between 10 and 25% by weight and is generally a spherical aluminum powder or small flakes of aluminum. Binder systems include hydroxy-terminated polybutadiene (HTPB) or carboxy-terminated polybutadiene.

Prior to the Pershing II incident, secondary explosives and propellants were considered relatively safe since certification tests had indicated that joules of electrical energy were required to obtain ignition. Since this time, relatively small electrical energies, e.g., order of 10 mJ, have been associated with inducing a sustained exothermic reaction in energetic materials.[2,3,4,5] These energies are in accord with the expected values that may be stored on composite casings and subsequently transferred to the energetic material.[6]

Hodges and McCoy[2-4] initially obtained these relatively low ignition energies by pressurizing test samples with nitrogen in a closed chamber. It was observed that electrical energies required for ignition decreased with increasing nitrogen pressure. In an effort to understand the relevance of this phenomenon to energetic systems, Hodges and McCoy[5] confined test samples in a test cell where a force was applied on the electrodes located on either side of the test sample. Similar trends observed in these latter experiments to those of the nitrogen chamber experiments inspired the hypothesis that sufficient containment of the hot gases that evolve during the electrical discharge is important for inducing ignition with electrical energy depositions of tens of millijoules.

Investigators have reported variations in ESD ignition sensitivity due to changes in humidity, temperature, electrical conductivity, electrode geometry, etc.[7,8,9] These factors complicate the study of this phenomenon. Despite considerable effort applied to this problem since the Pershing II incident, our understanding of ESD ignition remains limited.

In an effort to achieve a fundamental understanding of this phenomenon, the physical state of various short duration millijoule electrical discharge channels, i.e., the size, temperature and density of these channels, have been quantified in the present study. Short duration discharges from 50 to 400 ns were used. These discharge characteristics simulate the conditions that would occur from a statically-charged casing. These data have been used to treat the discharge channel as a highly localized heat source comprised of a hot gaseous plasma with a finite amount of thermal energy. The lowest observed ignition energy for these experiments was 160 ± 1.4 mJ. (Ignition was determined experimentally by the total consumption of the test sample.) Measurements from pressure transducers placed 3.18 mm from the arc channel showed that no significant reaction occurred in the propellant during the electrical discharge. In addition, infrared detectors were used to measure the time to reaction following the discharge; the shortest induction time recorded was 5.7 ± 0.2 ms. (The onset of reaction was taken to be the time the detector signal began to increase in magnitude.) Light from the ensuing reaction increased over a period of tens of milliseconds following the induction time, indicating the establishment of a reaction front. These results are consistent with a relatively slow thermally induced reaction opposed to prompt ignition from a shock wave.

The primary contribution of this study is the quantification of the size and temperature of the electrical discharge channel so that it could be characterized as a finite heat source. A high speed framing camera (2×10^7 frames/sec) was used to observe the expansion of the arc channel as the electrical energy was deposited. An example of these results is a 61.8 ± 21.4 µm radius channel observed for an energy deposition of 850 Mj over 400 ns. An analytical model has been adapted to predict arc channel expansion for various discharge profiles defined by the magnitude and duration of the electrical power profile. Post test dissection of inert samples revealed that the arc channel forms in the binder material weaving a convoluted path around the crystalline constituents.

Spectrographic data taken at various intervals during the electrical discharge indicate that the plasma in the channel reaches an equilibrium temperature of 13,000 K early in the discharge. Estimates of the plasma density were made by assuming that the plasma mass corresponds to the mass of binder trapped by the initial formation of the discharge channel: The value is 150 ± 66 kg/m^3. (The AP and aluminum were excluded from this calculation since: (1) Post test dissection of inert samples revealed that the arc channel forms in the binder material around the crystalline constituents and (2) not enough energy was available to evaporate the aluminum.) These plasma properties are important for defining boundary conditions for modeling efforts of ESD ignition.

An ignition model based on energy transport, via radiation and thermal conduction, from the plasma to the surrounding energetic constituents is described. Previous computer models have established reaction as an initial condition and then dealt with mechanisms that might cause the reaction to be quenched. These models have merit, but their assumption of immediate reaction is contrary to the induction period found in this study. The model presented here addresses the initial steps leading to reaction which occur during the induction period.

A one dimensional thermal-chemical kinetics code called XCHEM, developed by Sandia Laboratories, was used to test a part of the ignition model: energy transport to and subsequent ignition of large AP crystals adjacent to the arc channel. The importance of radiation in the ignition model was demonstrated as well. The simulations failed to indicate a sustained reaction for a wide range of input scenarios. This failure can be attributed to either a lack of appropriate kinetics parameters or the existence of other reaction mechanisms that dominate the ignition process.

Chapter 2

BACKGROUND

A fundamental understanding of ESD ignition is required to describe what happened with the Pershing II[1] and to help prevent similar incidents from occurring. Prior to the Pershing II incident, propellants and many explosives in bulk solid form were considered insensitive to ESD ignition, having sensitivities above a joule. Learning that the energy stored on the motor case was sufficient to induce ignition suggested that the sensitivity of the Pershing II propellant was orders of magnitude smaller than previously thought. For example, the ASRM propellant, the focus of this study, is considered to have an ESD sensitivity greater than one joule according to its material safety data sheet, however, the data from this study shows that 160 mJ is sufficient to induce ignition. The explanation for this discrepancy in ignition sensitivities was originally discovered by Hodges and McCoy: they showed that containment of the hot gases produced during the electrical discharge was important to achieving ignition with electrical energies on the order of tens of millijoules.[5] Even though, Hodges and McCoy's work provided a significant step in understanding how the Pershing II incident could have happened, a more fundamental understanding of the ignition process was desired. Modeling efforts[10,11,12] attempted to describe ESD ignition using the data provided by Hodges and McCoy.[2-4] This study adds to the data base by offering an understanding of the arc channel that is produced by the ESD event.

A number of modeling efforts, discussed below, were forced to make assumptions about the physical state of the electrical discharge channel, e.g., the final size, density, and temperature of the channel. Estimates of the initial discharge channel volume have been either inferred from post-test observations or adjusted to force the model to match experimentally obtained ignition results. Thus far all investigators have also assumed that the density of the channel is the same as that for the solid energetic material. It has also been assumed that the release of chemical energy corresponding to the mass of energetic constituents in the channel enhances the thermal energy associated with the discharge channel. Since most of these studies have been focused on propellants, many investigators have also assumed that the temperature of the channel is equivalent to the adiabatic flame temperature of the energetic material. The results of this study show that these assumptions were incorrect.

The main objectives of this study was to quantify the arc channel growth, and its final size, temperature and density. These data are augmented with measurements of minimum ignition energy and time to reaction which help define the decomposition kinetics associated with the problem. This study offers the data that previous modelers lacked.

A review of past modeling efforts is given below as background information for this study; four ESD ignition models reported in the literature are described. The three models proposed by Raun,[10] McHugh,[11] and Mellor, et al[12] have attempted to predict the low level ignition results observed by Hodges and McCoy.[2-4] The fourth model is based on shock induced ignition from a thermally exploded arc channel. The description of these various models represents a review of the present knowledge of ESD.

Computer Modeling Efforts

Two computer models have been developed by Raun[10] and McHugh[11] that focus on correlating ESD sensitivity with the burn rate of the material in question. This concept has been supported experimental attempts by Covino et al[9] to relate ESD ignition sensitivity to burn rate. Both model assume the immediate induction of reaction with the formation of the electrical discharge. Each model treats a mechanism by which the ignition may be extinguished. Raun's[10] model establishes a burning surface that is supported by a hot pocket of gas which was initially formed by the electrical discharge. Ignition is achieved if an increasing burn rate is predicted. McHugh's[11] model treats the possibility of reaction quenching due to over expansion of the gas volume and/or cracking in the solid.

Raun's[10] model is based on the expansion of a hot pocket of gas initially established by the electrical discharge. His model tracks the movement of a burning surface through a solid exposed to the hot gas which promotes decomposition of the surrounding solid into a combustible gas mixture. His criterion for ignition corresponded with a monotonically increasing burn rate.

Raun[10] assumed that the initial arc channel volume, established by dielectric breakdown, is composed of a hot gas with the same density as the solid propellant. He also assumed that the solid propellant, gasified in the formation of the channel, releases its chemical energy in such a way that the gas is at the propellant adiabatic flame temperature. Earlier computations assumed that this volume did not increase directly as a result of additional electrical energy associated with the discharge. This energy only served to raise the temperature of the gas. Later, Raun[13] altered his model to allow for an expansion of the initial arc channel with respect to the deposition energy. He assumed a constant energy density to predict the channel expansion. He chose an initial discharge volume, V'_o, equal to 1.6×10^{-3} mm^3 which was based on the earlier calculations. The volume was set to correspond with a reference pressure, $P_{o,ref}$, equal to 2.07 MPa. The volume of the channel for all other pressures were taken to be proportional to the reference volume as follows:

$$V'_o(P_o) = V'_o(P_{o,ref}) \frac{\Delta E_{ESD}(P_o)}{\Delta E_{ESD}(P_{o,ref})} \qquad (2\text{-}1)$$

where ΔE_{esd} is the discharge energy, and V_o and P_o are the volume and pressure of the arc channel following the discharge which is equivalent to the volume and pressure prior to adiabatic expansion from the presence of the hot gas.

Raun[13] proposed that the hot pocket of gas would expand adiabatically until the pressure of the gas equalized with that surrounding the sample. This allowed him to compare his results to the data from nitrogen pressure experiments performed by Hodges and McCoy.[2-4]

$$T = T_o\left(\frac{P}{P_o}\right)^{\frac{\gamma-1}{\gamma}}, \qquad V = V_o\left(\frac{P_o}{P}\right)^{\frac{1}{\gamma}} \qquad (2\text{-}2)$$

where γ is the adiabatic constant, P_o, T_o, and V_o are the pressure, temperature, and volume respectively prior to expansion, and P, T, and V are after expansion. He used this final temperature, T, as the initial temperature in his burn-rate model which indicated thermal runaway for ignition events. Raun's model[13] indicated the same trend in the data as that experimentally observed by Hodges and McCoy,[2-3] i.e., increasing sensitivity with increasing nitrogen pressure, but failed to match the data satisfactorily.

McHugh's[11] model was based on similar assumptions to that of Raun.[13] The difference was that McHugh incorporated the interaction of thermal and burning effects with the structural response of the solid propellant. His treatment of the initial evolution of the arc channel and subsequent expansion of the hot gasses is identical to that of Raun. However, McHugh's[11] model allows for the input energy, ΔE_{esd}, and the discharge volume, V_{esd}, to be either constant or a linear function of time. The model assumes adiabatic expansion of the gas volume. However, the pressure is calculated from the JWL equation of state:

$$P_g = A_1 e^{-A_2 V_r} + A_3 e^{-A_4 V_r} + A_5 \frac{T_g}{V_r} \qquad (2\text{-}3)$$

where A_1 through A_5 are input parameters, V_r is the relative volume (taken to be V_g/V_{esd} where V_g is the expanding gas volume and V_{esd} is the initial arc channel volume), and T_g is the gas temperature.

McHugh's[11] model treats the possibility of reaction quenching due to over expansion of the gas volume and/or cracking in the solid. If the material has a large bulk modulus and a high fracture toughness, the expansion of the gas volume is small. Under these conditions the gas remains hot and hence sustains the combustion process at the solid-gas interface of the volume. Conversely, if the material has a small bulk modulus or a low fracture toughness, the gas volume becomes relatively large through unrestrained expansions or cracking, respectively. The gas cools and combustion is quenched.

McHugh[11] used Raun's[10] burn rate equation which is strongly dependent on the surface temperature of the solid surrounding the gas volume. The surface temperature was determined from a one-dimensional thermal model for a reservoir of hot gas in contact with the surface. Sustained ignition was achieved by establishing a set of conditions by which the temperature of the gas maintained a burn rate. The model was eventually adapted to predict results from the compressive load fixture experiments performed by Hodges and McCoy.[5]

Characteristic Time Model

Mellor and Stoops[12] proposed adapting an engineering model used successfully for liquid fuel sprays. The model is based on equating characteristic times determined from the reciprocal of heat transfer rates associated with the process. The ignition criterion is established when the rate of heat release resulting from chemistry becomes equal to or exceeds the rate of heat loss from a localized heated volume called the hot spot.

$$\frac{dq}{dt}\Big|_{chem} \geq \frac{dq}{dt}\Big|_{loss} \qquad (2\text{-}4)$$

In terms of characteristic times, ignition is achieved when the characteristic time for heat loss from the hot spot, τ_{sl}, is equal to or exceeds the time required for the heated gasses to ignite, τ_{hc}. As applied to fuel sprays, the hot spot is called the spark kernel. The spark kernel is defined as the pocket of gas surrounding the spark channel that is heated to the stoichiometric adiabatic flame temperature by the electrical energy deposited in the spark channel. For quiescent sprays in air, the fuel must be vaporized prior to ignition. To account for the additional time required for vaporization, Peters and Mellor[14] added a second term in the equation. This term was the evaporation time for a drop in the spray, τ_{eb}, with an empirically determined multiplication factor. The minimum ignition criteria then became:

$$\tau_{sl} = \tau_{hc} + 0.21 \tau_{eb} \qquad (2\text{-}5)$$

Rich et al[15] adapted this model to solid propellants. Thermal conduction was assumed to be the primary mechanism for heat loss in the absence of cracking. Note that if the material should mechanically fail, expansion of the arc channel gasses into cracks would cause rapid cooling of the gas and any ensuing reaction would quench. The rate of heat release is determined by the chemical reaction kinetics and what they called the "propellant preparation" which accounts for the gasification of the energetic constituents prior to reaction. Rich et al[15] expressed the characteristic time equation in its most general form as follows:

$$\tau_{sl} = m\left(\tau_{hc} + k\phi\tau_{p,prep}\right) + b \tag{2-6}$$

where τ_{sl}, τ_{hc}, and $\tau_{p,prep}$ are the characteristic times for conductive heat loss, ignition delay, and propellant preparation, respectively, ϕ, is the equivalent ratio, i.e., the ratio of combustible material to noncombustible material. The proportionality constants **m** and **k** are required due to the uncertainty of the characteristic times. The value **b** is determined from an empirical correlation but typically considered negligible. They pointed out that ignition of the aluminum is a much slower process than that for the typical oxidizer, e.g., AP, hence the metal loading was considered inert in, ϕ, the equivalent ratio.

Rich et al[15] defined the characteristic time for heat dissipation as the ratio of the hot spot surface area, A_{mr}, to the solid propellant thermal diffusivity, α_p. This surface area is determined from the final volume of the hot spot. They assumed that the arc forms a heated volume, i.e., the hot spot, which is elevated to the stoichiometric adiabatic flame temperature. The initial volume formed by the discharge is determined from:

$$V_{esd} = \frac{E_{ig}}{\rho_p C_{pa} \Delta T_{\phi=1}} \tag{2-7}$$

where V_{esd} is the initial volume of the hot spot, E_{ig} is the electrical deposition energy required for ignition, ρ_p is the propellant solid density, C_{pa} is the specific heat of the combustion products at the average of the stoichiometric and initial temperatures, and $\Delta T_{\phi=1}$ is the stoichiometric adiabatic flame temperature rise at constant volume for the propellant. The final volume is determined by allowing V_{esd} to isentropically expand to V_{mr}.

The characteristic time for ignition delay is derived from an Arrhenius expression:

$$\tau_{hc} = \frac{B\phi}{\rho_{mr}^n} e^{\frac{E_a}{RT_{mr}}} \tag{2-8}$$

where **B** is a constant, E_a is the activation energy, **R** is the gas constant, T_{mr} and ρ_{mr} are the gas temperature and the density in the cavity after isentropic expansion, and **n** is the overall reaction order. Rich et al[15] compared this model to the constant pressure data of Hodges and McCoy[2-4] as did Raun.[10,13] Hence, they chose the constant **B** equal to 10^{-5} ms to place the ignition delay times on the order of milliseconds to match delay times observed by Hodges and McCoy. They chose the activation energy and overall reaction order to be 7500 K and 0, respectively, following from Raun's computer model discussed above.

Rich et al[15] defined the preparation time as the time required to gasify a quantity of oxidizer, e.g., ammonium perchlorate. The definition excludes gasification of the binder as it is assumed that the binder is gasified during dielectric breakdown. This follows from observations by Isom and Speed[16] that the breakdown occurs through the binder between aluminum particles. The gasification of aluminum was not considered for the preparation time since

it was assumed that the aluminum is not gasified during these phases of the ignition process. They used an empirical correlation from Hermance[17] for the ignition delay for AP crystals embedded in burning propellant.

$$\tau_{p,prep} = k_o \frac{D_i^{1.8}}{P_{mr}^{0.75}}$$ (2-9)

where $k_o = 2 \times 10^5$ ms-atm$^{0.75}$-cm$^{-1.8}$, D_i is the oxidizer particle diameter, and P_{mr} is the hot spot pressure after isentropic expansion of V_{esd}.

They compared their calculations for minimum ignition energy to the PBAN and HTPB data from Hodges and McCoy[2-4] with favorable results. This comparison suggested that the ignition process was mostly dependent on the chemical kinetics, i.e., they achieved the best fit by excluding the preparation time.

Shock Ignition Model Featuring Thermal Explosion

Lee et al[18,19] proposed an analytical model based on shock ignition. It was assumed that the reactive constituents trapped in the arc channel would thermally explode following an induction time. Walker and Wasley's[20] energy fluence method for predicting shock sensitivity was used to determine the minimum ignition criteria for this scenario in an aluminized explosive. The energy fluence, E, was approximated by:

$$E = \frac{P_s^2 \tau}{U_s \rho_o}$$ (2-10)

where P_s is the peak stress at the initial impact surface of the unreacted explosive, τ is the shock pulse width at one-half peak stress, U_s is the shock velocity and ρ_0 is the initial density.

The minimum energy fluence for ignition was set at the threshold for first reaction as defined by Liddiard and Forbes[21] for shock-induced reaction studies. First reaction, originally called the burning threshold, is where the first evidence of reaction is observed on a plot of shock velocity vs particle velocity, i.e. where the data depart from what would be considered the unreactive curve. The analysis suggested that the shock pressure, shock velocity, and initial density would be the same in each case for a given material. Hence, the shock pulse width, τ, was indicated as the critical parameter for ignition.

The thermal explosion was assumed to occur in the arc channel at constant volume. From a polytropic equation of state[22] for the gas products, the explosion pressure, P_e, is exactly half the Chapman-Jouget pressure, P_{cj}, the Chapman-Jouget pressure being the pressure associated with the detonation wave of the material in question. The shock pressure, P_s, delivered to the unreacted explosive is determined from the intersection of the reacted thermal explosion isentrope[18] and unreacted shock Hugoniot given below respectively.

$$u_p = -\frac{2}{1-\gamma}\left[\frac{\gamma P_e}{\rho_o}\right]^{\frac{1}{2}}\left\{\left(\frac{P}{P_e}\right)^{\frac{\gamma-1}{2\gamma}} - 1\right\}$$ (2-11)

$$P = \rho_o u_p U_s$$ (2-12)

where the coefficient $\gamma = 3.34$ for the polytropic equation of state at high pressures, ρ_0 is the initial density of the material, u_p is the particle velocity, and U_s is the shock velocity. The particle velocity in the channel was taken to be initially zero since thermal explosion is a constant volume reaction. The shock velocity in the material beyond the arc channel was determined from a linear relationship with the particle velocity.

$$U_s = Su_p + b$$

(2-13)

where S and b are the slope and intercept of the unreacted Hugoniot. The shock pulse width was estimated to be the time it takes the first rarefaction to travel to the center of the discharge channel and back again to meet the expanding channel wall. The expansion velocity of the channel after thermal explosion was taken to be the particle velocity in the shocked solid. This analysis indicated a critical arc channel size was required for a thermal explosion to produce a shock pulse width adequate to induce a reaction in the material beyond the arc channel. From this, it was suggested that the minimum ignition energy could vary with changes in energy deposition rate, i.e., the electrical power deposition. This follows from Tucker's[23,24] observation that higher deposition rates produce faster expanding channels.

Summary Remarks

The various models mentioned above have made a number of assumptions about the physical state of the electrical discharge channel which were incorrect. The main objective of this study was to quantify the growth, final size, temperature and density of the electrical discharge channel so that future modeling efforts would benefit from having the correct initial conditions. These data are augmented with measurements of minimum ignition energy and time to reaction which help define the decomposition kinetics associated with the problem. Other observation from this study help provide a better view of what the electrical discharge channel is and how the energy stored in the channel is redistributed to the surrounding solid.

The data from this study were used to develop an ignition model based on energy transport, via radiation and thermal conduction, from the plasma that makes up the discharge channel to the surrounding energetic constituents. A number of concepts are discussed which require more study. Future modeling efforts will benefit from this study.

Chapter 3

EXPERIMENTAL

Various diagnostics were employed in electrical discharge experiments to provide information on the physical dynamics and chemical kinetics associated with the development of an arc channel in solid energetic materials. The premise is that a fundamental understanding of the ignition process from an electrical discharge requires a knowledge of the arc channel evolution. A detailed description of each diagnostic is given in this chapter. A brief summary of the experimental technique is provided as an introduction.

A charged cable pulser was used to provide electrical discharges with durations from 50 to 400 ns. This technique offered the ability to vary the energy deposition rate, i.e., the electrical power, and the magnitude of the energy deposition independently from one another. The electrical power and energy were determined for each experiment from measurements of current and voltage. High speed photographic data offered a unique view of the arc channel diameter with changes in electrical power, energy, and discharge duration.

The arc channel is highly confined by the surrounding solid, the pressure and density of the plasma are relatively high and hence may be treated as a blackbody radiator. Therefore, spectrographic data taken at various intervals during the discharge provided an indication of the temperature evolution in the arc channel.

Comparisons with inert samples were made to observe any indication of reaction in the arc channel. Infrared detectors were used to indicate when reaction occurred in the surrounding material beyond the arc channel. Post-test arc channel damage was also compared to the dynamic development of the arc channel radius to infer the density of the arc channel plasma. These data were used to validate an ignition model based on thermal transport from the hot gaseous channel to the adjacent reactive constituents.

No effort was made to control environmental effects on ESD sensitivity, since the focus of this research was on the development of the discharge channel. Dielectric breakdown was ensured for the experiments analyzed in this study by taking note of the current and voltage profiles. Not achieving dielectric breakdown thereby not forming a localized discharge channel may have compromised results of other studies not employing voltage and current diagnostics.

Great pains were taken to insure a single channel event in each experiment. Multiple channels could profoundly alter the ignition for a given set of electrical parameters. These multiple channels share the electrical energy, but not necessarily equally.

Bulk Breakdown Configuration

Small cylindrical samples, 12.7 mm (1/2") in diameter and 6.35 mm (1/4") thick, were tested in an enclosed test cell. Two basic configurations were employed; the bulk breakdown configuration and the surface discharge configuration. The surface discharge configuration is discussed later in this chapter. The bulk breakdown configuration, shown in Figure 1, forced the discharge through the test sample between planar electrodes placed on either side of the sample. This configuration provided data on an internal discharge, i.e., a discharge which would be completely surrounded by the material of interest, hence, a majority of the energy evolved in the arc channel was coupled into the sample.

The experimental arrangement was designed to confine the test sample, mitigate against surface discharges and align the viewing hole in the low voltage (LV) electrode with the camera and other optical diagnostics. This was accomplished by supporting the test sample and low voltage electrode with a transparent window, 38 mm (1.5") in diameter and 12.7 mm (0.5") thick, which fit into a polymethyl methacrylate (PMMA) retaining ring. The retaining ring fit over two locating pins pressed into the base of the test fixture. These pins aligned the system over a 12.7 mm (0.5") hole which served as a viewing port. The containment cylinder fit around the window and into a shallow groove cut into the retaining ring to align the test sample with the electrodes. The test sample was mechanically confined in a room temperature vulcanizing rubber (RTV) washer which fit firmly in a PMMA containment cylinder. A 1.8 kN (400 lbf) force was applied to a PMMA loading rod located directly over the top electrode via a bolt supported at the top of the test fixture. A load cell, fitted between the loading rod and bolt, provided confirmation of the loading force. The washer pressed against the cylinder wall under the applied force to mitigate against undesirable surface discharges. The test sample was confined at the top surface by a 9.5 mm (3/8") thick brass disk which was the high voltage (HV) electrode. This electrode and the window under the low voltage electrode served to contain the gases generated during the electrical discharge. The loading force also served to improve the contact between the sample and the confining components.

Thin Kapton masks were used over both electrodes to control the location of the arc channel. A small hole in each mask ensured that the discharge formed towards the center of the test sample. The mask covering the thick top electrode was made from 25 μm (1 mil) thick Kapton and was secured in place with vacuum grease. The mask covering the thin bottom electrode was made from a 63 μm (2.5 mils) thick adhesive backed Kapton tape. A punch was used to produced a 0.4 mm (16 mils) diameter hole in the Kapton tape and a 0.5 mm (20 mils) diameter hole in the brass foil. This hole pattern kept the arc channel towards the center of the sample and in line with the steering optics. Optical radiation (infrared and visible) emitted from the bottom surface of the test sample passed through the viewing port and was directed either by a mirror or a fiber optic to a high speed camera, photodetectors, or a spectrograph.

Both electrodes were comprised of two conducting tabs which either stuck out over the top or through slits at the base of the containment cylinder. These tabs facilitated electrical connection with the leads for the discharge circuit and the voltage probe. The voltage probe was always connected separately from the high current lead to minimize errors in the voltage record.[25]
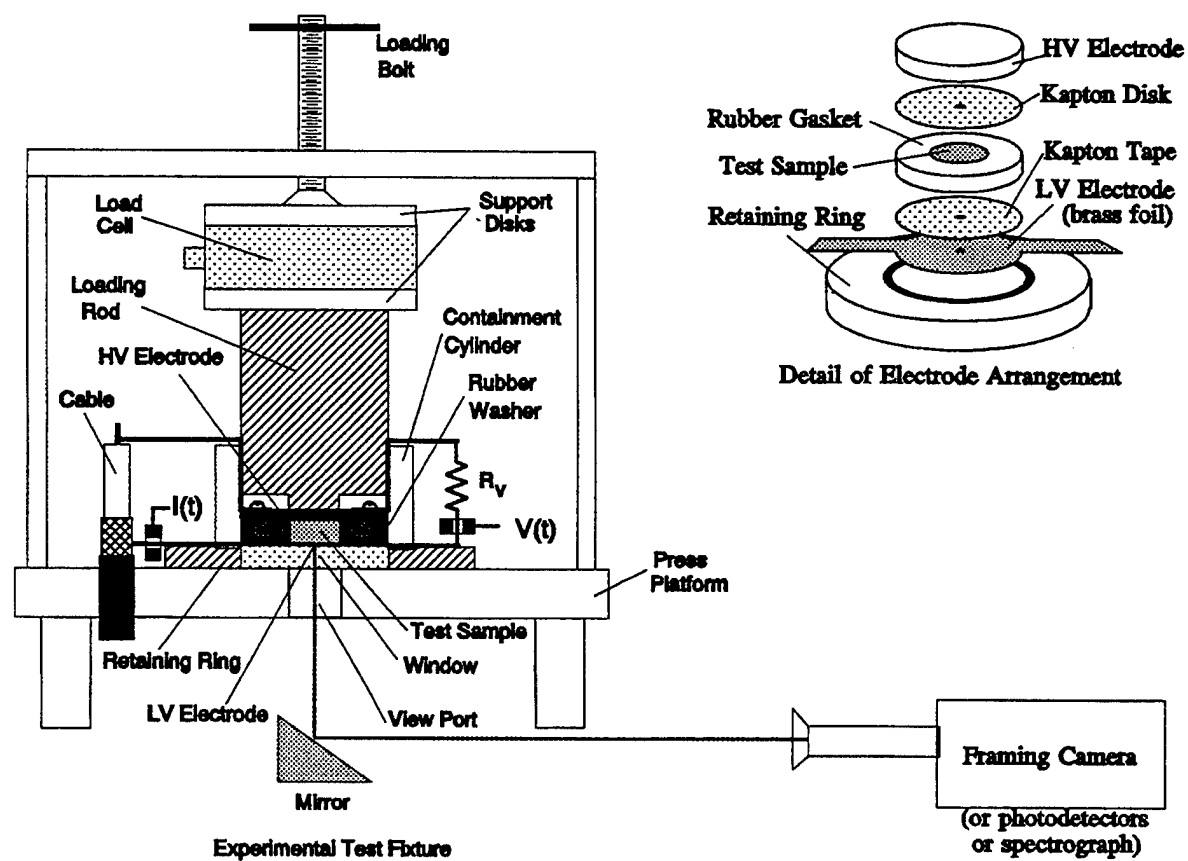
Figure 1. Bulk Breakdown Configuration

Sample Materials

NASA's Advanced Solid Rocket Motor (ASRM) propellant, ANB 3652-1, and its inert simulant, DP-75, were used for test samples. The simulant provided comparisons for various data due to its inert response. Specifications of sample materials are given in Table 3-1. The propellant consists of 69% AP crystals, 19% fine spherical aluminum particles and a hydroxyterminated polybutadiene (HTPB) binder system. potassium chloride crystals replaced the AP for the inert simulant. The density of both materials was 1810 kg/m^3. The presence of aluminum facilitated dielectric failure of the test samples, allowing arc channels to be formed at moderate voltages across the 6.35 mm (1/4") electrode gap. Both cast materials were machined into slabs 6.35 mm (1/4") thick. A cork boring tool was used to cut out 12.7 mm (1/2") diameter disks to be used as test samples.

Table 3-1. Specifications of Test Sample Materials

Composition	ASRM Propellant	ASRM Inert Simulant
Ammonium Perchlorate (NH$_4$ClO$_4$)	69%	NA
250 μm	48.3%	NA
20 μm	20.7%	NA
Potassium Chloride (KCl)	NA	58%
130 μm	NA	47%
28 μm	NA	11%
Spherical Aluminum Powder (30 μm diameter)	19%	27.17%
Dioctyladipate (DOA) Plasticizer	2%	2.5%
Hydroxy Terminated Polybutadiene (HTPB) HO-(C$_4$H$_6$)$_n$-OH	9%	11.13%
Isophorone Diisocyanate (IPDI) Curing Agent	0.6%	NA
Ferric Oxide	0.1%	0.1%
HX 752 Bonding Agent	< 0.5%	0.2%
AO 2246	< 0.5%	NA
Density (kg/m^3)	1810	1810

Discharge Circuit

A charged cable pulser was used to provide electrical discharges with durations from 50 to 400 ns. The technique, illustrated in Figure 2, stores electrical energy on a charged cable and then rapidly transfers that energy to some load. Additional features like a transfer cable between the switch and the test cell, and the current and voltage diagnostics are also illustrated in Figure 2. This technique was used for a number of reasons; it offered the potential for fast-developing arc channels which were required to investigate the possibility of shock-induced ignition, the magnitude and deposition rate of the electrical energy can be varied independently from one another, and short discharge pulses serve to decouple the arc channel evolution from the potentially slower ignition due to thermal conduction thereby simplifying the analysis.
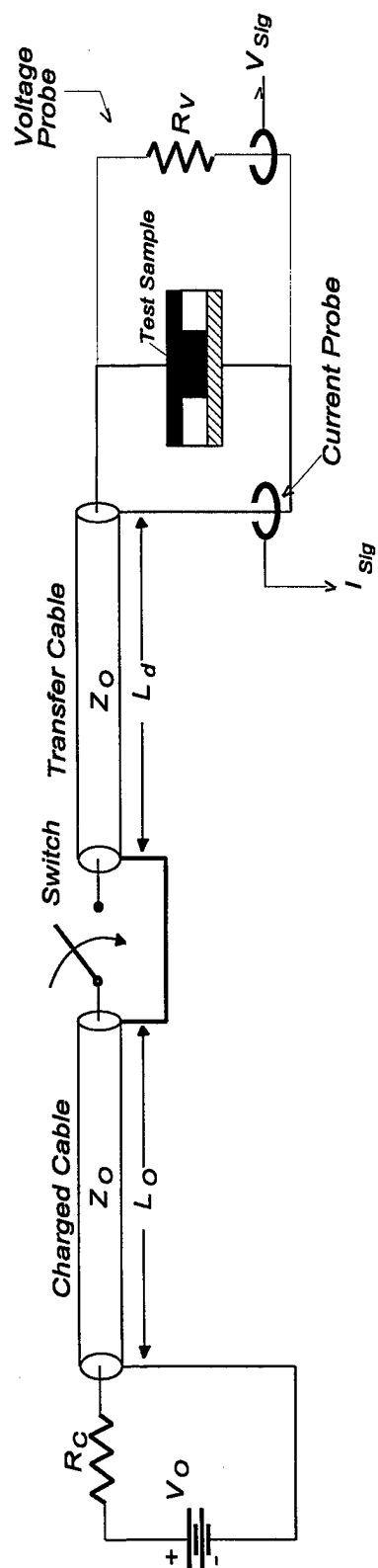
Figure 2. Experimental Circuit With Electrical Diagnostics

Charged cable pulsers offer rectangular current pulses if they are operated into a load matching the characteristic impedance, Z_0, of the cable. Since the arc channel in these experiments was highly resistive and dynamic in nature, it was difficult to achieve a matched load. Figure 3 offers a comparison between current pulses for a matched load, 50 Ω, and an aluminized sample.
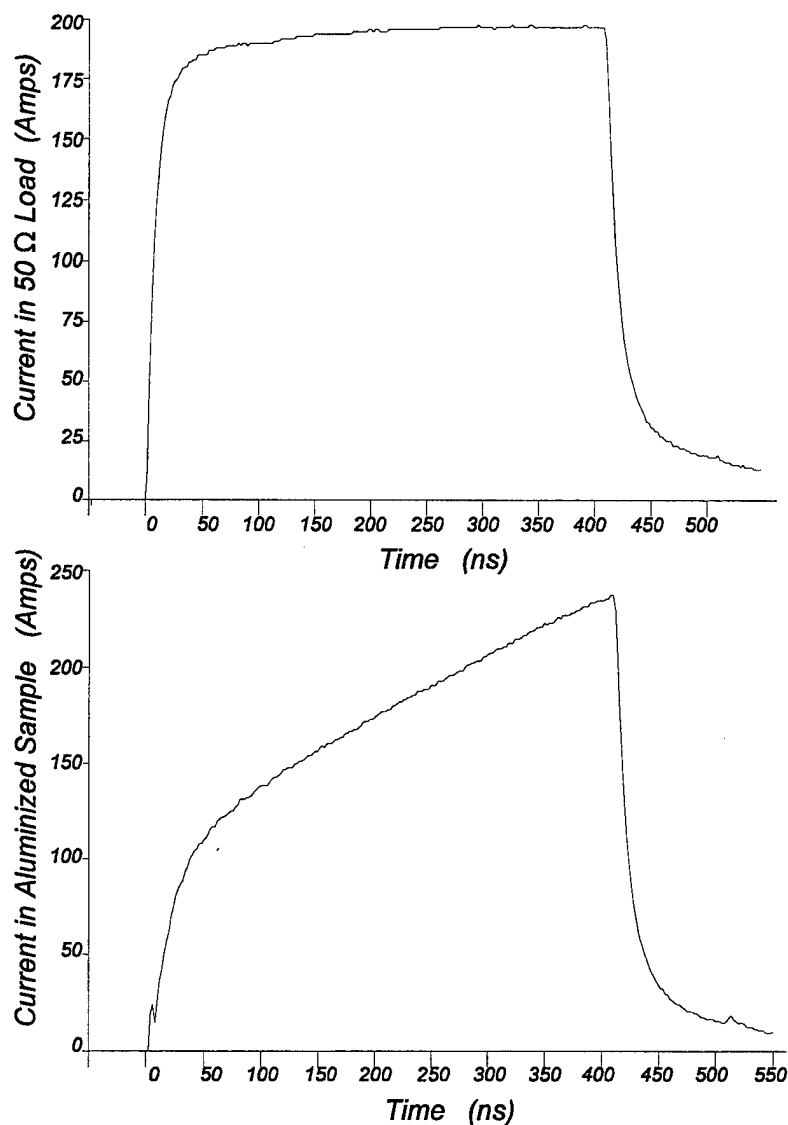
Figure 3. Comparison Between Current Pulses in a Matched Load and a Test Sample

When the switch was closed, the voltage across the cable, V_0, was dropped across the sample after propagating down the transfer cable. If V_0 was sufficient to cause dielectric breakdown, the current would begin to flow. The current through the arc channel can be defined by the following expression:

$$i(t) = \frac{V_0}{Z_0 + R} (1 - e^{-\frac{t}{\tau}}) \tag{3-1}$$

where V_0 is the open circuit voltage of the charged cable, Z_0 is the characteristic impedance of the charged line, $R = R_s + R_{load}$, and $\tau = L/(Z_0 + R)$, where R_s is the sum of any series resistance that exists from connections, R_{load} is the resistance of the arc channel, and L is the total inductance associated with the system.

The duration of the pulse is defined by the time it takes an electromagnetic wave to propagate down one end of the cable and back. The propagation velocity, v_p, is determined by the relative dielectric constant, ϵ_r, of the dielectric medium:

$$v_p = \frac{c}{\sqrt{\epsilon_r}}, \quad \text{where c = the speed of light} \tag{3-2}$$

It is useful to note that the propagation velocity in most co-axial cables is nominally 20 cm/ns. The rise time of this circuit is defined by 2.2τ; note that the inductance, L, affects the rise time of the pulse. The inductance associated with the loop incurred from the cable connections to the electrodes was determined experimentally to be 120 nH. This corresponds to a rise time of 2.8 ns for a matched load. This is close to rise times indicated on current records taken with a matched load in place of the test gap. These records were obtained with a 1 GHz band width analog oscilloscope (Tektronix 7104), however, electrical data were typically taken with a digital oscilloscope. Early studies used a Nicolet 4094C main frame with 4180 plug-ins, with a limited bandwidth of 20 MHz and sampling rate of 5 ns/pt. Later experiments used a Lecroy Model 9314 digital oscilloscope with a bandwidth of 300 MHz and a sampling rate of 2 ns/pt. For both digital oscilloscopes the perceived rise time was 20 ns. This was not a problem for accurate data representation because the measured rise times for current profiles in the test samples varied and were typically longer than 20 ns. These longer rise times were attributed to the breakdown process in the test sample.

The experiments were carried out with an Instrument Research Company Model LX-40 cable pulser. The LX-40 allowed convenient use of co-axial cables in a variety of lengths which defined the duration of the discharge pulse. Electrical energy was stored on a given length of cable by charging it to the desired voltage (up to 40 kV) and then transferred to the load via a co-axial mechanical switch. The LX-40 system offers rise times down to 1 ns for a RG-214 co-axial cable switched into a matched load. The rise time typically degrades with cable length due to a finite resistivity associated with the cable conductors.

RG-214 double shielded co-axial, 50 Ω cables 5, 10, 20, 30, and 40 m long were used to provide respective pulse lengths of 50, 100, 200, 300, and 400 ns. The electrical energy was deposited in the form of a filamental arc channel which was established after dielectric breakdown between two metallic electrodes. The dynamic resistance associated with the electrical discharge did not provide an ideal matched load for the system. Hence, the current and voltage varied in magnitude during the discharge. The arc channel resistance typically decreased from several 100 Ω to tens of Ohms during the discharge. The current and voltage ramped up and down respectively but the power pulse was typically rectangular.

Electrical Diagnostics

The voltage, $V(t)$, and the current, $I(t)$, were measured with field coils (Pearson Electronics Model 2877), as indicated in Figure 2. Field coils were used to eliminate problems associated with ground loops. These data were used to make calculations of the electrical power profile, $W(t)$; and the energy deposited, $E(t)$; for each experiment.

The voltage probe consisted of a Pearson field coil measuring the current through a liquid resistor. The resistor was made from concentrated liquid soap (Arm and Hammer) contained in a 6.35 mm (0.25") ID Tygon tube capped at the ends by stainless steel plugs. The liquid column of soap was nominally 38 mm (1.5") long. The total length of the resistor was 63.5 mm (2.5"). Conducting leads were fastened tightly at each end with screws. Copper strips soldered to these leads facilitated connection to the electrode leads. A convenient connection between leads was made by pressing the respective copper tabs together with alligator clips. The small resistance from these type connections was negligible in comparison to the nominal value of 1000 Ω used for the liquid resistor. The value of the liquid resistor was measured prior to each experiment with an impedance bridge (Hewlett Packard Model 4277A). The voltage probe was connected directly across the electrodes to minimize the effects of inductance. The effects of parasitic inductance in series with the arc channel, L_{Ld}, and the voltage probe, L_v, were analyzed and found to be negligible. The error induced by a parasitic capacitance, c_v, established between the two metallic end caps of the liquid resistor, was analyzed as well and found to be insignificant. These errors are discussed in more detail in Appendix B.

Current measurements were made with a Pearson field coil fitted over a lead that was connected to the ground braid of the transfer cable from the LX-40 Cable Pulser. Pressure connections via alligator clips were used here as well. Any voltage drop across these connection due to high currents was outside of where the voltage probe was measuring, hence no error to the voltage record was incurred from these type connections. The additional current passed through the voltage probe was typically negligible in comparison to the currents flowing through the arc channel, however, the current recorded through the voltage probe was subtracted from the current measurement during data reduction using a computer. The error induced by a parasitic capacitance, c_{Ld}, across the electrode gap was analyzed as well. The errors associated with the current measurement are discussed in more detail in Appendix B.

High Speed Photography

Temporal and spatial characteristics of the arc channel light were examined using an Imacon 675 camera (Headland Photonics, Ltd) in an effort to quantify the radial expansion of the arc channel. A crossectional view of the arc channel was observed by forcing the channel to form in a 0.5 mm diameter hole in the cathode, as indicated in Figure 1. Earlier experiments indicated wide variations in the final channel size due to expansion of the arc plasma into cavities at the surface of the test samples. Vacuum grease was applied over the surface of each test sample which mitigated experimental optical intensity variations resulting from the irregular surfaces of the test materials.

The Imacon camera was operated in the framing mode at a speed of 20×10^6 frames/sec which provided a 50 ns interframe time and an 10 ns exposure time per frame. The camera and oscilloscope were triggered from the output of a B-dot probe which sensed the initial rise in current associated with the closing of the high voltage switch. The voltage wave launched from the charged cable pulser was delayed by 250 ns in arriving at the test sample by a 50 meter transmission line. This allowed more than enough time for the electronic shutter of the camera to open. Camera operation was then synchronized with the start of the current pulse by delaying the arrival of the trigger pulse via an appropriate length of RG-58 cable. The camera monitor pulse was recorded to compare camera operation with the current and voltage records associated with each electrical discharge.

Spectrographic Measurements

In a number of experiments, a narrow band of wavelengths between 450 nm to 620 nm was spectrally resolved from light emitted by the arc channel. Spectra for various discharge characteristics were observed. These spectra were compared to blackbody curves to determine the temperature of the channel plasma. The light from the arc channel was imaged onto the slit of a Spex 1877 Triplemate spectrometer via a fiber optic. The other end of the fiber optic was positioned behind the window supporting the test sample. Unfortunately, positioning the fiber optic like this excluded simultaneous use of other optical diagnostics, therefore, these experiments were carried out separately from those employing the Imacon camera and infrared detectors.

Details Concerning the Spectrograph: The Triplemate spectrograph consists of two stages; a filter stage which employs a 0.22 m double monochromator with gratings locked in a subtractive-dispersion mode and a 0.6 m, single monochromator spectrograph stage. The filter stage acts as a selectable bandpass filter for selected wavelength bands. The spectrograph stage disperses the desired radiation over the detector array. This dispersion is varied over the detector array by selecting one of three gratings (600, 1200, and 2400 grooves/mm with respective dispersions of 0.07, 0.035, and 0.0175 nm/μm) mounted on a manually actuated turret.

Gratings with 150 grooves/mm were used in the filter stage of the Triplemate which allowed a bandpass of 125 nm to the spectrograph stage. The central wavelength of the band passed through the system was selected by external controls which adjust the optics in the filter section.

The selected spectrum was taken by a gatable intensified diode array coupled to an optical multichannel analyzer (Tracor Northern) offering a temporal resolution of 10 ns. The spectral response of every array element varies over the spectrum between 185 nm and 1000 nm. The observable spectrum was limited to wavelengths between 400 and 700 nm due to a combination of the array response curve and relatively low light levels collected from the small arc channel. Compensation for the spectral response of each array element was performed with a standard light source (Oriel model 63350).

Timing of the detector gate pulse relative to the discharge pulse was varied with a trigger-delay generator. The system did not allow for multiple timing sequences over the fast discharge time (between 100 to 400 ns), however, spectra were acquired between 100 ns to the end of the discharge by performing different experiments where the appropriate trigger delay was set.

Determination of Temperature: The temperature was determined by comparing the intensity profile for the band of wavelengths between 450 nm to 620 nm to various normalized blackbody curves to determine a match. The spectral distribution of radiant emittance from a blackbody is given by Planck's radiation equation:

$$I_{bb}(\lambda) = \frac{2\pi c^2 h}{\lambda^5} \frac{1}{e^{\frac{ch}{\lambda kT}} - 1} \tag{3-3}$$

which may be written as:

$$I_{bb}(\lambda) = \frac{c_1}{\lambda^5} \frac{1}{e^{\frac{c_2}{\lambda T}} - 1}$$

(3-4)

Where c is the speed of light, h is Planck's constant, λ is the wavelength, k is Boltzman's constant, T is the absolute temperature in Kelvin, c_1 is equivalent to 3.742×10^8 W/m^2-μm^2, and c_2 is equivalent to 1.439×10^4 μm-K. A number of blackbody curves are given in Figure 4. As the temperature increases the emittance peak shifts from high wavelengths in the infrared (0.8 to 2.0 μm) to shorter wavelengths in the visible (0.3 to 0.8 μm) and ultraviolet (below 0.3 μm). The emittance increases in magnitude across the spectrum for increasing temperature. Note that the shape of each curve is distinguishable from the rest. This provides a predictable spectrum for determination of the temperature.
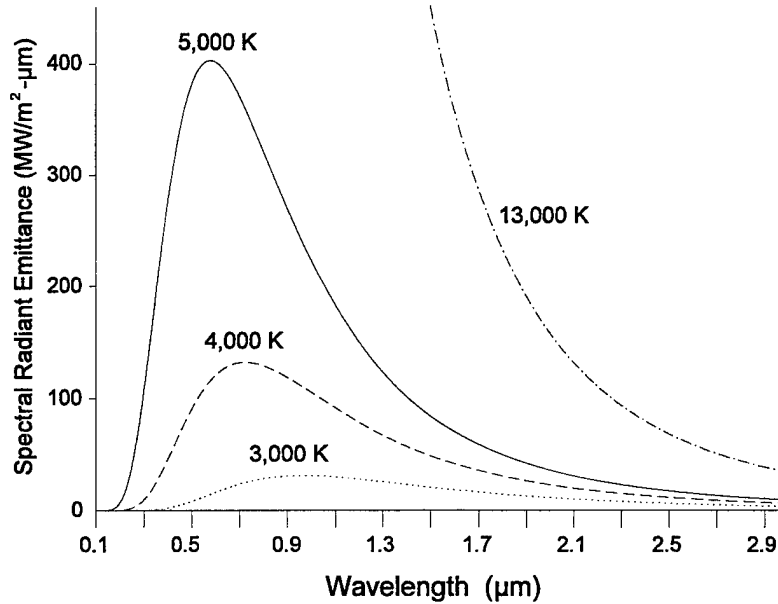
Figure 4. Examples of Blackbody Curves for Different Temperatures

There are materials that do not radiate like a perfect blackbody. For these cases a spectrally dependent emissivity, $\epsilon(\lambda)$, takes care of any deviations that the source may have from a true blackbody. The radiant emissivity at a given wavelength, ϵ_λ, or spectral radiant emissivity is defined by:

$$\epsilon_\lambda = \frac{I_\lambda}{I_{b\lambda}}$$

(3-5)

Where I_λ is the radiant emittance of the source and $I_{b\lambda}$ is the radiant emittance of a blackbody at a given wavelength. If the emissivity is constant over all wavelengths or at least over the range of interest, the source is considered a gray body. The plasma associated with the arc channel was assumed to radiate with the characteristics of either a blackbody or a gray body, so the shape of the radiant emittance was preserved.

18

Surface Discharge Configuration

Surface discharge experiments were originally performed to provide a better view of the arc channel, i.e., along the length of the arc channel. Unfortunately, the arc channel usually formed in the material instead of along the surface, thereby, rendering observations of the arc channel impossible for many experiments. (This effect was attributed to the aluminum loading and the relative rough surface of the sample due to pits left by the absence of crystals removed inadvertently during sample fabrication.) This configuration, shown in Figure 5, was required for making two measurements: the time to reaction and pressure profiles in the solid beyond the arc channel. Infrared detectors recorded comparatively consistent times to reaction for the surface discharge configuration. (The time to reaction was taken to be the time the detector signal began to increase in magnitude; ignition was defined as sustained reaction and determined by the total consumption of the sample.) The bulk breakdown configuration did not provide consistent times to reaction; variations between tens to hundreds of milliseconds were observed in bulk breakdown experiments. This large variation was attributed to localized reaction sites along the length of the discharge channel. The surface discharge configuration proved to be the only way to acquire pressure profiles in the solid beyond the arc channel. It proved to difficult to insulate the pressure transducers and insert them into position in bulk breakdown experiments.
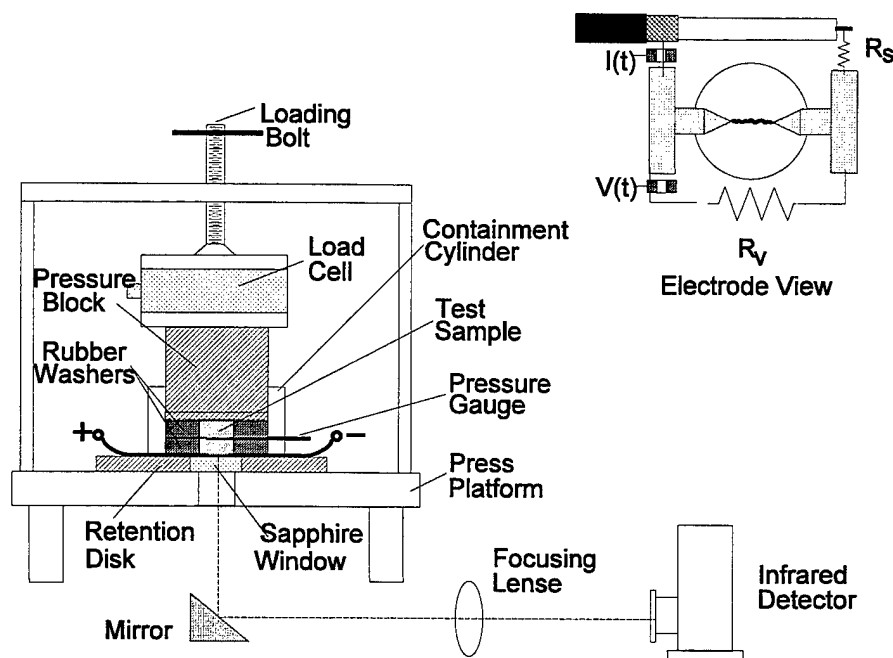
Figure 5. The Surface Discharge Configuration

For the surface discharge configuration, the electrical discharge was formed between two thin electrodes along the interface between one surface of the test sample and a sapphire disk, 19 mm (3/4") in diameter and 12.7 mm (1/2") thick. The electrical circuit was the same as that used for the bulk breakdown configuration shown in Figure 2. The electrodes were brass foils, 12.7 mm (1/2") wide and 25.4 μm (1 mil) thick, cut to a 30° angled point. The gap spacing between the electrode tips was 6.3 mm (1/4"). Each electrode was held in place on the sapphire window by a strip of 63.5 μm (2.5 mils) thick adhesive-backed Kapton tape. The sapphire disk offered a window which was resistant to

arc erosion, allowing the use of the same surface and electrode configuration through the course of a given experimental series. The sapphire disk was held in place by a PMMA retaining ring which fit over two locating pins pressed into the base of the test fixture. The test samples were circumferentially confined by an RTV washer which fit in a PMMA containment cylinder with an inner diameter of 38 mm. The containment cylinder was secured in a groove cut in the top surface of the retaining ring.

Photodetectors

An infrared detector system using photodiodes based on germanium and indium antenamide was used to observe when reaction occurred. Originally, light from the arc channel was brought to the detector by a gold turning mirror and a barium flouride focusing lens. Latter experiments used a fiber optic to place the diodes a few feet from the discharge to mitigate electrical noise pickup. Earlier experiments employed a gold-plated mirror and a barium fluoride lens to direct the light onto the detector. The earlier experiments incorporated attempts to resolve temperature changes associated with the arc channel. Despite the efforts to minimize noise, temperature profiles during and immediately following the electrical discharge were not observed due to a number of technical difficulties only one of which was electrical noise. The photodiode system was still useful in recording when reaction occurred since this event was well after the discharge and there was no longer electrical noise with which to contend.

Pressure Measurements Parallel to the Arc Channel

A thin film polyvinylidene difluoride (PVDF) pressure transducer, shown in Figure 6, was placed parallel to the arc channel, using the surface discharge configuration shown in Figure 5, to directly measure any shock propagating in the material surrounding the arc channel. Ignition occurred tens of milliseconds after the electrical discharge, records from the pressure transducers and the IR detectors were recorded with a relatively high memory LeCroy oscilloscope (Model 9314M, 300 MHz Bandwidth, 10 ns/pt sampling rate). These data were used to investigate the ignition either directly from the shock established during channel expansion, or subsequently due to a delayed thermal explosion in the arc channel. The existence of a secondary shock pulse occurring at the time of ignition as indicated by the IR detectors, would be taken as evidence of the latter scenario.

The PVDF gauge was inserted through a slit in the containment cylinder located $90°$ from the electrode access slits and at an appropriate height from the sapphire surface. The active area of the transducer was situated directly over the center of the discharge gap. The distance between the discharge gap and the transducer was defined by the thickness of the test sample. Most experiments used a 3.18 mm (1/8") thick test sample with another 6.35 mm (1/4") sample and RTV washer set behind the gauge for confinement. Departures from this configuration are mentioned in the Results section. Vacuum grease was applied at all interfaces, except at the discharge gap, to exclude air at these surfaces. The discharge gap was left clear of vacuum grease so as not to impede the dielectric breakdown process. The pressure-gauge package was based on the standardized PVDF transducer element marketed by K-tech Corporation using the patented Bauer poling process. The uniaxial stress is obtained from a strain versus charge density calibration.[26,27] Note that lateral strain effects are also important, as described later. The charge was measured using a 1 nF integrating capacitor. A 50 Ω resistor was placed in series between the integrating capacitor and the cable for electrical impedance matching. An active area (nominally 9 mm^2) was selected because it provided a reasonable signal to noise ratio with the 1 nF integrating capacitor. Smaller gauges, requiring a smaller capacitance, suffered from premature signal attenuation due to a significant RC droop.
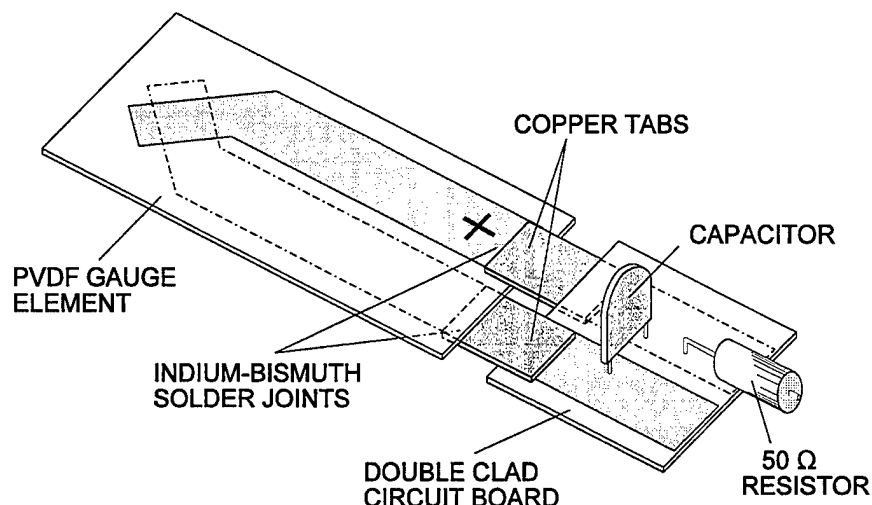
Figure 6. PVDF Pressure Transducer with Integrating Circuit

Gauges were shielded on both sides by an unbroken sheet of 25.4 µm (1 mil) thick copper foil folded over the transducer at the end closest to the active area. The negative lead was directly bonded to the shield while the positive lead was insulated from the shield by a 25.4 µm (1 mil) thick sheet of Mylar. Earlier gauges, that were shielded only over the negative lead, developed a noticeable base line shift. The double shielded gauges provided better electrical noise rejection, eliminating the base line shift and, hence, allowed a closer placement of the gauge to the discharge gap.

Each gauge was electrically insulated from the high voltage area by placing a 25.4 µm (1 mil) thick disk of Kapton, 38 mm (1.5") in diameter, between the gauge and the test sample. For experiments where the voltage exceeded 30 kV, 127 µm (5 mil) Kapton disks were used. Attempts at gluing sheets of insulation to the gauge proved ineffective. The insulation had to be closely cropped to the gauge to allow access through the containment cylinder. The glue bond often failed, allowing arcing to the gauge through the test sample. The large insulating disk offered better dielectric coverage but had to be mounted separately through the top of the containment cylinder.

The PVDF pressure transducer, consisted of gold-platted leads on either side of the thin sheet of PVDF material which crossed at one end making two electrodes with a definable active area. This area is poled during manufacture to enhance the piezoelectric properties of the material and to ensure calibration of the transducer. The signal typically obtained from these devices is directly related to the change in charge per unit time, **dq/dt**, which yields **dP/dt**, where **P** is the pressure. A simple capacitive integrating circuit, attached to the leads at the other end of the gauge, was used to transform the signal to a measure of the charge which allowed direct conversion to pressure during data reduction on a computer. This technique, referred to as the charge mode, circumvents possible errors associated with numerical integration resulting from bit errors incurred from the digital scopes. A 50 Ω resistor was placed in series between the integrating capacitor and the cable to separate the two electrically.

21

The divergent nature of the shock wave coming from the arc channel induced two other sources of error in the pressure measurements. These errors were due to multidimensional strain and a poorly defined affected area. The area of the sensor affected by any disturbance must be known in order to obtain an accurate measurement of the pressure. This becomes problematical for a divergent wave since the entire active area will not be uniformly affected. The rise-time of the measured voltage-time record is affected as the divergent wave initially impinges on the gauge. Following the pressure front a slower-building strain profile is established in the gauge from the two-dimensional divergence of the shock wave. This results in an error because the gauge is sensitive to changes in multidimensional strain. The active area was kept small to minimize these errors.

IHTR 1925

Chapter 4

EXPERIMENTAL RESULTS AND DISCUSSION

In this chapter data from the diagnostics, discussed in the previous chapter, are used to quantify the temperature, size and density of the arc channel and indicate how the arc channel induces ignition in the propellant.

The data and discussion concerning ignition are presented first. Time to ignition data are used to dismiss shock ignition for millijoule electrical discharges and to infer that reaction occurs in localized areas along the length of the arc channel. The smallest energy that produced ignition in these studies was 160 ± 1.4 mJ.

A number of observations concerning the arc channel development are made in this chapter. Pressure transducer measurements in inert samples are reported and used to infer that the arc channel expands as a result of a hydrodynamic process. Spectrographic data are used to determine the temperature of the plasma associated with the arc channel.

Photographic data of arc channel expansion are reported and used to fit an analytical expression. Post test observations are used to make inferences concerning the initial formation of the arc channel and decomposition of binder material due to radiation from the arc channel. The electrical data from these experiments are used to compare resistance-time profiles to infer that aluminum concentration affects the initial size and expansion of the arc channel. The information concerning the initial formation of the arc channel is used with the arc channel expansion data to estimate the density of the plasma at the end of the discharge.

Dismissal of Shock Ignition Mechanisms

Three scenarios were considered as possible mechanisms for ignition in this study: prompt shock ignition in the solid from the rapid expansion of the arc channel, shock ignition following a latent thermal explosion of a heated volume of the material, or a thermal ignition process defined by heat conduction from the channel to the surrounding material. All three scenarios may be valid for different regimes of electrical stimulus defined by the magnitude and the rate of electrical energy deposition, however, in light of the data, the latter is the dominant mechanism for short duration millijoule discharges.

Observations with infrared detectors indicated times to reaction on the order of 5.7 ± 0.2 ms. (The time to reaction was taken to be the time the detector signal began to increase in magnitude; ignition was defined as sustained reaction and determined by the total consumption of the sample.) The late times to reaction exclude the possibility of prompt ignition from the shock established by the expanding arc channel. Ignition times on the order of microseconds would have been expected for this mechanism.

PVDF pressure transducer records taken in an attempt to observe a secondary shock failed to show any stress waves at the recorded ignition time. This suggest that there is no latent thermal explosion of chemically reactive constituents trapped in the arc channel, thereby dismissing the mechanism of shock ignition via thermal explosion for short duration millijoule discharges.

23

Having eliminated the other two mechanisms, thermal energy transfer from the arc channel to reactive constituents in the solid matrix surrounding the arc channel is the viable ignition mechanism.

Indication of Discreet Ignition Sites

Infrared observations were made for both the bulk breakdown and surface discharge configurations to measure ignition times. Large increases in infrared emissions were observed between 8 to 13 ms with the surface discharge configuration, while those observed with the bulk breakdown configuration varied from 5.7 ms to hundreds of milliseconds. These results suggest that the reaction starts in localized sites along the length of the discharge. Once established, the reaction propagates along the length of the arc channel. For the bulk breakdown configuration, this creates the illusion of longer induction times since the reaction takes time to reach the observation point, i.e., the hole in the low voltage electrode. The opacity of the test samples excludes detection of infrared emissions until the reaction reaches the low voltage electrode. Despite the arc channel's forming beneath the surface in the surface discharge configuration, the channel is shallow enough for the light to be detected along the length of the channel. Since the entire channel length is in view of the collecting optics, the recorded times to ignition were more repeatable with the surface discharge arrangement.

Lowest Ignition Energy Observed

There are a number of parameters that can affect the minimum ignition energy that an experimental apparatus will observe. The most notable of these parameters is containment of the hot gas produced by the electrical discharge. This phenomenon was addressed by the application of a 1.8 kN (400 lbf) force and vacuum over test sample surfaces in contact with the electrodes. However, this parameter was not studied, so a minimum ignition energy was not determined. The best that can be reported is the lowest ignition energy observed for this experimental arrangement.

The lowest observed ignition energy for the bulk discharge configuration was 160 ± 1.4 mJ. Two experiments produced these results. These experiments employed a 50 ns discharge cable initially charged to 30 kV. This is comparable to an ignition energy of 186 mj produced with a 100 ns discharge for a charging voltage of 20 Kv. (Note that these experiments were outside the operation range used to characterize the arc channel expansion.) The time to ignition for these two experiments was 5.7 ± 0.2 ms. These were the lowest ignition times observe in either the bulk breakdown and surface discharge arrangements.

PVDF Transducer Measurements in Inert Samples

The electrical responses of PVDF transducers were measured for cylindrical stress waves generated from electrical discharges in the inert solid. The results indicate that the arc channel hydrodynamically expands in relation to the deposition of electrical energy.

Three different parametric studies were performed wherein the discharge time, energy deposition rate, and energy deposition were held constant, respectively. The signal shown in Figure 7 was from a transducer located 3.18 mm from the discharge gap where 514 mJ was deposited. The signal peak was 1.03 V (≈ 5.2 MPa). (Signal magnitudes are given in volts.) The rise time of this signal, defined as the time between 10% and 90% of full magnitude, was 430 ns and its duration, defined as the time between the 90% points on either side of the peak, was 300 ns.
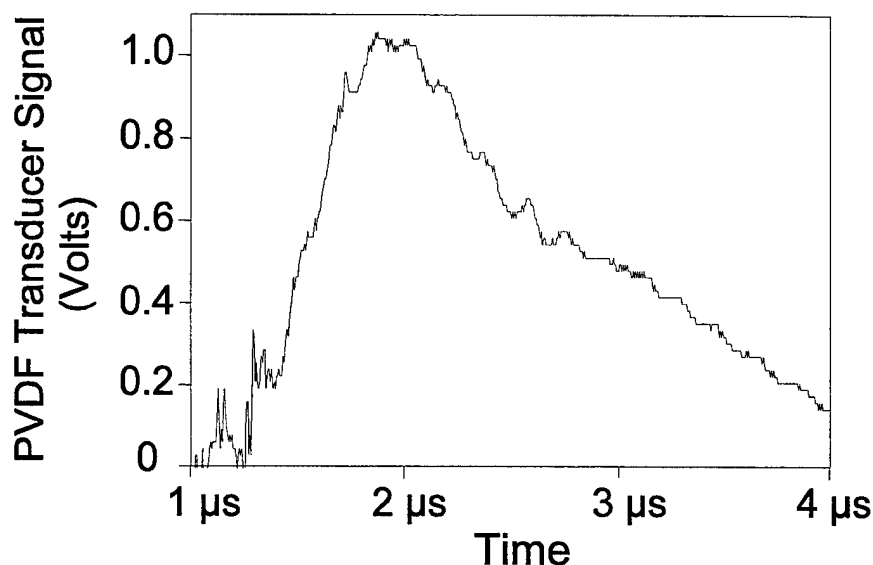
**Figure 7. PVDF Transducer Signal 3.18 mm from the Discharge Gap
Where 514 mJ Was Deposited**

Two series of experiments were performed to investigate the effect of holding the discharge time constant (100 or 300 ns) while varying the power and energy associated with the discharge. This was accomplished by using the same cable for a given series and increasing the initial charging voltage for successive experiments. These early studies departed from the usual arrangement in that a 6.35 mm test sample was used in conjunction with a 6.35 mm PMMA disk, behind the gauge, for confinement. Increasing transducer signals corresponding with increasing power and energy deposition indicated that differences between discharge parameters could be distinguished by the PVDF transducer.

Three experiments were performed where the near rectangular power profile was maintained around 1.6 MW for successive increases in deposition energy. This was accomplished by charging different lengths of cable to 20 kV. The different discharge times provided the change in energy. The gauge was placed at a distance of 3.18 mm from the discharge gap. The data show increasing transducer response with increasing energy deposition. The peak signals from the transducer 0.33 V ($\approx$1.8 MPa), 1.28 V ($\approx$4.9 MPa), and 1.65 V ($\approx$6.3 MPa) correspond to energy depositions of 141 mJ/100 ns, 519 mJ/300 ns, and 693 mJ/400 ns respectively.

Experiments were performed using nominal discharge times of 100, 200, 300, and 400 ns, where the energy deposited was maintained between 470 and 516 mJ. Variations in the discharge parameters made it impossible to achieve identical energy depositions between experiments. However, these experiments were conducted by charging different lengths of cable to selected voltages to yield similar deposition energies. The data show similar transducer responses at 3.18 mm from the discharge gap for different discharge times and powers when the electrical energy deposition is about the same value. The initial parameters, characterized by the charging voltage and nominal discharge time, were 37 kV/100 ns, 25 kV/200 ns, 20 kV/300 ns, and 17 kV/400 ns which corresponded to electrical powers of 5.19, 2.57 and 2.35, 1.53, and 1.0 MW respectively. The peak signals from the transducer were 1.05 V ($\approx$5.3 MPa), 1.15 V ($\approx$5.6 MPa) and 1.11 V ($\approx$5.6 MPa), 1.07 V ($\approx$5.4 MPa), and 1.03 V ($\approx$5.2 MPa) respectively. Rise times and signal durations were nearly identical.

25

The stresses were obtained from the one-dimensional gauge calibration[26] ignoring the effects of multidimensional divergent strain. The observed signal is affected by non-uniaxial strain and coupling effects between the gauge and the material in which it was included. Voltage contributions occur due to non-one-dimensional piezoelectric coefficient in the stress-strain matrix. Correcting gauge records for multidimensional strain is a current research problem and beyond the scope of this study.

The curvature of the wave coming from the arc channel affects the gauge response, due to 3 poorly defined components: (1) the affected area over the transducer element, (2) non-uniaxial strain and (3) the gauge/matrix coupling (Gupta 1983) The cross-sectional area of the sensor affected by any disturbance must be known in order to obtain an accurate measurement of the stress. (Figure 6 in Chapter 3 shows the cross-sectional area of the transducer sensor.) This becomes difficult for a divergent wave since the entire active area will not be uniformly affected. This affects the perceived rise time of the pressure front as the diverging wave initially impinges on the gauge. The rise times resulting from this effect are expected to be 146 ns and 76 ns at 3.18 mm and 6.35 mm from the discharge gap respectively. These rise times were calculated given the 9 mm^2 active area and assuming a cylindrical shock originating at the center of the arc channel with a wave speed of 2.3 mm/μs. The calculated rise times are much smaller than those observed, 430 ns and 550 ns at the respective distances. Hence, the active area of the gauge does not explain the long rise times observed.

The results do suggest that the mechanical disturbance established by the arc channel is determined by the magnitude of the energy deposition, not the deposition rate, for short duration electrical pulses. The transducer records are consistent with the description of arc channel expansion as a hydrodynamic process.

All the effects of short duration discharge times (100 to 400 ns) on the mechanical response of the material can not be completely resolved with observed signal rise times greater than 400 ns. Better resolution of the effects of short duration discharges would require closer placement of the gauge and proper strain compensation.

Temperature of Plasma in Arc Channel

Temperature measurements were made by comparing spectrographic data between 450 nm and 620 nm to blackbody curves. Spectra were acquired for two parametric studies over different intervals during 300 ns discharges produced by an initial charging voltage of 24 kV, and at the end of 300 ns discharges where the charging voltage was varied from 20 to 36 kV. In each case the temperature of the plasma in the arc channel was determined to be 13,000 K for both the inert and the propellant.

The intensifier for the linear array at the image plane of the spectrograph was gated to observe the spectrum at a different time during each experiment. The observation window was 40 ns. Observation times varied from 100 ns to the end of the discharge. Observations at times earlier than 100 ns were not possible because the arc channel did not emit enough light for the spectrometer at these times. The current magnitude was varied to determine the effect on the spectral data. In each case the spectral data were comparable suggesting that they neither change over the course of the discharge nor for increasing values of power and energy deposition. The spectra are similar for inert and propellant samples. Note that this result also held for propellant samples that did not ignite. The data were matched with a normalized blackbody curve corresponding to 13,000 K, see Figure 8.
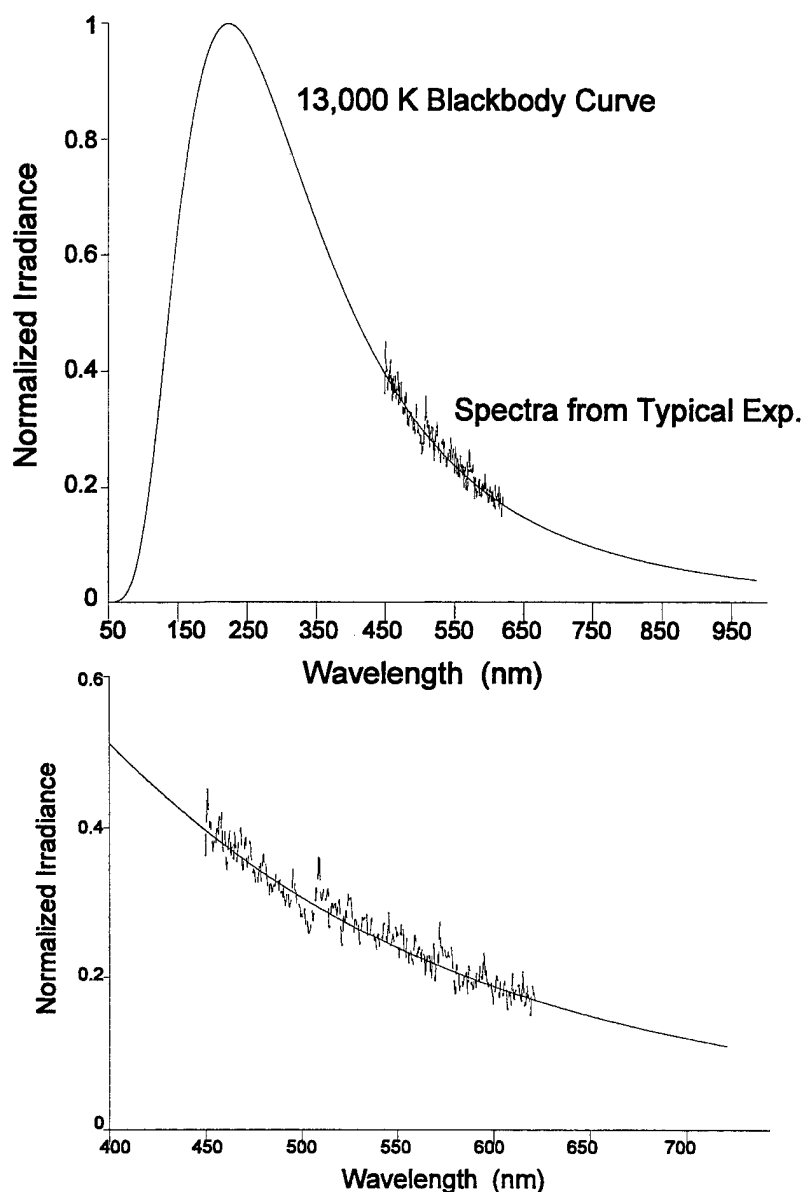
Figure 8. Observed Spectral Data Matched to a 13,000 K Blackbody Curve (Full Curve and Expanded Region of Interest)

The constancy of the temperature over the course of the discharge and for increases in current magnitude suggest that an equilibrium is established in the plasma during the initial stages of the discharge. Assuming that the energy expended on dissociation and ionization is minimal following the initial formation of the arc channel, the discharge energy is largely converted to work done in expanding the channel. This would mean that the equilibrium is between electrical energy deposition heating the plasma and expansion of the plasma.

27

Arc Channel Expansion

The evolution of internal arc channels in 6.35 mm thick samples of the ASRM propellant and its inert simulant were quantified by measuring the diameter of images recorded by an Imacon framing camera. The image was magnified by a factor of 5.9 using photographic lenses. The diameters of these images were determined with a traveling microscope using a digital readout with a resolution of 2 μm. The errors associated with this photographic technique are discussed in Appendix B.

Acceptable photographic images of dynamic arc channel growth were selected from experiments using different f-stop settings of 2.8, 4, and 5.6. The use of these settings, which altered the opening in an aperture in the lens, was required to compensate for variations in light intensity between experiments. The change in light intensity between experiments was in part due to different channel sizes and differences in the amount of vacuum grease applied to the test sample surface. Furthermore, more exposure was required to resolve the channel during the early part of the discharge and less exposure for the latter portion of the discharge. Complete description of the channel evolution had to be realized from different photographic settings employed over a number of different experiments.

The arc channel expansion was observed for different discharge characteristics defined by the current, power, and energy deposition. The nominal discharge time for these studies was 400 ns as determined by the length of the cable. Figures 9 and 10 compare the current and voltage profiles for each experimental variation for the ASRM propellant and its inert simulant respectively. These variations were established and hence designated here by the initial charging voltage on the cable. Voltages of 24 and 28 kV were used to quantify the expansion of a single discharge channel in the propellant because these voltages could induce prompt dielectric breakdown in the test sample. (Voltages of 20 and 24 kV were used for the inert simulant for the same reason.) An example of delayed breakdown is given in Figure 11.

The shift in operating voltages from the propellant to the inert simulant was due to the higher aluminum concentration in the inert. The aluminum concentration in the inert was 27.17 % by weight compared to 19 % in the propellant. Corresponding increases in electric field strengths across the material, resulting from increased initial voltages, are enhanced by the presence of the fine aluminum particles in the material and thereby affect the breakdown process. Higher concentrations of aluminum serve to increase the effect of electric field enhancement.

Higher voltages typically produced multiple discharge channels invalidating analysis for those experiments. The effect is governed by the presence of aluminum and hence altered by different aluminum concentration as well. The presence of secondary channels resulted in smaller than expected channel sizes. Discharge data for 32 kV and 28 kV in the propellant and the inert respectively are given in the figures and tables for comparison. The existence of secondary channels in the inert was discovered in post-test dissections of test samples. The existence of multiple channels in the propellant had to be inferred from the observations in the inert since the propellant always ignited and was subsequently consumed.
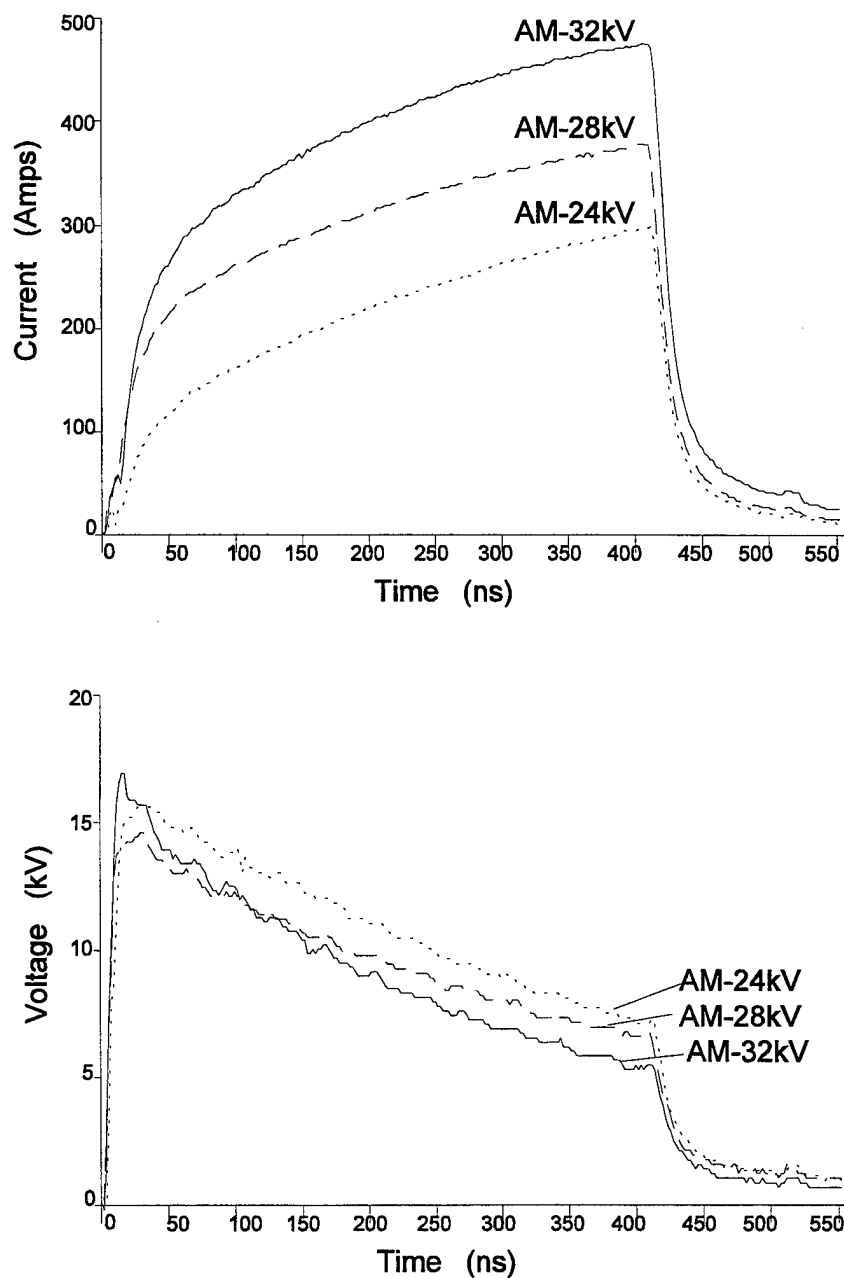
Figure 9. Comparison of Current and Voltage Profiles Resulting from Different Initial Charging Voltages for ASRM Propellant
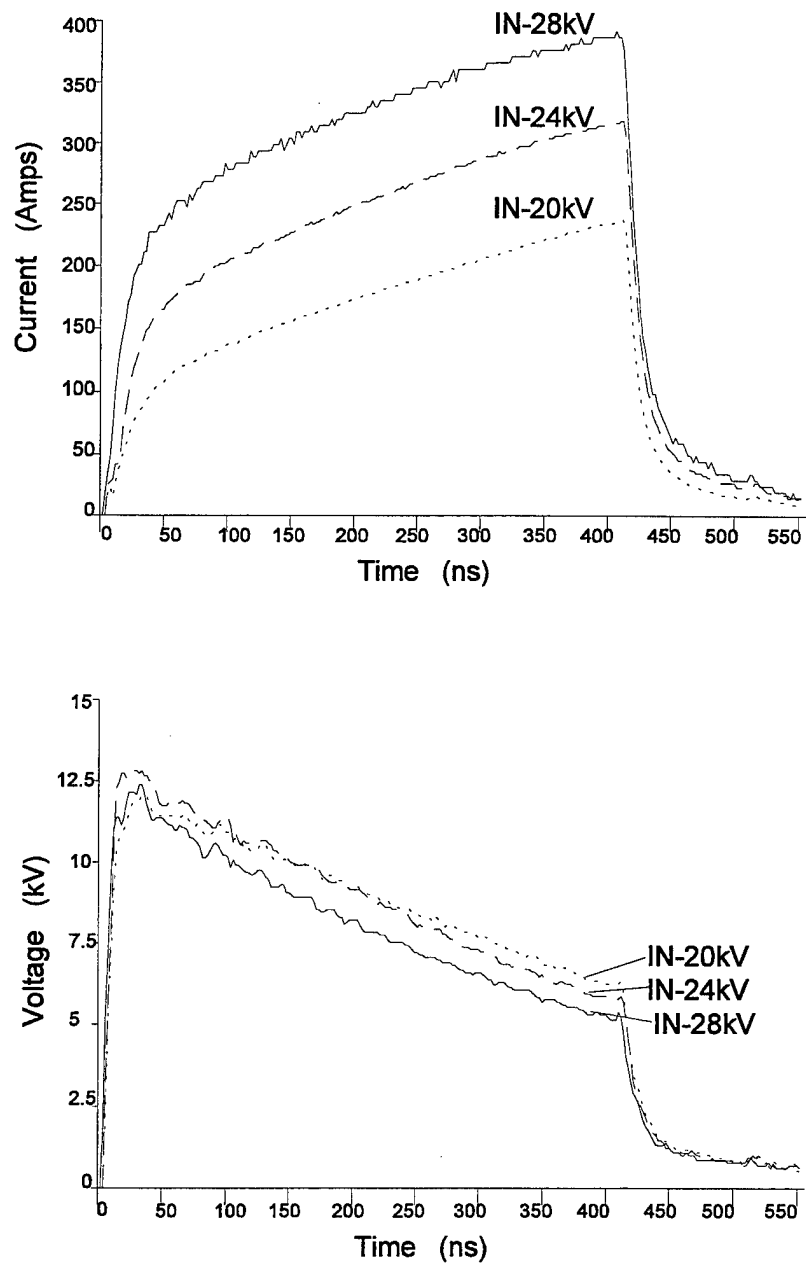
Figure 10. Comparison of Current and Voltage Profiles Resulting from
Different Initial Charging Voltages for the Inert Simulant

30
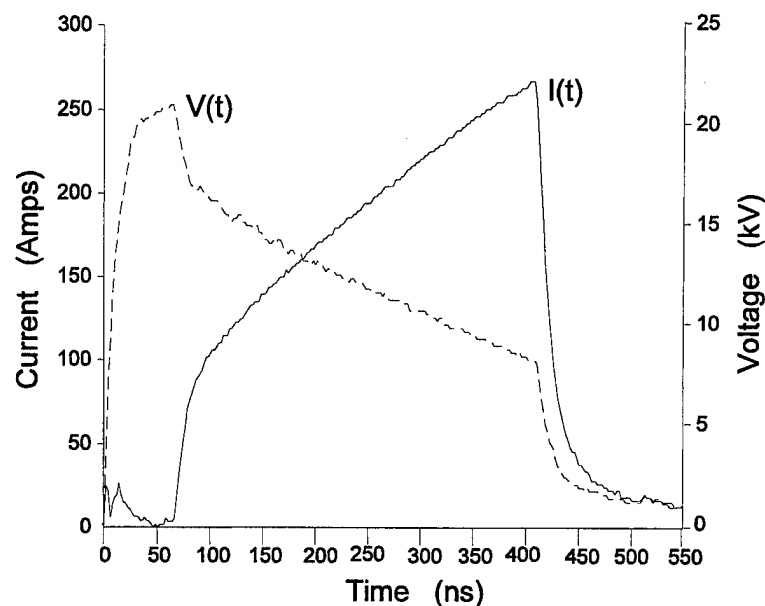
Figure 11. *Current and Voltage Profiles Representing Delayed Dielectric Breakdown in the ASRM Propellant*

Both materials experienced a certain delay in breakdown. This provided some difficulty in comparing the results. Only tests that displayed a breakdown delay less that 20 ns were accepted for analysis. A number of experiments were performed for each experimental change to establish an average result. All the data concerning arc channel expansion for those experiments selected for analysis are given in Appendix B with the error analysis. The averages of initial and final channel radii for the experiments described above are given in Tables 4-1 and 4-2 for the propellant and the inert simulant respectively. The overall error associated with these values are given with the respective value in each table.

Analytical Expression for Arc Channel Expansion

The intent of the photographic study was to determine the relationship between the arc channel expansion in the composite solid, and the discharge characteristics. Tables 4-1 and 4-2 also include the coefficient, K_w, from the analytical expression for arc channel expansion. It is desirable to predict the arc channel size for different discharge characteristics. To this end, the analytical expression developed in Appendix A was compared to the experimental results in Appendix B. This expression, shown below, describes the arc channel radius as a function of electric power:

$$a(t) = K_w [\int_0^t W^{\frac{1}{3}} dt]^{\frac{3}{4}} \qquad (4\text{-}1)$$

where $a(t)$ is the radius of the arc channel, W is the electrical power, and K_w is a constant which contains-material specific quantities which are given in Appendix B. Throughout this report values of K_w that are given will yield the radius in micrometers when multiplied by the integral expression above.

31

Table 4-1. Arc Channel Expansion Data for ASRM Propellant Using a 400 ns Discharge

Charging Voltage	Nominal Deposition Energy	Nominal Discharge Power	Observed Initial Radius $a_i \pm e_{ai}$* (μm)	Observed Final Radius $a_f \pm e_{af}$* (μm)	Channel Expansion Rate (m/s)	Analytical Constant K_w** (x 10^3)
24 kV	850 mJ	2.1 MW	29.8 ± 16.4	61.8 ± 21.4	75.3 ± 13	58.3 ± 10.1
28 kV	1150 mJ	2.9 MW	35.4 ± 16.6	76.5 ± 17.4	86.2 ± 10.2	63.6 ± 7.5
32 kV	1350 mJ	3.4 MW	—	50.2 ± 15.8	Multiple Channels Assumed	

* The total errors, e_{ai} and e_{af} for the initial and final observed radii are reported in the table.
** The values for K_w yield the radius in micrometers when multiplied by the integral expression for the arc channel radius.

Table 4-2. Arc Channel Expansion Data for Inert Simulant Using a 400 ns Discharge

Charging Voltage	Nominal Deposition Energy	Nominal Discharge Power	Observed Initial Radius $a_i \pm e_{ai}$* (μm)	Observed Final Radius $a_f \pm e_{af}$* (μm)	Channel Expansion Rate (m/s)	Analytical Constant K_w** (x 10^3)
20 kV	600 mJ	1.5 MW	not observed	54 ± 15.8	115.4 ± 8	97.5 ± 6.8
24 kV	850 mJ	2.1 MW	18.7 ± 16.3	59.7 ± 17	110 ± 3.6	86.8 ± 3.0
28 kV	1020 mJ	2.5 MW	—	40.9 ± 14	Multiple Channels Observed	

* The total errors, e_{ai} and e_{af} for the initial and final observed radii are reported in the table.
** The values for K_w yield the radius in micrometers when multiplied by the integral expression for the arc channel radius.

The analytical expression may be expressed as $a(t) = K_w I_w(t)$, where $I_w(t)$ is the value of the integral expression at time t. Using this notation, the value for K_w was determined from the average values of initial and final channel radii. A curve was fit through the data observed between 162 and 420 ns using a linear least squares fit. Values for K_w were selected for each experimental situation, i.e., changes in material and initial voltage, so that the slope for $K_w I_w(t)$ would match the slope of the least squares fit. The predicted curve was then shifted by a constant so that the two curves would overlay one another. The values for K_w are given in Tables 4-1 and 4-2.

Figure 12 offers comparisons between representative data from photographs and the above analytical expression (the solid line) for the propellant with charging voltages of 24 and 28 kV. Similar data for the inert with charging voltages of 20 and 24 kV are given in Figure 13. The photographic data make a satisfactory match with the curve predicted for the propellant by Equation 4-1. The initial channel radii determined from the above analysis compare favorably with observations reported in Table 4-1. For a charging voltage of 24 kV, the analytical expression predicts a radius of 27.2 μm at 24 ns and the corresponding experimental average is 29.8 μm. For the inert, the correlation between the predicted curve and the observed radius at 24 ns appears to be not as good. The predicted value for a charging voltage of 24 kV is 9.6 μm compared to the observed average of 18.7 μm. Despite this discrepancy, the predicted curve remains believable since the initial channel radii for the inert was comparable to the resolution of the camera system.
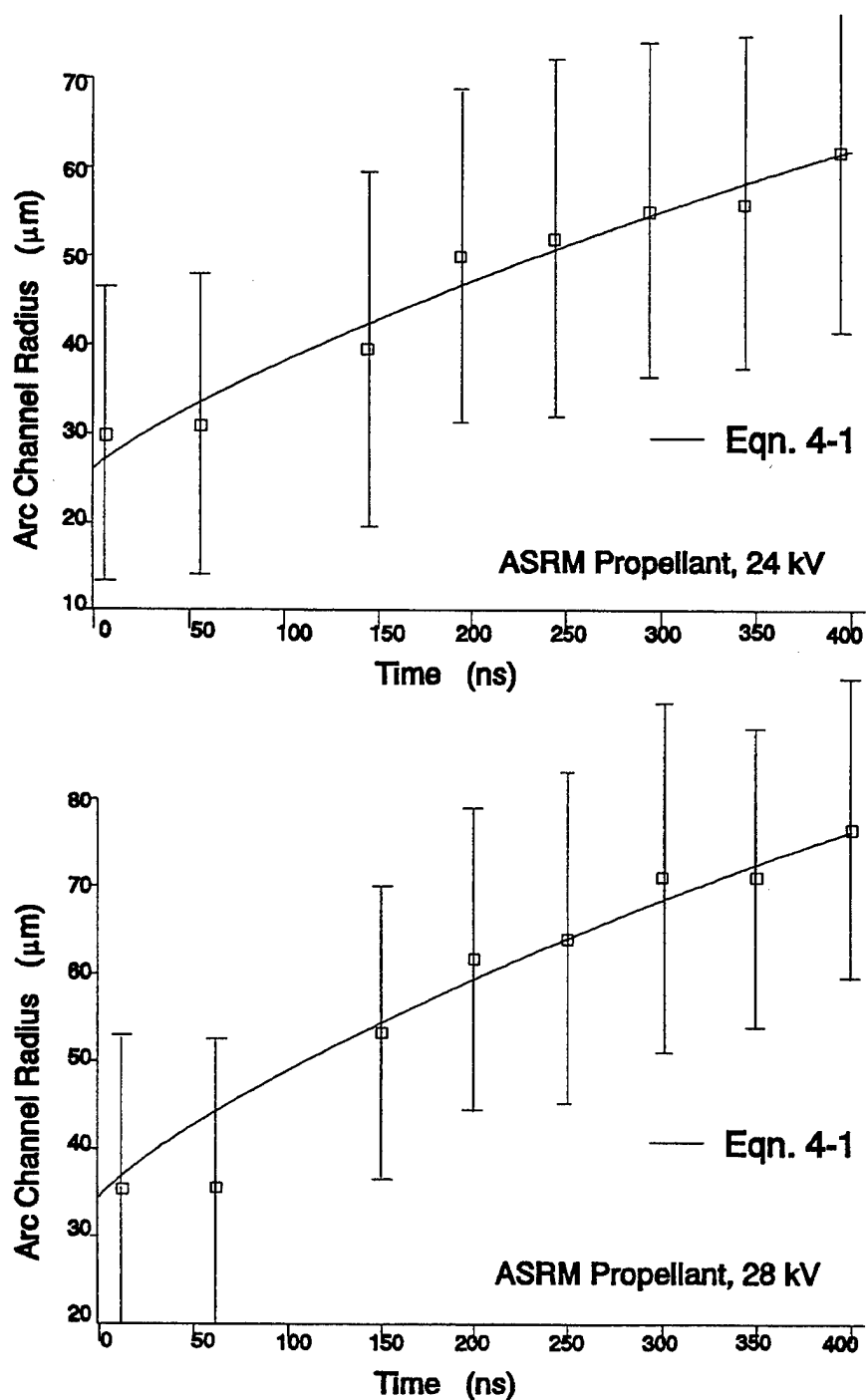
Figure 12. Predicted Arc Channel Radius Compared to Averaged Photographic Data for ASRM Propellant
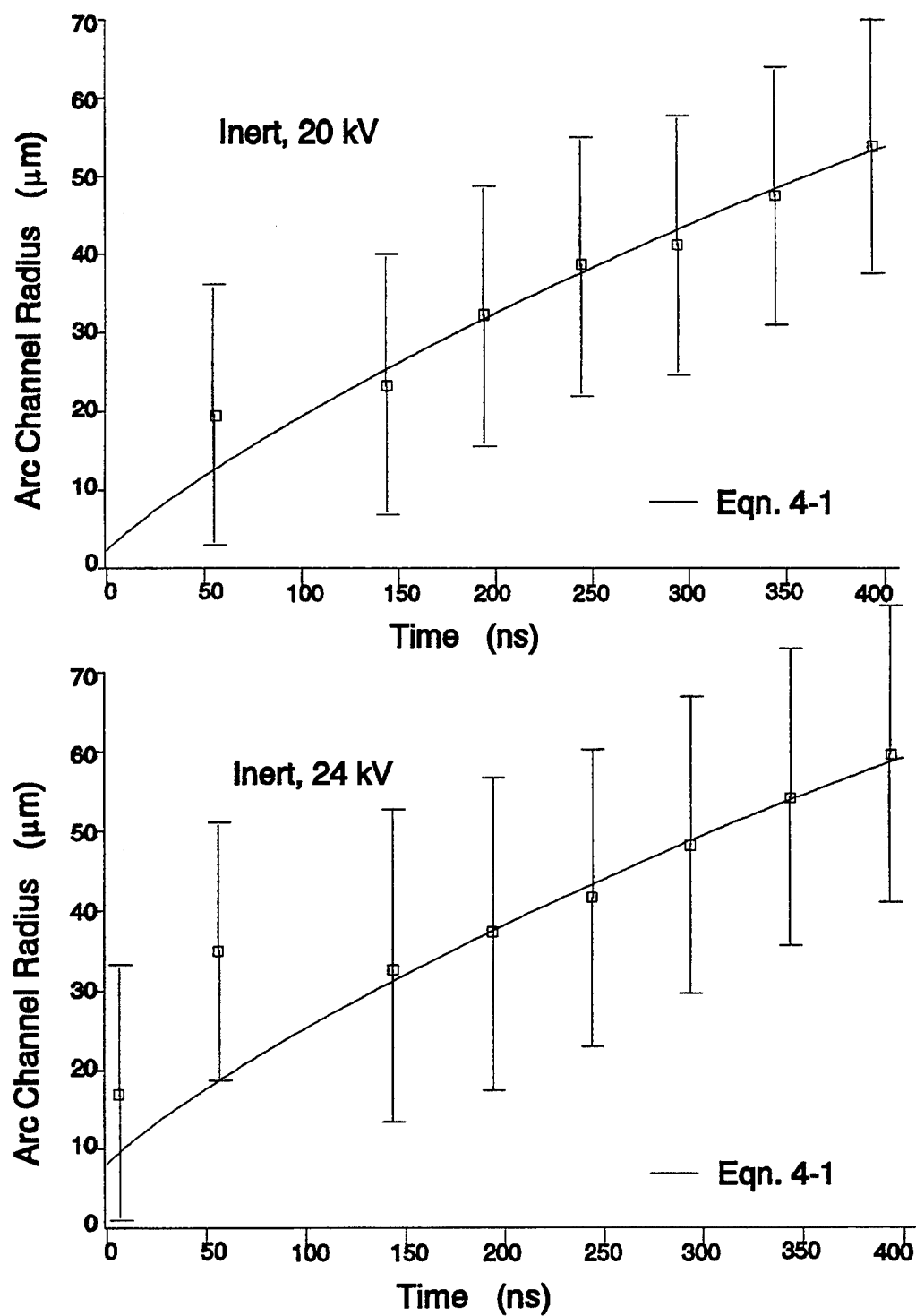
Figure 13. *Predicted Arc Channel Radius Compared to Averaged Photographic Data for Inert Simulant*

34

Post Test Observations of Inert Test Samples

Post test dissection of inert samples revealed that the cavities, resulting from the arc damage, were between 25 μm (1 mil) and 75 μm (3 mils) in diameter. The diameter of the cavity was measured after bisecting the blackened region left by the electrical discharge. The bisection was accomplished by cleaving through the test sample with a thin scalpel. No definite trend was established between bisected cavities and discharge characteristics. Note, that the size associated with the cavity is very much smaller than the final dynamic arc channel size, however, these values do compare favorably with the diameters observed for the initial arc channel radius at 24 ns.

Post test channels produced in inert samples were observed to weave around the crystalline constituents, i.e., KCl. This phenomena is assumed for the AP crystals in the propellant. These results suggest that the arc channel is initially formed in the binder material between closely associated aluminum particles thereby including those aluminum particles.

Decomposition of the binder material was observed as a blackening of the material surrounding the post discharge cavity. The blackened region was irregular in size, varying in diameter along the length of the cavity. The diameter of the blackened region could be as large as 1 mm. Blackened regions beyond the area immediately surrounding the post discharge cavity were observed on the opposite sides of KCl crystals. It is possible that these regions sustained damage due to radiation passing through the KCl crystal and being absorbed by the binder/aluminum matrix that surrounds the AP.

Comparison of Measured Resistance Curves

Resistance profiles in time, determined from the ratio of the voltage and current data, follow an explicable trend of decreasing resistance corresponding to increasing channel size. Figure 14 compares average resistance profiles for both materials. Average profiles were obtained for a number of experiments corresponding to different charging voltages. The resistance starts high and declines over the course of the discharge. It is expected that the resistance will decrease as the channel increases in diameter and the density of the plasma decreases. Note that the resistance profile shifts to smaller values for increased charging voltage. This effect is in accord with increased channel size due to increased energy deposition observed photographically. The data show that changes in resistance are due to changes in arc channel radius.

Comparisons of measured resistance curves between materials indicate that the arc channel resistance in the propellant is higher than that in the inert simulant, as can be seen in Figure 15. The average resistance curves for 24 and 28 kV experiments in the propellant are comparable to those for 20 and 24 kV in the inert simulant respectively. Since the arc channel was larger in the propellant these results suggest that the conductivity of the arc channel in the propellant is smaller than that in the inert simulant.

For the ASRM Propellant
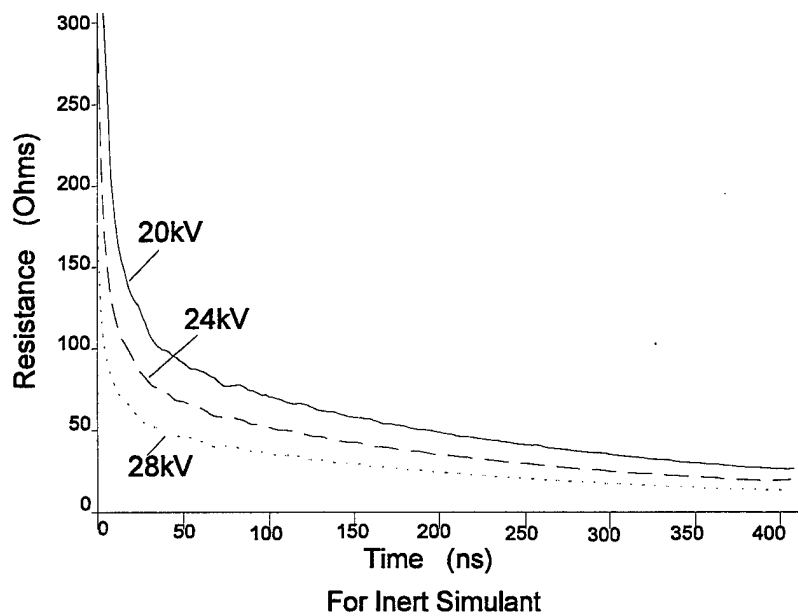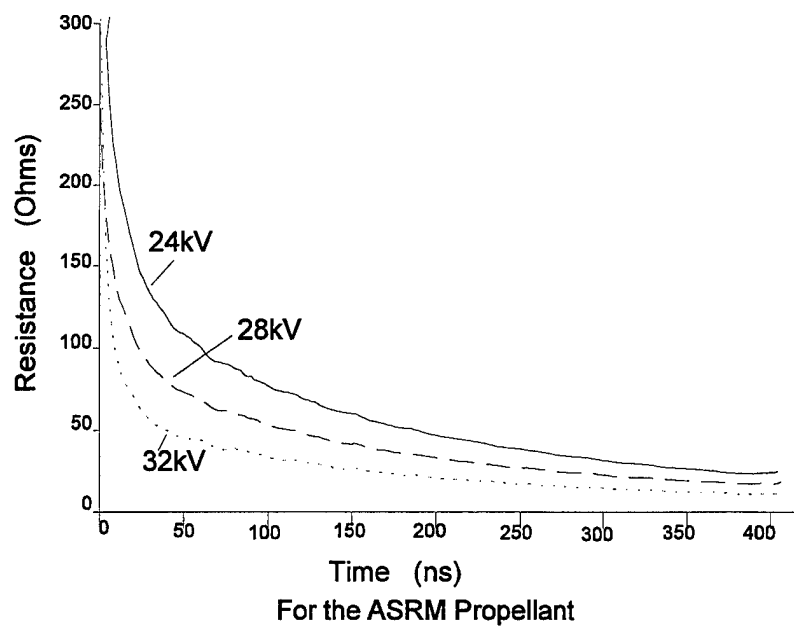
For Inert Simulant

Figure 14. Measured Average Resistance Curves for Different
Discharge Characteristics for the ASRM Propellant
and its Inert Simulant
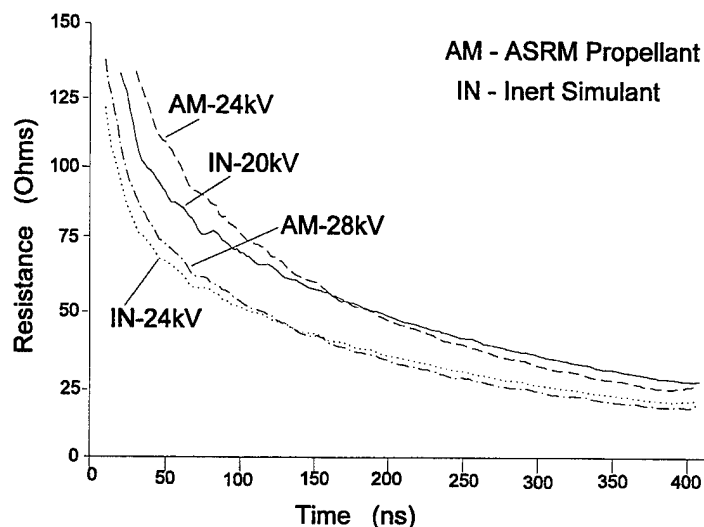
**Figure 15. Measured Resistance Curves for Selected Charging
Voltages for the ASRM Propellant Compared to Those
from Inert Simulant**

The propellant and the inert differ in two respects, crystalline constituents (AP and KCl respectively) and aluminum concentration (19% and 27.2% respectively). Since the arc channel forms in the binder material between the aluminum constituents but around the crystalline constituents, the differences in average resistance profiles are attributed in part to the differences in aluminum concentration. Note that the aluminum is as good electrical conductor, so its presence in the plasma will increase the conductivity of the arc channel. Variations in initial channel size can be attributed to the presence of the aluminum as well. (Note that the initial size of the arc channel varied with initial charging voltage and changes in material.) The arc channel is established when the electric field exceeds the dielectric breakdown strength of the material. This critical electric field may be achieved at relatively moderate voltages due to the presence of the aluminum in the solid. The small aluminum particles serve to enhance the electric field in the material thereby inducing failure at lower voltages. (Note that the propellant required a higher breakdown voltage on average than the inert samples because of the lower concentration of aluminum in the propellant.) The initial size of the arc channel is established during this process. The modification of the electric field due to different aluminum concentrations serves to control the breakdown process and affect the initial size of the arc channel.

Final Density of Plasma

In this section the final density of the arc channel plasma is estimated by assuming the mass corresponded to that for the binder material in the initial channel size. (These calculations require the volume percentages for the binder and the aluminum in the binder/aluminum matrix given in Tables 4-3 and 4-4 for the propellant and inert respectively.) This is reasonable since the diameter of post-discharge cavities in inert samples were comparable to photographically measured diameters of the arc channel at the beginning of the electrical discharge. Furthermore, this cavity was observed to weave a convoluted path around the crystalline constituents indicating that the arc channel forms between the aluminum in the binder. The mass and volume of the aluminum are excluded in this calculation because there is not enough energy in the plasma to evaporate the aluminum.

Table 4-3. Constituent Percentages for Propellant and its Binder/Al Matrix

Constituent	Density kg/m^3	%Mass Material	%Volume Material	%Mass binder/aluminum matrix	%Volume binder/aluminum matrix
AP	1950	69%	64%	—	—
Al	2700	19%	12.7%	61.3%	35.3%
Binder	931	12%	23.3%	38.7%	64.7%

Table 4-4. Constituent Percentages for the Inert and its Binder/Al Matrix

Constituent	Density kg/m^3	%Mass Material	%Volume Material	%Mass binder/aluminum matrix	%Volume binder/aluminum matrix
KCl	1990	58%	52.8%	—	—
Al	2700	27.2%	18.1%	64.6%	38.4%
Binder	931	14.8%	29.1%	35.4%	61.6%

The statement that the aluminum does not vaporize is supported by following example where the electrical energy deposition for the 24 kV experiment featured in Table 4-1 is compared to the energy required to vaporize the amount of aluminum in the arc channel. The volume percentage of aluminum in the volume defined by the initial arc channel radius, 29.8 μm, is assumed to be equivalent to the volume percentage of aluminum in the binder/aluminum matrix given in Table 4-3 for the propellant. The mass corresponding to the volume given the density of aluminum is 18.3 μg. The energy required to evaporate this mass is 145 J using 7.9 MJ/g for the heat of evaporation (Chemical Propulsion Information Agency, n.d.). This is several orders of magnitude larger than the electrical energy deposition of 850 mJ measured for the discharge. So the aluminum does not have enough energy to evaporate.

There is, however, enough energy to gasify the binder. Lengelle et al,[28] reported that the heat of degradation for HTPB is 2.72 kJ/g. Since the binder is made up of mostly HTPB, its mass in the volume defined by the initial radius for the example above can be determined from the volume percentage of binder in the binder/aluminum matrix and binder density given in Table 4-3. This mass is 10.2 μg and the amount of energy required for gasification is 28 mJ.

The expression used to estimate the final density is developed in Appendix B and given below:

$$\rho_f = \frac{k_{\%B}\,\rho_B}{\dfrac{a_f^2}{a_i^2} - k_{\%Al}} \tag{4-2}$$

where a_i and a_f are the respective initial and final radii of the plasma column, ρ_B is the density of the binder, and $k_{\%B}$ and $k_{\%Al}$ are the fractional coefficients corresponding to the volume percentages for the binder and aluminum in the binder/aluminum matrix. These percentages are given in Tables 4-3 and 4-4 for the propellant and inert respectively.

The density for the 24 kV experiments was estimated using the averaged initial and final channel radii of 29.8 and 61.8 μm respectively. The fractional coefficients for the volume percentages for the binder and aluminum in the propellant were 0.65 and 0.35 respectively. The density of the binder was 931 kg/m^3. This yields a plasma density of 150 ± 66 kg/m^3. (The high error is due to the errors associated with the respective channel radii.) The evolution of the mass and its eventual ionization were not characterized in this study. It is assumed that the binder mass is completely gasified by the end of the discharge.

Chapter 5

THE ARC CHANNEL AND AN ENERGY-TRANSPORT IGNITION MODEL

There are three sections in this chapter. The first section is a general overview of an arc channel that forms in a heterogeneous material. The second section uses an idealized view of the arc channel (a perfectly cylindrical plasma column) to present an ignition model based on energy transport from the arc channel. Potential ignition mechanisms are also discussed in this section. The third section presents the results from XCHEM computer simulations used to model one of the ignition mechanisms.

Overview of the Arc Channel

The arc channel, as depicted in Figure 16, forms in the propellant between the aluminum particles, weaving a convoluted path around the AP crystals. (This statement is supported by post test dissections of inert samples which showed that cavities left by the arc channel did not pass through large KCl crystals.) The arc channel's initial volume and its path through the material are determined during the dielectric breakdown process which occurs as a result of the application of a sufficient electric field. The breakdown process is assisted by the heterogeneous nature of the material and moreover by the presence of small aluminum particles. The arc channel will preferentially form between interstitial boundaries between different constituent regions, i.e., the binder and AP crystals, because the dielectric strength of these regions are typically weaker than the individual constituents. The small aluminum particles serve to increase the electric field through out the entire sample: the effect is more pronounced in the binder/aluminum matrix because that is where the aluminum is situated. The increased field concentration induces failure at lower voltages. (Note that the propellant required a higher breakdown voltage on average than the inert samples because of the lower concentration of aluminum in the propellant.) So the arc channel will form between closely associated aluminum particles. It is assumed, that the material trapped in the initial formation of the channel is the aluminum particles involved in the breakdown process and the HTPB binder existing between these aluminum particles.

Following dielectric breakdown, the established arc channel is a highly localized column of ionized gas which is referred to as a plasma in this report. Confined by the solid, the plasma will remain highly condensed giving rise to non-ideal behavior, i.e., coulomb forces are no longer negligible. The plasma arises from gasification and ionization of the small amount of binder material trapped in the initial volume along the path of the channel. The aluminum trapped in the channel does not vaporize because the energy required to evaporate the aluminum is much larger than the electrical deposition energy. As electrical energy is deposited in this plasma, the physical state of the arc channel (size, temperature, density, etc) is altered in a way that allows the current to increase, i.e., the conductance of the arc channel increases.

Observations of increasing current during the discharge support the hypothesis that the arc channel is primarily made up of gas species. Increasing resistance (decreasing electrical conductance) is typically observed in solids because the mean free path for conduction electrons is reduced due to thermal agitation of the bound atoms, conversely, the mean free path increases in an expanding gas.
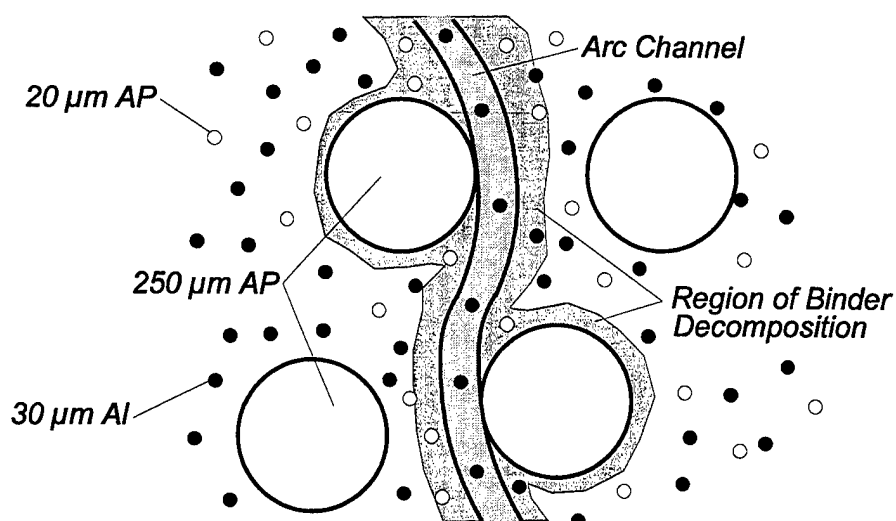
Figure 16. Pictorial View of Arc Channel in Heterogeneous Propellant

Following the formation of the plasma column, continued electrical energy deposition causes the column to expand radially. Ablation of solid constituents from radiated energy deposition is negligible in early times. (A vapor shield, associated with the ablation process, typically requires hundreds of microseconds to become established.[29]) The ablation process is like any other chemical process in that it takes time for the decomposition to occur. It was assumed that ablation is minimal for the short discharge times, hence, the arc channel is primarily thickened as a result of hydrodynamic expansion of the hot plasma evolving in the channel. (This statement is supported by the observation of stress waves propagating in the material following the formation of the discharge channel.) The exclusion of additional mass means that the density of the plasma decreases as the channel expands thereby allowing increased electrical conduction in the plasma as mentioned earlier.

During, and shortly following, the electrical discharge, radiant losses cause a rapid cooling of the plasma and consequential heating of the surrounding solid due to absorption. The effects of this radiation were observed in inert samples; a blackened region, illustrated in Figure 17, surrounded the post-discharge cavity and adjacent AP crystals. This blackening was taken to be decomposition of HTPB binder. The decomposed regions on the backside of KCl crystals indicated that radiant energy absorption was an important finding.

Radiative and thermal conductive transport from the plasma are important aspects because deposition of this energy to the surrounding medium is the stimulus for ignition. Furthermore, energy losses from the initial deposition sites in the reactive medium are important because this can allow the reaction to terminate: the temperature can drop below a level where the decomposition chemistry has not had enough time to become self-sustaining.

41
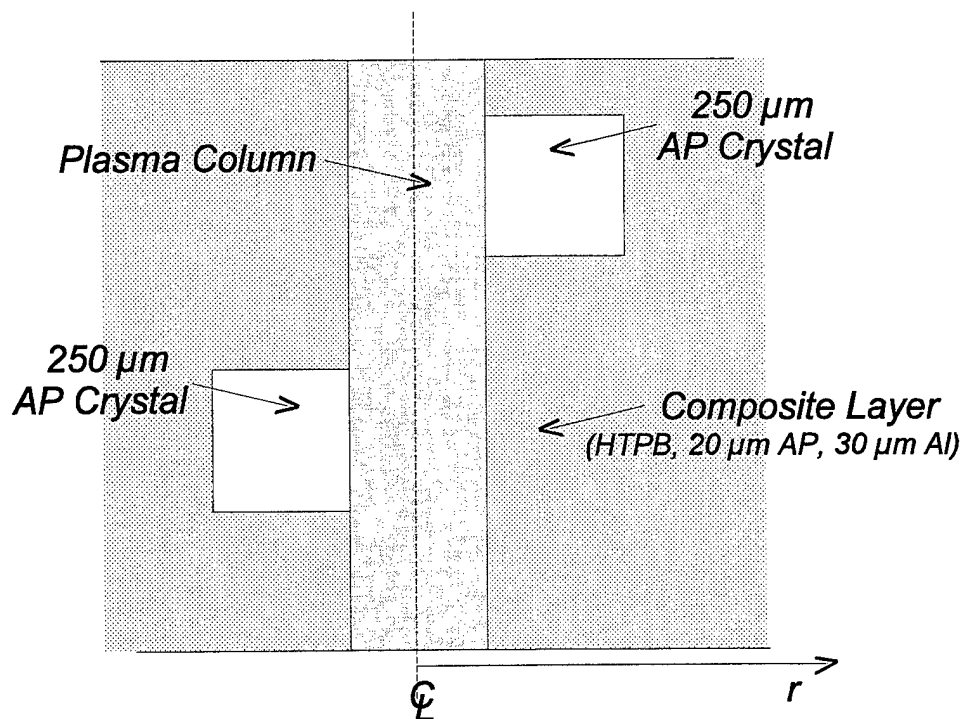
Figure 17. Simplified Picture of Arc Channel for Ignition Model

Energy transfer from the plasma to the surrounding reactive constituents is complicated due to the inhomogeneity of the material. Radiative and thermal conductive transport will vary along the length of the channel depending on whether the portion of the channel in question is completely surrounded by the binder/aluminum matrix or adjacent to an AP crystal.

Idealized Energy-Transport Ignition Model

An idealized ignition model, based on energy transport from the electrical discharge channel to the surrounding reactive media, is presented in this section. This section includes discussions on the reaction kinetics of AP, energy transport from the plasma via radiation and thermal conduction, and three potential reaction mechanisms. It ends with a list of general assumptions for the model. Full implementation of this idealized model is beyond the scope of the present study.

A crossectional view of an idealized system containing a perfectly cylindrical plasma column surrounded by large AP crystals, and a composite layer is shown in Figure 17. (Here, the term composite layer refers to the region containing HTPB binder, 30 μm aluminum, and 20 μm AP crystals; the larger 250 μm AP crystals are designated separately.) The gaseous plasma column is considered to have already been formed with a finite amount of energy, i.e., electrical energy is no longer being supplied.

It is assumed that the aluminum in the channel does no evaporate. (This statement is supported by a comparison of typical energy depositions, less than a joule, to the energy required to evaporate the aluminum trapped in the channel which is two orders of magnitude higher. See the example concerning this in Chapter 4.) Remember that it is assumed the arc channel forms in such a way that AP (the oxidizer) is excluded from the constituents that make up the plasma, hence, there is not enough oxygen available in the plasma for the early times (hundreds of microseconds) to cause any significant reaction with the aluminum in the channel. The HTPB and other minor constituents that make up the binder also do not contain enough oxygen to support a reaction of any consequence.

The plasma column is considered a finite heat source which may be defined in part by the data for arc channel size, temperature, and density determined from this study. Other parameters, not determined in this study, e.g., thermal properties of AP and plasma, radiation losses, radiant energy deposition in AP, and reaction kinetics, must be taken from the literature or deduced from reasonable assumptions.

Ignition occurs in a localized region adjacent to the plasma column where the heating is the most intense. Three reaction mechanisms are active: (1) unimolecular decomposition of adjacent AP, (2) pyrolysis of HTPB binder resulting in an exothermic reaction between the evolving pyrolysis gases and the small AP contained in the binder, and (3) reaction of the super-heated hydrocarbon gas making up the plasma with the AP. (Note that exothermic decomposition of the aluminum is assumed to be negligible.) The two latter mechanisms require determination of the appropriate chemistry so that accurate chemical kinetics can be determined.

Reaction Kinetics of AP: The decomposition of AP is a complex process which leads to products that vary in composition with the decomposition temperature. Multistep reaction kinetics which predict the observed times to reaction from the heavily confined experiments of McGuire and Tarver[30] are not yet available for AP,[31] so a global reaction rate will have to be used.

The evolution of heat in the solid material surrounding the plasma column is determined by the two energy transport mechanisms and self-heating from chemical decomposition. Assuming global decomposition kinetics, the chemical heating rate can be described by the following Arrhenius form:

$$\frac{dN_A}{dt} = -zN_A e^{-\frac{E_a}{RT}} \tag{5-1}$$

where N_A is the mass fraction of undecomposed reactant at any point, its derivative with respect to time is the reaction rate, z is the decomposition rate factor, E_a is the activation energy, Q is the heat of reaction per unit mass, and R is the gas constant which is equivalent to 8.314 J/(mol-K). The rate at which exothermic energy is released, dq_c/dt, is given by:

$$\frac{dq_c}{dt} = -Q\frac{dN_A}{dt} = QzN_A e^{-\frac{E_a}{RT}} \tag{5-2}$$

where q_c is the chemical energy being released as a result of the chemical decomposition. A more detailed discussion on reaction kinetics is given in Appendix C.

Sublimation and decomposition occur simultaneously to varying degree depending on the nature of the AP and experimental conditions, consequently, a variety of values for activation energy and the pre-exponent can be found in the literature.

Radiant energy absorption complicates the reaction kinetics even further. The reaction rate can vary from that typically observed in differential scanning calorimetry (DSC) and differential thermal analysis (DTA) experiments owing to a preconditioning effect from the radiation. A number of researchers have shown that induction times decrease and reaction rates increase after AP has been pre-irradiated with X-rays, γ-rays or ultraviolet light.[32] In one study, the activation energy for pre-irradiated AP was found remain the same at 119 kJ/mol while the induction time decreased: This implies the pre-exponent increased. The increased rate of decomposition of pre-irradiated AP was ascribed to an increase in the nucleation rate constant and an increase in the number of nucleation sites. Note that there had to have been a considerable amount of time between when the AP was irradiated and when the reaction rate experiments were performed. The effect of radiation requires study in the context of the electrical discharge problem, i.e., rapid heating immediately following irradiation by the plasma column, to determine if nucleation sites will develop quickly enough to yield a significant change to the reaction kinetics.

Radiation: An accounting of radiation losses from the plasma is important for two reasons: quantifying radiative heating of energetic constituents and determining the decline in plasma temperature. The importance of the latter was recognized from high speed framing camera photographs that indicate a rapid reduction in plasma temperature. (Arc channel images corresponding to hundreds of nanoseconds after the discharge faded to the point where the film was no longer exposed.) Radiation losses for the plasma are expected to be high, especially in regions adjacent to large AP crystals, owing to the optical transparency of AP in the visible and through much of the ultraviolet spectra.[33] These losses dominate the early stages of energy transfer substantially reducing the temperature of the plasma channel resulting in a hot gas column.

Energy transport within the plasma is important as well, since the spatial redistribution of internal energy as the outer surface radiates will affect radiant losses from the plasma. (It was assumed that the relatively dense plasma was optically thick, i.e., radiated energy within the plasma is absorbed by the plasma, so the radiated energy comes primarily from the arc channel's outer boundary.) Information about the molecular species associated with the plasma and the ionization level of these species is required to determine the energy transport in the plasma. These types of calculation were outside the scope of the present study. In the absence of this information, certain assumptions have to be made concerning the plasma and the hot gas to which the plasma relaxes following cooling. Post-test inspection of the arc channel damage in inert samples suggested that the arc channel is formed in the binder material between the aluminum particles, thus it may be assumed that the plasma is made up of various molecular constituents of the binder material. Since most of the binder is HTPB it can be assumed that the plasma is comprised of vaporized oligomers of HTPB.[34] So, the arc channel region may be modeled as a hot gas with thermal properties matching those of pyrolyzed HTPB.

For large crystals, 250 µm in diameter, the transmitted energy may not assist in promoting reaction on the opposite side of the crystal adjacent to the arc channel, however, pyrolyzed HTPB evolving from the absorption of this energy can promote reaction at the surface of the AP. These issues and similar ones concerning the smaller AP crystals, 20 µm in diameter, require additional study to determine the role of transmitted radiation.

Absorption of radiant energy in the various media surrounding the arc channel is important because this energy serves to preheat and possibly precondition the energetic constituents. A determination of these effects for both the composite layer and large AP crystals is needed to adequately define heating rates and the appropriate decomposition kinetics. For large AP crystals, the amount of radiant energy that may be adsorbed has not been measured. Hills and McBride[33] reported that large single crystals of AP grown in the laboratory absorb radiant energy in the ultraviolet above 200 nm. Based on these data, the absorption of ultraviolet light coming from a 13,000 K blackbody radiator is 18.4% of the total radiant energy. However, they did refer to other work that had reported 300 nm as the absorption edge. They ascribed the disparity in the data to high scattering losses. It is possible that industrial grade AP does not have the same optical clarity of AP that is grown in a laboratory. So the inference that can be made is that the absorption edge for industrial grade AP is 300 nm. This means more wavelengths are absorbed and consequently the

percent energy absorbed increases to 46.3% assuming a 13,000 K blackbody radiation curve. The amount of radiation will decrease as the temperature decreases and, consequently the amount of available energy that is absorbed. This effect is a result of Planck's radiation equation shrinking from the ultraviolet spectrum as lower temperatures are realized. This effect can be seen from Table 5-1 which compares the percent of energy absorbed for the two possible absorption edges (200 and 300 nm) at different temperatures. The values for energy absorption were calculated by integrating Planck's radiation equation at each temperature from zero to the absorption edge value:

$$W_{b,\Delta\lambda} = \int_0^{\lambda_b} \left(\frac{2\pi c^2 h}{\lambda^5} \frac{1}{e^{\frac{ch}{\lambda kT}} - 1} \right) d\lambda \qquad (5\text{-}3)$$

where $W_{b,\Delta\lambda}$ is the amount of radiant energy absorbed, c is the speed of light, h is Planck's constant, λ is the wavelength, λ_b is the wavelength corresponding to the absorption edge, k is Boltzman's constant, and T is the absolute temperature in Kelvin. The total radiant emittance was calculated from the Stefan-Boltzman equation:

$$W_{b,tot} = \sigma_s T^4 \qquad (5\text{-}4)$$

where $W_{b,tot}$ is the total radiant emittance and σ_s is the Stefan-Boltzman constant which has a value of 5.673×10^{-8} watt/m^2-K^4. Note that as the temperature decreases the percent of total radiant energy absorbed decreases. Since the temperature decreases sharply with respect to time, the absorption of radiant energy will only last for a few hundred microseconds.

Table 5-1. Comparison of Radiant Absorption for Different Absorption Edges

Blackbody Temperature (Kelvin)	Total Radiant Emittance (GW/m^2)	Percent Absorbed above 200 nm	Percent Absorbed above 300 nm
13,000	1.62	18.4%	46.3%
10,000	0.567	6.7%	27.3%
8,000	0.233	2.0%	14%
6,000	0.0735	0.02%	3.9%
4,000	0.0145	0.002%	0.2%

Another effect that needs to be investigated is the possibility of increased absorption due to optical degradation of the AP crystal resulting from radiation absorption. White et al[35] observed that a translucent gun propellant turned opaque beneath its surface after exposure to plasma radiation. They attributed this effect to a subsurface reaction induced by the radiant energy absorption. If the AP undergoes a similar decomposition then it is possible that more radiant energy will be absorbed, so it is impossible to say how much of the radiant energy will actually be absorbed by the AP.

Thermal Conduction: The thermal conduction of heat from the plasma column to the various surrounding media occurs on a millisecond time scale, which is much slower than radiation transport. Here the two potential surrounding media of interest are the composite layer and large AP crystals. It is assumed that these two transport problems can be determined separately with a one-dimensional analysis, so the thermal conduction problem can be expressed with two equations which describe the cooling of the gas channel and consequential heating of the surrounding medium. The gas channel is defined as the region between $r = 0$ and $r = a$, where a is the radius of the channel. The surrounding medium is the region beyond the gas channel, i.e., $r > a$. The heat equations in both regions are as follows:

$$\rho_1 C_1 \frac{\partial T_1}{\partial t} = K_1 \frac{\partial^2 T_1}{\partial r^2} + K_1 \frac{1}{r} \frac{\partial T_1}{\partial r} \qquad 0 \leq r < a \qquad (5\text{-}5)$$

$$\rho_2 C_2 \frac{\partial T_2}{\partial t} = K_2 \frac{\partial^2 T_2}{\partial r^2} + K_2 \frac{1}{r} \frac{\partial T_2}{\partial r} + \rho_2 Q z e^{-\frac{E_a}{RT_2}} \qquad r > a \qquad (5\text{-}6)$$

where T_1 and T_2 are the temperatures in the channel and the surrounding medium respectively and r is the radial variable in cylindrical coordinates, ρ_1, c_1, K_1 are the density, specific heat, and thermal conductivity of the hot gas, and ρ_2, c_2, K_2 are the density, specific heat, and thermal conductivity of the solid. Note that the Arrhenius term, introduced earlier, only exists for the surrounding medium, since the gas channel is considered nonreactive.

Summary of Assumptions for the Idealized Model: Based on the discussion in this section a list of assumptions are:

a. Two-dimensional radiation and thermal conduction effects are small so a one-dimensional treatment will be adequate.

b. Different regions (large AP crystals and composite layer matrix) along the length of the plasma column can be considered separately.

c. Radiation losses are important only during the early stages of energy transfer when thermal conduction is minimal, so radiant energy deposition can be simulated separately and used as an initial condition for the thermal conduction simulation.

d. The plasma column has a finite thermal energy at time zero, i.e., the gas has an initial temperature and there are no external heat sources.

e. The arc channel is primarily gaseous plasma

f. The arc channel size once established may be used as an input parameter such that the size remains the same during the simulation.

g.   No AP is trapped in the initial formation of the plasma column and no new material is introduced through ablation during the development of the arc channel, so no significant oxygen is available for the aluminum to react with, hence the plasma column contains no reactive constituents.

h.   The plasma radiates energy like a blackbody from its outer surface.

i.   A radiant deposition profile is established in the solid medium beyond the arc channel at early times on a much shorter time scale than thermal conduction.

This model is presented for future simulation efforts. The next section will treat one aspect of this model.

Simulation of Unimolecular Reaction of Large AP Crystals Using XCHEM

From the three possible mechanisms for reaction, only energy transport from the channel to large AP crystals inducing subsequent unimolecular reaction of the AP was considered. The other problems: (1) energy transport to the composite layer inducing pyrolysis of HTPB and subsequent reaction with AP and (2) reaction of the super-heated hydrocarbon gas making up the plasma with the AP were not considered. Simulations using XCHEM for the onset of reaction in just the large AP crystals is reported here.

XCHEM is a thermal-chemical code which solves the differential equations for thermal transport in and across boundaries between different material regions or layers with chemical kinetics terms specified in each of these layers. The code allows multiple layers of different materials which can have different Arrhenius kinetics parameters. The energy transport problem considers two such layers or concentric cylindrical regions shown in Figure 18: the arc channel was modeled by the first layer and the reactive solid by the second layer. The arc channel layer was modeled as a hot gas with thermal properties matching those of pyrolyzed HTPB. (The specific heat and thermal conductivity for pyrolyzed HTPB were provided by Richard Farmer[36] who is presently modeling pyrolysis of HTPB for a hybrid motor concept.) The values used for the density, thermal conductivity, and specific heat of this gas are given in Table 5-2. The thermal properties used for the AP layer were taken from the literature and are given in Table 5-3. The heat of reaction was calculated from the CET code[37] using the heat of formation (Chemical Propulsion Information Agency, n.d.) as an input; the output of the CET code was processed as described by Baroody and Peters.[38]

For the simulations performed here, the channel radius was 61.8 μm. This radius corresponded to an electrical deposition energy of 850 mJ. This radius was selected because it represented an electrical discharge channel that was photographically studied and the energy deposition was well over that required for ignition.

The code takes into account phase changes, e.g., solid energetic constituents turning into gaseous products, to modify thermal properties in spatial regions where gasification is predicted. (Chemistry resulting from pyrolysis gases is not treated with XCHEM.) The required input is the proportion of carbon, hydrogen, nitrogen, oxygen, and chlorine. No phase changes were considered in the layers representing the arc channel since it was assumed that no reaction occurs in the channel and that channel expansion is primarily through hydrodynamic considerations and not ablation. The proportions for AP (NH_4ClO_4) were used for the reactive solid layer. Note that the AP layer was treated as a semi-infinite medium: this was accomplished by assigning the outer boundary to 600 μm. Since the thermal conductivities for solid AP and HTPB are of the same order of magnitude, it was assumed that the problem could be adequately solved by modeling the entire solid as AP. The thermal conductivity of solid HTPB[28] and AP (Solid Ingredients Propellant Manual and Farmer 1996) are 0.15 and 0.44 W/(m-K) respectively at 450 K.

47
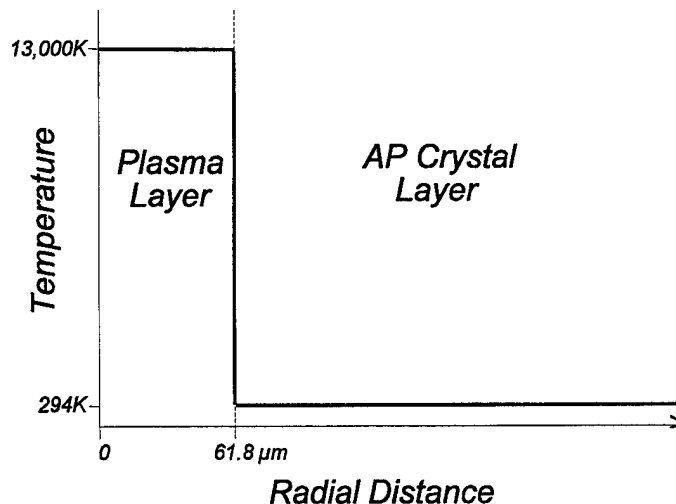
**Figure 18. Initial Conditions for Simulation of
Thermal Transport Ignition Model**

Table 5-2. Material Properties used for the Arc Channel Gas

Definition	Value (SI units)	Value (traditional units)	Comments
Density (ρ)	150 kg/m^3 @61.8 µm radius	0.15 g/cm^3 @61.8 µm radius	See Discussion on density determination
Specific Heat (c_p)	3.18 kJ/kg-K @1000 K	0.76 cal/g-K @1000 K	Reference 39
Thermal Conductivity (K_{low})	0.105 W/m-K @1000 K	2.5 x 10^{-4} cal/cm-s-K @1000 K	Reference 39

Table 5-3. Material Properties used for the Solid (AP)

Parameter	Value (SI units)	Value (traditional units)	Comments
Density ρ	1950 kg/m^3	1.95 g/cm^3	Reference 30
Specific Heat c_p	1.29 kJ/kg-K @288K* 1.55 kJ/kg-K @513K*	0.309 cal/g-K @288K* 0.365 cal/g-K @513K*	Reference 38
Thermal Conductivity K	0.571 W/m-K @ 323K* 0.387 W/m-K @513K*	1.364 x 10^{-3} cal/cm-s-K @323K* 0.924 x 10^{-3} cal/cm-s-K @513K*	Reference 38
Heat of Reaction per Unit Mass Q	1.4 MJ/kg	334 cal/g	See Text Above

* Two values were used to establish a linear dependence on temperature between the two temperatures given. Above the highest temperature the parameter was set to a constant value equivalent to that indicated for the high temperature.

These simulations were the result of two separate computations: (1) an initial radiation computation which served to account for early-time radiation losses and establish a temperature profile in the AP layer, and (2) a subsequent computation which modeled thermal conduction and chemical kinetics. Spatial temperature profiles determined from the initial radiation computation were used as different initial conditions for the second computation. This two step technique was required because XCHEM only simulates radiation as a boundary condition. The initial radiation computation was required to redistribute the radiant energy as a temperature profile in the AP to simulate possible radiant absorption profiles. This was accomplished by artificially elevating the thermal conductivity in the AP layer to 4.19 W/m-K so that the radiant energy would be quickly redistributed through the AP layer from the plasma/AP boundary.

The data for the initial temperature profile was placed in a file that was used as the initial conditions for the second computation where the thermal conductivity of the solid was set at its true value. (This data transfer between the two simulations was made possible by a restart feature incorporated in XCHEM which could re-map the temperature profile from the first computation to the second one.) Note that no reaction was considered in the initial radiation computation, so that as far as the second computation was concerned, the radiant energy deposition profile occurs instantaneously.

The initial radiation computation provided different temperature fields corresponding to different computational times. These temperature fields included the temperature profile for both the plasma and the AP layers. Four examples of these temperatures fields are shown in Figure 19. Profiles 1 and 4 represent temperature fields from the earliest and latest times that were used as initial conditions for the subsequent computations. Different initial temperature profiles were selected to investigate the effect of radiant energy deposition profiles in the AP. The purpose was to determine what type of initial temperature profile is required to support ignition in the AP. (Remember that ignition, in this report, is defined as the establishment of a self-sustaining reaction.) For these simulations, ignition was determined to be the establishment of a rising temperature peak in the AP layer followed by a sustained, propagating thermal front that eventually consumed the AP layer. These data were used to determine if unimolecular reaction of the large AP crystals is a viable ignition mechanism.

Three sets of kinetics parameters were selected from the literature: Oxley et al,[39] Skinner et al,[40] and Price.[41] The values for the kinetics parameters are given in Table 5-4. The parameters from Oxley et al[39] were determined from differential scanning calorimetry (DSC) data. The parameters from Skinner et al[40] were reported as part of a study where Arrhenius kinetics parameters were correlated with ESD sensitivity data. Price[41] used the parameters he reported to model deflagration-to-detonation transition (DDT) studies performed by Atwood et al.[42]

Results from XCHEM Simulations: Kinetics parameters corresponding to low reaction rates like those reported by Oxley et al[39], activation energy of 88.8 kJ/mol and pre-exponent of 3.43 x 10^4, showed no signs of reaction for any initial temperature profile.

The parameters corresponding to a higher reaction rate reported by Skinner et al[40], activation energy of 126.5 kJ/mol and pre-exponent of 2.09 x 10^9, showed the onset of reaction for a number different initial temperature profiles but failed to indicate ignition. Rising temperature peaks were observed in temperature-space-time profiles produced from the data XCHEM yielded. (Figure 20 shows a representative temperature-space profile featuring this temperature peak.) Corresponding consumption of the AP in spatial regions where the thermal peak occurred was also predicted. This was taken to be indicative of the onset of reaction but not ignition because only a portion of the AP layer was consumed. The thermal peak for every case eventually decreased, accompanied by a cessation of AP consumption. This type of result was observed for a range of temperature profiles bounded by Profiles 2 and 3 in Figure 19.
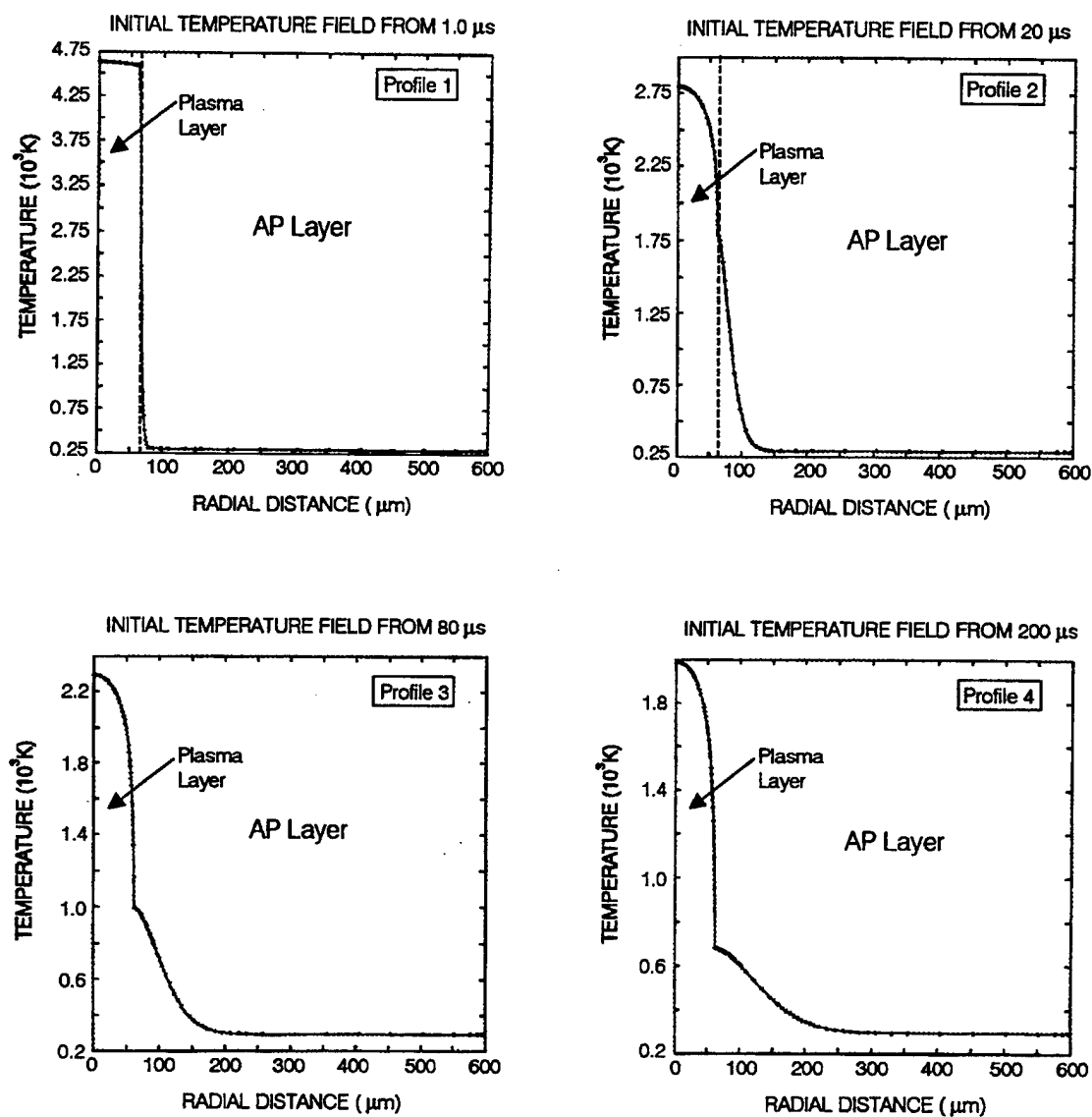
Figure 19. Initial Spatial-Temperature Profiles Generated in XCHEM Simulating Different Radiant Absorption Profiles

Table 5-4. Global Kinetics Parameters Used in XCHEM Simulations

Source	Activation Energy (SI Units) kJ/mol	Activation Energy (Traditional Units) kcal/mol	Pre-exponent s^{-1}
Oxley et al (1990)	88.8	21.2	3.43×10^4
Skinner et al (1996)	126.5	30.2	2.09×10^9
Price (1990)	109	26.0	1.64×10^{10}

TEMPERATURE PROFILE AT TIME 650 μs
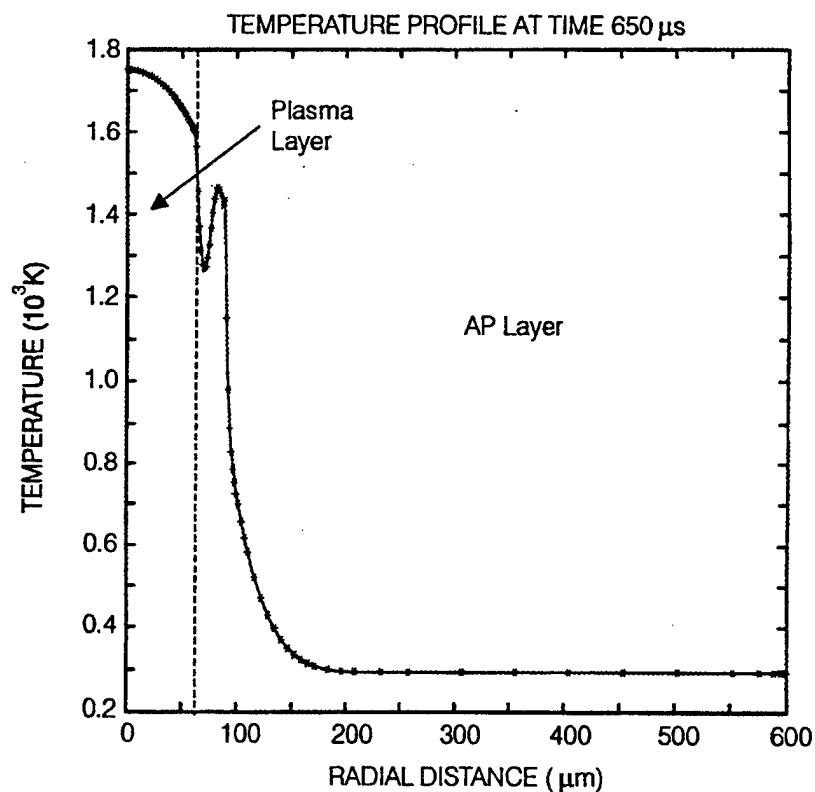
Figure 20. Spatial Temperature Profiles from XCHEM Indicating the Onset of Reaction; Ignition Failed to Occur

The kinetics parameters reported by Price,[41] activation energy of 109 kJ/mol and a pre-exponent of 1.64×10^{10}, which were originally used to model DDT, demonstrated ignition in every situation. Figure 21 shows the results of a simulation where ignition was established in the AP layer. This result corresponds to the initial temperature profile shown in Figure 19 as profile 1 which represents an absorption depth of 16 μm. The time to reaction predicted by the simulation represented in Figure 21 is 1.0 ms, which is less than that observed with the infrared detectors, 5.7 ± 0.2 ms.
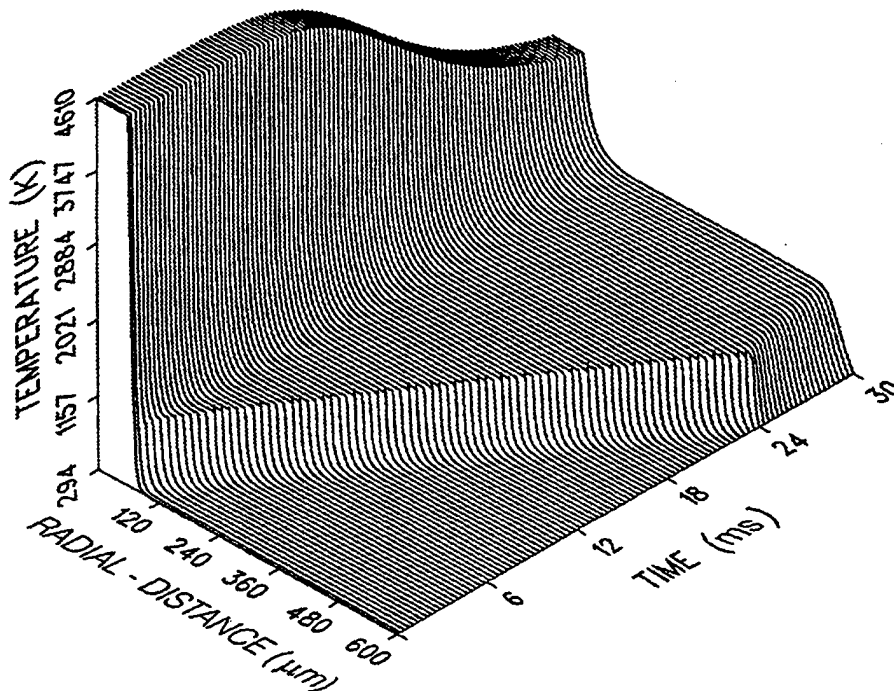
Figure 21. Spatial Temperature Profiles from XCHEM Indicating Ignition

Predicted Absorption Profile Error: The different temperature profiles were run because there were no data on the absorption coefficient for AP in the ultraviolet. Since there are no data on the absorption coefficient, an absorption profile can not be defined at this time. It is expected that the absorption thickness will be small since this was observed by Hills and McBride[33] for two absorption bands in the infrared for AP. They reported that crystal sections could not be cleaved thin enough to allow transmittance of wavelengths in these bands.

It must be kept in mind that the initial temperature profiles generated with XCHEM are artificially high. This is because all the energy that is radiated, using the boundary condition in XCHEM, is absorbed by the AP in the simulations. This is contradictory to the expectation that approximately 46% or less of the total radiant energy should be absorbed by the AP crystal, see Table 5-1. There was no way to extract the amount of energy corresponding to transmitted energy from the energy that was absorbed in the simulations. This is a feature that will have to be added to XCHEM in the future. For now the results indicate the need for an initial temperature profile in the AP layer.

Comparison of Radiant Energy Deposition Time to Time to Reaction: In this section an estimate of the time required to radiate an energy deposition predicted by XCHEM is compared to the lowest experimentally observed time to reaction to provide a perspective of possible radiant energy deposition prior to the onset of reaction. This example is based on the radiant energy deposition predicted by XCHEM for profile 1.

For profile 1, XCHEM predicted the plasma temperature will drop from 13,000 K to 4,650 K. This temperature differential can be used to estimate the energy lost from the plasma with the following:

$$\Delta E = c_p \rho V_{ol}(\Delta T) \tag{5-7}$$

where ΔE is the change in energy, ΔT is the change in temperature, c_p is the specific heat at constant pressure, ρ is the plasma density, and V_{ol} is the volume of the arc channel. (Note that this estimate is a lower bound because the energy stored in the plasma from ionization has not been considered here.) Using the values for specific heat and density from table 5-2 with a channel radius and length of 61.8 µm and 6.35 mm respectively, the energy lost due to the temperature drop is 304 mJ. This is the energy that XCHEM extracts from the channel and redistributes over the absorption depth in Profile 1.

To put the energy deposition predicted above in perspective with radiation from the arc channel, the required time to radiate this amount of energy from the arc channel surface can be compared to the experimentally observed time to reaction. Since there is no easy way to compensate for changes in radiant energy as the temperature decreases, this comparison will have to represent a lower bound for the radiation time in that the calculation will be performed for the initial plasma temperature, 13,000 K, over the area of the arc channel assuming no changes in temperature and channel size. The Stefan-Boltzman equation, given as Equation 5-4, yields 1.62 GW/m^2 as the radiant emittance from the surface of a 13,000 K blackbody. Over the arc channel surface, 2.47 x 10^{-6} m^2, defined by the dimensions given above, the radiant energy per unit time is 4 kW. Dividing the predicted radiant energy deposition from the example above, 304 mJ, by 4 kW yields a radiation time of 76 µs. This value is two orders of magnitude less than the shortest observed time to reaction. The conclusion is that the energy XCHEM extracts from the plasma layer and redistributes over the AP layer as an absorption region are realizable over a relatively short time frame compared to normal thermal conduction and subsequent reaction in the AP. (Remember that the initial radiation computation used a high thermal conductivity in the AP layer to quickly redistribute the radiant energy from the boundary.) What is not known is the actual absorption depth for AP.

Summary of XCHEM Simulations: A one-dimensional simulation of energy transfer from the hot plasma of an arc channel to adjacent AP crystals and subsequent unimolecular reaction of the AP was performed with XCHEM. The simulation showed that an initial temperature profile in the AP was required to establish a notable reaction in the AP. The onset of a notable reaction was indicated by a rising thermal peak in the AP layer.

The initial temperature profiles that were used in these simulations were created from a separate simulation of radiant energy deposition resulting from radiation losses from the plasma. XCHEM could not subtract the amount of radiant energy that would have been transmitted through the AP, so the predicted temperature profiles were high. The results only serve to indicate which parameters might be appropriate for modeling ESD ignition.

From the three sets of global reaction kinetics parameters selected for study, those of Price[41] used to model DDT are the best values for modeling unimolecular reaction of AP from an electrical discharge. These parameters, given in Table 5-4, represent the fastest reaction rate simulated in this study. These parameters provided a prediction of ignition for the thinnest absorption depth studied, 16 µm. These results are encouraging since it is expected that the absorption depth will be very thin as observed by Hills and McBride[33] observed thin absorption depths for two absorption bands in the infrared for AP. Reaction in the composite layer and reaction of super heated hydrocarbon gas in the plasma with adjacent AP crystals are topics for future investigations. Continued efforts in these directions would have been inappropriate without better information concerning the actual radiation losses and the absorption depth of ultraviolet light in both AP and the composite layer. The simulations reported here indicate how the model can work. Future modeling efforts can use this work as a starting point.

Chapter 6

CONCLUSIONS

The results of this study improve the current understanding of millijoule, short duration arc channels in solids and suggest a new way in which to view the ignition process from an electrical discharge. The arc channel is a filamental column of plasma produced when an initial volume of the solid is gasified and ionized under the force of an applied electric field. Post-test observations of arc channel damage in inert samples indicate that the arc channel forms in the binder between aluminum particles producing a narrow column of ionized gas. Since there is not enough energy available to evaporate the aluminum, it may be inferred that the plasma in the channel is only comprised of dissociated binder. The evolving plasma expands under the continued introduction of electrical energy.

This study's main contribution has been to quantify the expansion of the electrical arc channel for an aluminized propellant and indicate a technique for predicting the arc channel size for different electrical energy depositions. The arc channel temperature and time-to-reaction have been quantified as well, and the density of the plasma estimated. Although these data serve to define the heat source that has been produced by the discharge, more information concerning the plasma interaction with the solid energetic constituents is required to accurately simulate thermal transport and ignition.

The evolution of internal arc channels in 6.35 mm thick samples of the ASRM propellant and its inert simulant was quantified by measuring the diameter of arc channel images recorded by a high-speed framing camera. The nominal discharge time for these studies was 400 ns. Nominal electrical energy depositions of 850 mJ and 1150 mJ, corresponding to charging voltages of 24 kV and 28 kV, produced observed radii equivalent to 61.8 ± 21.4 and 76.5 ± 17.4 μm in the propellant. Nominal electrical energy depositions of 600 and 850 mJ, corresponding to charging voltages of 20 and 24 kV, produced observed radii equivalent to 54 ± 15.8 and 59.7 ± 17 μm in the inert. The different operating ranges for the two materials were established between the lowest voltage that would promptly induce dielectric breakdown and the voltage just below that which produced multiple discharges. The variation observed between materials was attributed to the difference in aluminum concentration; 19% for the propellant and 27.2% for the inert.

The photographic studies demonstrated that the arc channel forms with an initial size. Images recorded after the rise time of the current profile, i.e., 24 ns, indicated that the initial channel radii were 29.8 and 35.4 μm for 24 and 28 kV experiments on the propellant, respectively, and 18.7 μm for 24 kV experiments on the inert. The photographic technique could not resolve initial channel sizes for the 20 kV experiments in the inert. Post-test dissections of inert samples indicated that the size of the cavity left by the passing of the arc channel was comparable to the initial size of the dynamic arc channel. From these observations the plasma density in the arc channel was estimated to be 150 ± 66 kg/m^3 by assuming that the mass in the channel corresponded to the amount of binder that existed in the initial volume.

Spectrographic data taken at different times during the discharge show that the temperature is invariant over the portions of the discharge that could be observed. The spectral data were compared to a normalized blackbody curve for a temperature at 13,000 K. The same temperature is determined for a range of different discharge profiles varying in discharge time, energy and energy deposition rate. These data suggest that an equilibrium in the plasma is established early during the course of the discharge: continued energy deposition serves only to expand the channel.

The lowest ignition energy for these experiments was 160 ± 1.4 mJ. (Ignition was defined as establishment of a sustained reaction determined experimentally by total consumption of the sample.) Measurements from pressure transducers placed 3.18 mm from the arc channel showed that no stress waves were generated from reaction occurring in the propellant following the discharge. Infrared detectors measured time-to-reaction following the discharge; the shortest induction time was 5.7 ± 0.2 ms. These results indicate a relatively slow thermally-induced reaction rather than prompt ignition from a shock wave.

In an effort to construct a model to understand the observed ignition results, a number of complex processes associated with energy transport from the arc channel and ignition have been identified. The processes related to energy transport are: absorption of radiant energy, thermal transport within the plasma, pre-conditioning of AP due to irradiation, and optical clarity degradation of AP due to radiation. The three reaction mechanisms are: (1) unimolecular decomposition of adjacent AP, (2) pyrolysis of HTPB binder resulting in an exothermic reaction between the evolving pyrolysis gases and the AP, and (3) reaction of the super-heated hydrocarbon gas making up the plasma with the AP.

Three different sets of Global kinetics parameters from the literature were used in computer simulations. Kinetics parameters corresponding to low reaction rates reported by Oxley et al[39], activation energy of 88.8 kJ/mol and pre-exponent of 3.43×10^4, showed no signs of reaction for any initial temperature profile. The parameters corresponding to a higher reaction rate reported by Skinner et al,[40] activation energy of 126.5 kJ/mol and pre-exponent of 2.09×10^9, showed the onset of reaction for a number of different initial temperature profiles but failed to indicate ignition. The values reported by Price,[41] activation energy of 109 kJ/mol and a pre-exponent of 1.64×10^{10}, which were originally used to model DDT, demonstrated ignition in every situation.

Price's parameters predicted ignition for a very thin temperature profile, 16 µm. These results are encouraging since it is expected that the absorption depth of AP will be small as observed by Hills and McBride[33] for two absorption bands in the infrared for AP.

The last simulation result demonstrated that unimolecular reaction of AP crystals resulting from energy deposition from the arc channel to the crystal is a viable ignition mechanism for the proposed model. This also shows that there may be a link between the chemistry occurring in DDT and ESD ignition.

Future Work

Most of the error associated with the arc channel expansion records were due to the poor resolution of the Imacon framing camera. Improved high speed photographic systems should be used in future studies. Other photographic studies could include observation of the arc channel along its length in a transparent solid that has been seeded with a line of aluminum particles to assist in dielectric breakdown. This can be done effectively by using HTPB binder as the solid. Subsequent experiments could include the AP or KCl since both of these crystals are optically clear. These two experiments would reveal information concerning the discharge in the middle of the sample. This technique would improve temperature measurements as well because there would be a larger radiation surface providing more light for the optics.

Real-time temperature measurements can be made with a two color pyrometer based on photodiodes. The technique measures the signal from two diodes that respond to different wavelength bands. The ratio of the two responses can be calibrated to temperature. These measurements would confirm those made with spectrographic data. If the diodes had a rise time of 10 ns, these measurements could track the temperature evolution of the plasma during the first 50 to 100 ns of the discharge. These data are important for determining plasma temperatures for discharge times under 100 ns.

The two color pyrometer could also track the decline in temperature following the electrical discharge. These data are required for determining the time scale for energy transport from the plasma to the surrounding mediums.

Temperature measurements can be supported with spectrographic data that can resolve the blackbody curve. Broader spectra should be obtained than that obtained in this study. A spectrographic system capable of acquiring broader spectra especially wavelengths in the ultraviolet would provide more detailed data on the radiated spectra from the plasma. Special consideration should be paid to light gathering and intensification of the acquired light so that spectra at times following the discharge can be obtained. This could provide information on the temperature decline during this period.

Radiation transport from the plasma is an important aspect since it serves to cool the plasma and pre-heat a thin region of the adjacent energetic crystal. Radiant losses from the plasma can be inferred from real-time temperature measurements of the arc channel just after the electrical discharge. Quantification of the radiant absorption profile into large AP crystals and the composite layer is required to model the effects associated with radiant heating. This information would allow modeling efforts to investigate different reaction kinetics parameters.

A more accurate determination of the plasma density is required to model heat conduction from the plasma. In this study, it was assumed that the binder material trapped in the arc channel was completely gasified by the end of the electrical discharge, thereby contributing to the mass of the final plasma column. Mass spectroscopy studies would verify which constituents are gasified and made part of the plasma. The plasma mass can be inferred from mass loss measurements, however, this would require an open system to allow the gas to vent, otherwise gas impregnation into the solid will invalidate the results.

Even though unimolecular reaction of the AP was the only ignition mechanism modeled here, two other mechanisms were discussed: pyrolysis of HTPB binder resulting in an exothermic decomposition between the evolving pyrolysis gases and the AP, and reaction of the super-heated hydrocarbon gas making up the plasma with the AP. The post test observation of binder decomposition in inert samples are compelling evidence that reaction in the binder layer plays a role in ESD ignition. Decomposition of binder material on the backside of KCl crystals adjacent to the post-discharge cavity supports the statement that this decomposition occurred as a result of radiant energy deposition. Post test observations also indicate decomposition of binder material from the super heated hydrocarbon gas. Blackened regions were observed on the flat faces of test samples indicate decomposition from hot gasses escaping the channel along the sample/electrode interfaces. The chemistry associated with hydrocarbon pyrolyzation and subsequent reaction with available AP requires investigation.

In regions where the arc channel is completely surrounded by the composite layer, radiant energy will be absorbed in a concentric region defined by the absorption coefficient of the binder/Al/small AP crystal matrix.[43] The effects of ferric oxide (Fe_2O_3) as an optical absorbent and a catalyst for decomposition was reported by Brewster and Hardt.[43] This effect should be investigated experimentally in the context of ESD ignition.

There are a number of other experimental studies that can be done to support modeling efforts. The thermal properties of the plasma, i.e., the specific heat, thermal conductivity and radiation transport, should be quantified. These parameters can be inferred by measuring the temperature profile following the electrical discharge to determine the cooling rate for the plasma. More accurate information could also be obtained by determining the species associated with the plasma so that the thermal properties can be accurately modeled. This type modeling is required to deal with complex changes in energy transport within the plasma as it cools to a hot gas.

Parametric studies isolating the effects of pre-heating from ultraviolet radiation, thermal conduction, and the presence of a hot fuel are required. Parametric studies of unimodal propellant with varying AP size would reveal the importance of large AP versus composite layer heating. The other parameters can be effectively isolated by using thin-walled tubes embedded in test samples. The plasma column can be produced in the tube with the assistance of thin wires with a mass comparable to the masses determined for the arc channel plasma.

Opaque tubes with high thermal conductivity could be used to study the effect of thermal conduction from the plasma while physically isolating it from the AP. Transparent tubes could also be used here to study the effects of radiation heating on samples without thermal conduction contributions

Appendix A

THEORY OF ELECTRICAL ARC EXPANSION

Appendix A

THEORY FOR ELECTRICAL ARC EXPANSION

The deposition of electrical energy controls the evolution of the arc channel. Any energy that the surrounding material initially receives comes from the arc channel (e.g., radiation, shock from the rapidly expanding channel, latent heat transfer from diffusion). It is surmised that there is a material-specific critical thermal mass for the arc channel, above which a reaction in the material beyond the arc channel is possible. It is important to define the arc channel in order to work towards a comprehensive description of ignition from an electrical discharge. This appendix discusses a theory originally developed by Braginskii[44] which describes the arc channel expansion on the basis of hydrodynamic theory. The verification of this theory and quantification of other aspects of the arc channel are dealt with in other areas of this document.

Drabkina[45] originally indicated that the rapid development of an arc channel can be accounted for by the excitation of a shock wave. Even though the two theories are based on similar concepts of hydrodynamics, subsequent experimental efforts[46] have shown Braginskii's theory to be more precise. Even though Braginskii's theory was originally developed for gasses, it is encouraging to note that Martin et al[47] used the theory to good use for determining discharge switch losses in gas and liquid dielectrics.

Braginskii wrote the equations describing the conservation of mass, momentum and energy for his problem as follow:

$$\frac{\partial \rho}{\partial t} + u_p \frac{\partial \rho}{\partial r} + \rho \frac{\partial (r u_p)}{r \partial r} = 0 \tag{A-1}$$

$$\rho(\frac{\partial u_p}{\partial t} + u_p \frac{\partial u_p}{\partial r}) + \frac{\partial (P)}{\partial r} = 0 \tag{A-2}$$

$$\frac{\partial}{\partial t}(\rho \epsilon + \frac{\rho u_p^2}{2}) + \frac{1}{r} \frac{\partial}{\partial r}\{r \rho u_p(\epsilon + \frac{P}{\rho} + \frac{u_p^2}{2})\} + \frac{\partial (rq)}{r \partial r} = JE \tag{A-3}$$

where ρ is the density of the medium, $\mathbf{u_p}$ is the particle velocity, $\mathbf{P}$ is the pressure, ϵ is the internal energy per unit mass $\mathbf{q}$ is the heat flow, $\mathbf{J}$ is the current density, $\mathbf{E}$ is the electric field, and $\mathbf{r}$ is the radial component. He assumed the equation of state for an ideal gas:

$$\epsilon = (\frac{1}{\gamma - 1})\frac{P}{\rho} \tag{A-4}$$

where γ is the ratio of specific heats. He also assumed that the radius of the shock front $a_s(t)$ follows a simple power law:

$$a_s(t) = A t^k \tag{A-5}$$

where **A** and **k** are constants.

Using the above equation of state and following jump conditions which describe the conservation of mass momentum and energy across the discontinuity of a strong shock front:

$$\frac{\rho_o}{\rho} = 1 - \frac{u_p}{U_s} \tag{A-6}$$

$$P = \rho_o U_s u_p \tag{A-7}$$

$$\epsilon = \frac{P}{2}\left(\frac{1}{\rho_o} - \frac{1}{\rho}\right) \tag{A-8}$$

where ρ, u_p, and **P** are the density, particle velocity, and pressure of the medium just behind the front, ρ_o is the initial density of the medium, and U_s is the shock velocity, it is possible to determine the following boundary conditions for the problem in a gaseous medium:

$$\frac{u_p}{U_s} = \frac{2}{\gamma + 1} \tag{A-9}$$

$$\frac{P}{\rho_o U_s^2} = \frac{2}{\gamma + 1} \tag{A-10}$$

$$\frac{\rho_o}{\rho} = \frac{\gamma + 1}{\gamma - 1} \tag{A-11}$$

Braginskii assumed a self similar solution for the problem by introducing the variable $x = r/a_s(t)$ in place of **r** and the following dependent variables:

$$\rho'(x) = \frac{\rho}{\rho_o} \tag{A-12}$$

$$u'(x) = \frac{u_p}{U_s} \tag{A-13}$$

$$P'(x) = \frac{P}{\rho_o U_s^2} \tag{A-14}$$

Note that this transformation of variables is appropriate for any medium. Braginskii treated the outer boundary of the channel as a piston pushing on the surrounding medium in such a way as to establish a shock wave. He assumed that the position of the channel boundary was determined at the point where:

$$u' = x \tag{A-15}$$

or where:

$$\frac{u_p}{U_s} = \frac{a_c}{a_s} \tag{A-16}$$

where a_c is the arc channel radius and a_s is the shock wave radius.

This statement is true only if the particle velocity, u_p, does not vary over the region between the channel boundary and the shock front, i.e., a steady shock wave exists which is being supported by the channel expansion. Solving Equation A-20 for U_s and substituting the expression into Equation A-18 and solving for P yields:

$$P = P' \rho_o (\frac{a_c}{a_s})^2 u_p^2 \tag{A-17}$$

Braginskii also used the assumption of a steady shock wave to state that $P'(a_s/a_c)^2$ is a constant. Hence, Equation A-21 reduces to:

$$P = K_p \rho_o u_p^2 \tag{A-18}$$

where the constant K_p was called the resistance coefficient. Recognizing that the channel velocity is equivalent to the particle velocity in the surrounding medium allows determination of the gas pressure in the channel at the boundary, P_c, with the following expression:

$$P_c = K_p \rho_o (\frac{da}{dt})^2 \tag{A-19}$$

Braginskii used this expression with the differential equations of mass, momentum, and energy conservation to determine that $K_p = 0.9$ and $k = 3/4$. The main importance of Equation A-19 is to eliminate the pressure in the power balance equation for the arc channel.

$$\frac{i^2 R_{ch}}{L_{ch}} = \frac{d\omega}{dt} + P_c \frac{d}{dt}(\pi a_c^2) \tag{A-20}$$

Where i is the current, $R_{ch} = L_{ch}/(\pi\, a_c^2\, \sigma)$ is the resistance of the arc channel, L_{ch} is the length of the arc channel, σ is the conductivity of the plasma in the arc channel, and ω is the internal energy of the plasma per unit length of the arc channel.

Braginskii used Equations A-19 and A-20 to derive an equation of motion for the arc channel expansion. The solution was simplified by assuming that the arc channel is homogeneous in the radial direction so that the following expressions may be used:

$$\omega = M\epsilon, \quad M = \pi a^2 \rho, \quad \epsilon = \frac{P}{\rho}\frac{1}{\gamma - 1} \tag{A-21}$$

where ω and M are the total internal energy and mass of the gas in the channel, ϵ is the internal energy of the gas in the channel, a is the radius of the channel, ρ is the gas density in the channel, P is the pressure, and γ is the effective adiabatic coefficient. Using equations A-20 and A-21, the following is obtained:

$$\frac{d\omega}{dt} = \frac{\pi K_p \rho_o}{\gamma - 1}\frac{d^2}{dt^2}(a^2)a\frac{da}{dt} \tag{A-22}$$

Substituting this expression into Equation A-19 and using the relation $R_{ch}/L_{ch} = 1/(\pi\, a^2\, \sigma)$ yields the following:

$$\frac{i^2}{\pi a^2 \sigma} = \frac{\pi K_p \rho_o}{\gamma - 1}\frac{d^2}{dt^2}(a^2)\frac{da}{dt} + 2\pi K_p \rho_o a^3 \frac{da}{dt} \tag{A-23}$$

Note that the above expression may be rewritten as follows:

$$\frac{i^2}{\sigma} = 2\pi^2 \rho_o \xi (a\frac{da}{dt})^3 \tag{A-24}$$

where

$$\xi = K_p[1 + \frac{1}{\gamma - 1}\frac{1}{2(\frac{da}{dt})^2}\frac{d^2}{dt^2}(a^2)] \tag{A-25}$$

This expression can be further simplified by using the power law solution for the radius, $a = At^2$ which eventually yields:

$$\xi = K_p[1 + \frac{2 - \frac{1}{k}}{\gamma - 1}] \tag{A-26}$$

It is assumed that the value of γ can be obtained by using the Saha formula, where the following is obtained:

$$\frac{I}{(Z + 1)T} = \frac{1}{\gamma - 1} - \frac{3}{2} \qquad \text{(A-27)}$$

where I is the energy of ionization and dissociation for a single heavy particle (atom or ion), T is the plasma temperature in energy units, and Z is the mean charge of an ion.

Andreev and Orlov[48] extended this analysis to predict the radius from an integral expression. They used a model in which the expansion of the arc channel from an initial diameter takes place with a constant electrical conductivity. They wrote Braginskii's differential equation in the following integral form:

$$a = (\frac{4}{\pi^2 \rho_o \xi \sigma})^{\frac{1}{6}} [\int_{t_o}^{t} i^{\frac{2}{3}} dt]^{\frac{1}{2}} \qquad \text{(A-28)}$$

where they assumed that the channel, homogeneous along its length, is completely formed at t_o, after which it begins to expand. They asserted that the radius of this initial channel is determined by the diffusion mechanism associated with streamer expansion. This work indicates that the ultimate size of the arc channel depends on the mechanism of dielectric breakdown which can vary in solid media.

The above analysis requires a determination of σ and γ when the medium in which the discharge occurs is changed. It is possible to use the Saha equation to define the conductivity, σ, and the adiabatic coefficient, γ, analytically. However, a detailed knowledge of the plasma is required. This information is beyond the scope of the present work.

The two goals in this work are to determine if Braginskii's theory can be adapted for solid energetic materials and to use it to predict the final arc channel size for different discharge energies. Since the electric power associated with the arc channel is measured for each experiment, specific knowledge of the plasma conductivity is not required, because the arc channel radius can be expressed in terms of power.

$$\text{Power} \equiv W = i^2 R_{ch} = i^2 (\frac{L_{ch}}{\pi} a^2 \sigma) \qquad \text{(A-29)}$$

In order to obtain an integral expression for the radius in terms of power, Braginskii's differential equation is rewritten as follows:

$$W \frac{\pi a^2}{L_{ch}} = 2\pi^2 \rho_o \xi a^3 (\frac{da}{dt})^3 \qquad \text{(A-30)}$$

Following a similar analysis outlined by Andreev and Orlov,[48] the above expression is re-written as follows:

$$a^{\frac{1}{3}} \frac{da}{dt} = [\frac{W}{2\pi \rho_o \xi L_{ch}}]^{\frac{1}{3}} \qquad \text{(A-31)}$$

Note that:

$$a^{\frac{1}{3}}\frac{da}{dt} = 3/4\frac{da^{\frac{4}{3}}}{dt} \tag{A-32}$$

Substitution yields:

$$\frac{da^{\frac{4}{3}}}{dt} = \frac{4}{3}[\frac{W}{2\pi\rho_o\xi L_{ch}}]^{\frac{1}{3}} \tag{A-33}$$

and integration yields:

$$a = (\frac{4}{3})^{\frac{3}{4}}(\frac{1}{2\pi\rho_o\xi L_{ch}})^{\frac{1}{4}}[\int_0^t W^{\frac{1}{3}} dt]^{\frac{3}{4}} \tag{A-34}$$

or

$$a = K_w[\int_0^t W^{\frac{1}{3}} dt]^{\frac{3}{4}} \tag{A-35}$$

Equation A-35 can be fit to experimental data by determining an appropriate value for K_w. This can be experimentally determined by directly observing the arc channel growth and simultaneously measuring the power deposition. The experimental thrust of this work was to quantify the expansion of the arc channel for different discharge characteristics and to use these data to determine a value for K_w.

Appendix B

ERROR ANALYSIS

Appendix B

ERROR ANALYSIS

GENERAL TREATMENT OF ERRORS

In this study most of the measurements were performed indirectly, e.g., the arc channel diameter was determined from the diameter of a photographic image. The intended errors associated with the actual measurement were related to the final measured value as follows:

$$\varepsilon_f^2 = \sum_i (\frac{\partial f}{\partial x})^2 \varepsilon_{x_i}^2 \tag{B-1}$$

where ϵ_f is the error associated with a measurement defined by $f(x_i)$, ϵ_{xi} represent the various errors associated with the independent measured parameters x. The sums represent different errors associated with each independent parameter. In the example given above, x_1 is the diameter of the photographic image, x_2 is the magnification, M_f, the error associated with determining the diameter of the photographic image is ϵ_x, and the error associated with determining the magnification is ϵ_y. The desired measurement is the diameter of the arc channel, $f(x) = x_1/x_2 = x_1/M_f$ Hence the error, ϵ_f, would be evaluated after differentiation from the following expression:

$$\varepsilon_f = \sqrt{(\frac{\varepsilon_{x1}}{M_f})^2 + (\frac{x\varepsilon_{M_f}}{M_f^2})^2} \tag{B-2}$$

Note that if this is expressed as a fractional error, i.e., the ratio of the error to the measurement, the above expression changes to:

$$\frac{\varepsilon_f}{f} = \sqrt{(\frac{\varepsilon_{x1}}{x})^2 + (\frac{\varepsilon_{M_f}}{M_f})^2} \tag{B-3}$$

Multiplying by 100 would change this to a percent error.

It is possible to have more than one independent error associated with a given measurement. These errors may be combined to produce a total error, ϵ_{tot}, which is equivalent to the sum of the squares of the independent errors and error resulting from experimental variation, i.e., precision of measurement:

$$\varepsilon_{f,tot} = \sqrt{(\frac{\partial f}{\partial x})^2 \varepsilon_{x1}^2 + (\frac{\partial f}{\partial x})^2 \varepsilon_{x2}^2 + (\frac{\partial f}{\partial x})^2 \varepsilon_{x3}^2 + \varepsilon_s^2} \tag{B-4}$$

where ϵ_{x1} through ϵ_{x3} represent three independent errors associated with the measurement of x, and ϵ_s is the standard deviation of the experimental data set. In this report the total error is reported in terms of a standard deviation of the measured value, i.e., the value and error would be reported as $f \pm \epsilon_{tot}$.

ERRORS ASSOCIATED WITH MEASUREMENT OF CHANNEL DIAMETER

A number of measurement errors were associated with the determination of the arc channel diameter. They included errors associated with resolution of the traveling microscope, the determination of the magnification, and the spatial resolution. These errors are combined with the standard deviation of the data set to provide a total error associated with the channel size measurement.

Resolution of Traveling Microscope

The resolution of the traveling microscope used to measure the diameters of the images on each photograph. The resolution of the microscope coupled to a digital read-out was taken to be 0.2 μm. The smallest image diameter measured was 0.2 mm, hence the largest fractional error associated with the microscope resolution was 0.1%.

Magnification Error

Another error is associated with the determination of the magnification. A precision grid pattern was photographed using the system. The spacing between two lines was measured four times on the grid pattern with the traveling microscope and compared to similar measurements of the corresponding lines on the photograph. The average measurements between the two lines on the grid pattern and the photograph were 1579.5 μm and 9360.3 μm respectively. The respective standard deviations were 2.08 and 3.5 μm. The magnification is the ratio of the distance on the photograph to that on the grid pattern, i.e., $M_f = d_{photo}/d_{grid} = 5.926$. The standard error associated with the magnification is determined from the following:

$$\frac{\epsilon_{Mf}}{M_f} = \sqrt{(\frac{\epsilon_{grid}}{d_{grid}})^2 + (\frac{\epsilon_{photo}}{d_{photo}})^2} \tag{B-5}$$

where ϵ_{Mf} is the total magnification error, M_f is the magnification, ϵ_{grid} and ϵ_{photo} are the measurement errors for the grid pattern and the photograph respectively, d_{grid} and d_{photo} are the average values of the distances measured on the grid pattern and the photograph respectively. Note the values for ϵ_{grid} and ϵ_{photo} were taken from the standard deviations of the respective measurements. Supplying the appropriate values in Equation B-5 and multiplying by 100 yields a percent error for magnification, 0.14%. The microscope and magnification errors are at least an order of magnitude smaller than the more significant errors, hence these errors were ignored.

Spatial Resolution

The spatial resolution of the camera objective is a function of camera system resolution, image interpretation error, and varying light levels. Each of these factors is treated below.

Photographic Resolution, ϵ_{rs}

One of the more significant errors was due to the resolution of the photograph which was affected by the resolution of the camera, the film type, and the magnification of the image. Polaroid type 55 film was used to provide positive and negative photographs. The magnification increased the resolution of the system at the objective. This resolution was determined by taking a photograph of a grid pattern which featured different sets of line pairs. The smallest set that could be resolved on the photograph corresponded to 34.5 line pairs/mm at the objective, hence the resolution error, ϵ_{rs}, was 29 μm. Note that the resolution of the film was better than that of the total system.

Interpretation Error, ϵ_{in}

The images of the arc channel were not perfectly circular, therefore, subjective interpretation was required to decide which portion represented the arc channel. The image was typically oblong in shape. The minor axis of these images were taken to be indicative of the channel diameter. These elongated images were assumed to be the result of plasma formed between the channel and the edge of the electrode to complete the electrical circuit. The arc channel was also typically surrounded by a fainter illumination which was assumed to be either the result of plasma leakage from the channel along the interface between the sample and the window or light leakage from the plasma column through the bulk of the test sample. No error is associated with these assumptions because they are accepted as correct decisions, however, the error associated with determining the correct image or the interpretation error was quantified by reading one experimental record four different times. This amounted to reading seven different images four times. The data for this exercise are given in Table B-1. An average of the standard deviations for all seven images was determined and taken as the interpretation error, ϵ_{in}, equivalent to 3.2 μm at the objective. The average of the standard deviations may be used instead of the individual errors for each image because this error is significantly smaller than the total system resolution error.

Table B-1 Diameter of Photographic Images used to Determine Reader Error Associated with Measurement of Channel Size

	Diameter of Photographic Image (μm) at Times During the Discharge							
	24 ns	74 ns	162ns	212ns	262ns	312ns	362ns	412ns
Reading 1	-	436	512	683	691	803	813	864
Reading 2	-	458	610	687	716	839	825	875
Reading 3	-	456	602	701	715	819	850	848
Reading 4	-	461	616	714	732	815	828	874
Average	-	453	585	696	714	819	829	865
Standard Deviation	-	11	49	14	17	15	15	13

Average of the standard deviations = 19 μm

Film Exposure Error, ϵ_{ex}

Concern was also given to varying light levels and the potential to underexpose or overexpose the film which could result in erroneous results. Obvious underexposed and overexposed photographs were rejected for analysis. However, a series of experiments were conducted to quantify the error resulting from variations in film exposure. Experiments were conducted on inert samples with a charging voltage of 24 kV and a discharge time of 400 ns. The aperture of the lens was varied by changing the F-stop to 2.8, 4, and 5.6. The F-stop of 2.8 resulted in an obviously overexposed image towards the end of the discharge. An F-stop of 8 typically resulted in a faint image which was much larger than any of the other images, consequently these types of records were rejected for analysis. Further reduction in aperture size, i.e., higher F-Stops, resulted in no image on the film. The size data for this exercise are given in Table B-2. Data from images corresponding to the same time during each discharge were averaged. An average of the standard deviations for each period in time was taken as the exposure error, ϵ_{ex}, and determined to be 12.2 μm at the objective. The average of the standard deviations may be used here as well for the same reason as before.

Total Error Associated with Spatial Resolution

The expression for calculating the total spatial resolution error includes all for the diameter measurement is as follows:

$$\varepsilon_d = \sqrt{\varepsilon_{rs}^{\;2} + \varepsilon_{in}^{\;2} + \varepsilon_{ex}^{\;2}} \qquad \text{(B-6)}$$

where ϵ_{rs} is the resolution error, ϵ_{in} is the interpretation error, and ϵ_{ex} is the exposure error at the objective. Supplying the values determined above yields:

$$\varepsilon_{d,tot} = \sqrt{(29\,\mu m)^2 + (3.2\,\mu m)^2 + (12.2\,\mu m)^2} \qquad \text{(B-7)}$$

where the spatial resolution is $\epsilon_d = 31.6$ μm at the objective for a measurement of the diameter.

Total Error Associated with Channel Size Measurement

The arc channel expansion data are given in Tables B-3 through B-8. In these tables the values for arc channel radius are reported. For radius values, the above error is reduced by a factor of 2, i.e., the error associated with the radius is $\epsilon_a = 15.8$ μm. The total error associated with the average values for the radius in Table B-8 are determined by combining the standard deviation of the data set, accounting for experimental variation, with the above error:

$$\varepsilon_{a,tot} = \sqrt{\varepsilon_a^{\;2} + s_a^{\;2}} \qquad \text{(B-8)}$$

where $\epsilon_{a,tot}$ is the total error associated with the average value for the radius and s_a is the standard deviation of the data set that produced the average value in tables B-3 through B-7. Remember that the errors for the microscope resolution and magnification of the photographic system are excluded because they were insignificant.

Table B-2 Photographic Images used to Determine Deviation of Measurements from Different Light Exposures.

F stop	Breakdown Delay (ns)	Deposition Energy (mJ)	Diameter of Photographic Images (µm) at Times During the Discharge							
			24 ns	74 ns	162ns	212ns	262ns	312ns	362ns	412ns
2.8	12	849	-	-	235	420	520	620	753	800
4	14	847	-	-	230	329	390	500	560	630
5.6	20	850	-	-	290	350	470	570	700	760
Average			-	-	504.7	367.1	460	563.5	670.6	730.6
Standard Deviation			-	-	67	47	66	60	100	88

Average of the standard deviations = 71.8 µm

Table B-3 Arc Channel Radii for Inert Simulant at 20kV Charging Voltage

F stop	Breakdown Delay (ns)	Deposition Energy (mJ)	Radius of Arc Channel (µm) at Times During the Discharge							
			24 ns	74 ns	162ns	212ns	262ns	312ns	362ns	412ns
4	6	605	-	-	17	28.1	31.5	36.5	42.5	54.4
5.6	16	600	-	-	29.8	36.6	41.6	47.6	51	55.3
5.6	20	597	-	-	21	35.7	45.1	39	47.6	52.7
5.6	8	610	-	19.5	25.5	28.9	35.5	41.7	49.3	53.5
Averages		603 ± 5.7	-	19.5	23.3 ±5.5	32.3 ±4.4	38.7 ±5.9	41.2 ±4.8	47.6 ±3.7	54 ±1.1

			Radius of Arc Channel (μm) at Times During the Discharge							
F stop	Breakdown Delay (ns)	Deposition Energy (mJ)	24 ns	74 ns	162ns	212ns	262ns	312ns	362ns	412ns
4	12	846	-	36	50.7	52	54.4	57.5	63.5	69.7
5.6	14	840	17	34	40.6	46.7	49.6	54.3	55.6	56.1
5.6	6	842	-	-	27.9	33.7	36	44.6	52	59.5
5.6	6	862	-	-	-	34	37	41.6	46.9	54.4
4	14	847	-	-	19.6	28	33.2	42.5	47.6	53.6
5.6	20	850	-	-	24.7	29.8	40	48.5	59.5	64.4
Averages		848 ± 7.8	17	35 ±1.0	32.7 ±12.7	37.4 ±9.7	41.7 ±8.4	48.2 ±6.5	54.2 ±6.6	59.7 ±6.4

Table B-4 Arc Channel Radius for Inert Simulant at 24kV Charging Voltage

Table B-5 Arc Channel Radius for ASRM Propellant at 24kV Charging Voltage

F stop	Breakdown Delay (ns)	Deposition Energy (mJ)	Radius of Arc Channel (μm) at Times During the Discharge							
			24 ns	74 ns	162ns	212ns	262ns	312ns	362ns	412ns
5.6	12	841	-	-	27.3	47	45.9	50.8	51.3	57
4	18	831	-	34.4	42.5	46.8	51	55.3	55.3	57.8
5.6	16	870	25.5	36	55	61.5	69.6	68	70	82.5
5.6	16	885	-	22.4	33.7	41.6	41	46.2	46.9	50
Averages		857±25	25.5	30.9 ±7.4	39.6 ±12	50 ±10	52 ±12.3	55.1 ±9.4	55.9 ±10	61.8 ±14.2

Table B-6 Arc Channel Radius for ASRM Propellant at 28kV Charging Voltage

F stop	Breakdown Delay (ns)	Deposition Energy (mJ)	Radius of Arc Channel (μm) at Times During the Discharge							
			24 ns	74 ns	162ns	212ns	262ns	312ns	362ns	412ns
4	12	1151	-	40	51	56.1	57	62.9	65.5	71.4
4	12	1153	-	39.1	55.6	67.2	71.4	79.1	76.5	81.6
Averages		1152	-	35.6 ±0.7	53.3 ±3.3	61.7 ±7.9	64 ±10.2	71 ±11.5	71 ±7.6	76.5 ±7.2

Table B-7 Radius of Arc Channel at 24 ns from Arrival of Discharge Pulse for ASRM Propellant and its Inert Simulant

Initial Radius in Propellant (μm)		Initial Radius in Inert (μm)	
24 kV	28 kV	20 kV	24 kV
34, 25.5	39.1, 37.4, 29.8	none observed	17, 17, 17, 25.5

Table B-8 Arc Channel Expansion Data for ASRM Propellant and Its Inert Simulant Using a 400 ns Discharge

Material	Charging Voltage	Average Final Radius* (μm)	Final Radius Error (μm)	Average Radius* @24ns (μm)	Radius Error @24ns (μm)	Slope of Fit* (x10^6)	Average Slope for I$_w$*	K$_w$** (x10^3)
Propellant	24 kV	61.8 ±14.4	21.4	29.8 ±4.3	16.4	75.3 ±13	1291 ±12.2	58.3 ±10.1
Propellant	28 kV	76.5 ±7.2	17.4	35.4 ±5.0	16.6	86.2 ±10.2	1362 ±8.5	63.6 ±7.5
Inert	20 kV	54 ±1.1	15.8	-	-	115.4 ±8.0	1183 ±9.0	97.5 ±6.8
Inert	24 kV	59.7 ±6.4	17	18.7 ±3.8	16.3	110 ±3.6	1267 ±14.1	86.8 ±3.0

* The standard deviation follows the mean of each value so designated with the ± sign in front of it.
** The average deviation determined from the total error follows each value so designated with a ± sign in front of it.

ERROR ASSOCIATED WITH THE CURRENT MEASUREMENT

The current probe consisted of a Pearson field coil. The precision of the instrument has been established at 1% by the manufacturer. For reference the fractional error associated with the precision can be represented as follows, $\epsilon_{pi}/I(t) = 0.01$.

Other potential errors in the current measurement are the evaluation of the resistance placed on the output of the current probe, R_{out}, to attenuate the signal sent to the oscilloscope, and an additional current which arises from fast-changing voltages through a parasitic capacitance, c_{Ld}, in parallel with the electrode gap. The resistance, R_{out}, was determined to be 9.203 Ω with an associated error, ϵ_{Ri}, of 3 mΩ. Hence, the fractional error was approximately $\epsilon_{Ri}/R_{out} = 0.0003$. The capacitance, c_{Ld} was measured with a impedance bridge and found to be 14 pF. Short lived spikes associated with the sudden arrival of the voltage wave from the LX-40 were observed with the Tektronix analog scope but not on the digital scopes typically used for data acquisition since they were limited in band width and sampling rate. Since this potential error was not recorded on the digital oscilloscope, it is not treated here. The relatively slower voltage change associated with the voltage ramping down did not exceed 2 GV/s which corresponds to an error, ϵ_{ci}, of 28 mA in comparison to currents in the 100 A range. Hence, the fractional error associated with parasitic capacitance is approximated to be $\epsilon_{ci}/I(t) = 0.0003$, where the magnitude for the current is taken to be on the order of 100 A. The fractional error associated with the current measurement may be defined as follows:

$$\frac{\varepsilon_I}{I} = \sqrt{(\frac{\varepsilon_{pi}}{I})^2 + (\frac{\varepsilon_{Ri}}{R_{out}})^2 + (\frac{\varepsilon_{ci}}{I})^2} \tag{B-9}$$

where the percent error is determined to be 1% indicating that the errors associated with parasitic capacitance and resistive load determination are negligible.

ERROR ASSOCIATED WITH THE VOLTAGE MEASUREMENT

The voltage probe consisted of a Pearson field coil measuring the current through a liquid resistor. The value of the liquid resistor was measured prior to each experiment with an impedance bridge (Hewellet Packard Model 4277A). The nominal value of this resistance was 1000 Ω. The error associated with the measurement of this resistance, ϵ_{rv}, was 5 Ω, hence, the fractional error associated with this gauge factor was $\epsilon_{rv}/V(t) = 0.003$.

There were two sources of error for voltage measurements associated with inductance; the self-inductance of the load, L_{Ld}, and the self-inductance of the voltage probe, L_V. The inductance L_s did not contribute to the error because it was outside the connection between the load and the voltage probe. The errors occur as voltage drops, V_L, across the inductance, L, for large changes in current, $V_L = L(dI/dt)$. The inductance L_{Ld} was estimated at 13 nH by measuring the inductance associated with a 20 mil (0.5 mm) diameter wire inserted through an inert sample placed between the electrodes. The initial rate of rise, dI/dt, for the current was observed with a 1 GHz bandwidth analog scope (Tektronix 7104) to be nominally 100 GA/s over a period of 2 ns. This would generate a voltage drop across the arc channel inductance 1.3 kV in magnitude. The digital scope did not record this spike for reasons indicated above. So the error that would have been induced by this spike is not treated here. Following the initial current rise, the current would ramp up at a rate that did not exceed 2 GA/s. This induced a voltage drop, ϵ_{Ld}, approximately 26 Volts, in comparison to typical voltages which exceeded 10 kV. The fractional error associated with the gap inductance was $\epsilon_{Ld}/V(t) = 0.003$. The self-inductance associated with L_V was higher, 110 nF, but the current through

the liquid resistor was orders of magnitude lower, and the corresponding rate of rise was 2.5 MA/s. This induces a voltage error, ϵ_{Lv}, equivalent to 0.3 volts, So, the fractional error associated with the voltage probe inductance was $\epsilon_{Lv}/V(t) = 3 \times 10^{-7}$.

Since the voltage measurement was basically a measurement of current through a resistance, parasitic capacitance effects must be considered as well. Similar to the error in the current measurement this error comes from fast-changing voltages through a parasitic capacitance, c_v. The capacitance associated with the voltage probe was measured with impedance bridge and found to be 3 pF. The largest rate of voltage change over the course of the discharge was 2 GV/s, hence, the associated error, ϵ_{cv} was 6 mA. The fractional error associated with the parasitic capacitance in the voltage probe was $\epsilon_{cv}/I_v = 0.0006$, where I_v is the measured current in the voltage probe taken here to be 10 A. The fractional error associated with the voltage measurement may be expressed as follows:

$$\frac{\varepsilon_v}{V} = \sqrt{(\frac{\varepsilon_{pi}}{I})^2 + (\frac{\varepsilon_{Rv}}{R_v})^2 + (\frac{\varepsilon_{Ld}}{V})^2 + (\frac{\varepsilon_{Lv}}{V})^2 + (\frac{\varepsilon_{cv}}{I_v})^2} \qquad \text{(B-10)}$$

where ϵ_{pi} is the precision of the Pearson probe. Supplying the values above and determining the percent error yields 1.09% indicating that the errors outside of the precision of the Pearson probe are minimal.

ERROR ASSOCIATED WITH THE POWER MEASUREMENT, W(t)

The error associated with the determination of power, ϵ_w, is determined by combining the errors for current and voltage as follows:

$$\frac{\varepsilon_w}{W} = \sqrt{(\frac{\varepsilon_I}{I})^2 + (\frac{\varepsilon_v}{V})^2} \qquad \text{(B-11)}$$

Supplying the values from above yields a percent error of 1.48%.

ERROR ASSOCIATED WITH CALIBRATION OF ANALYTICAL EXPRESSION

The value for K_w is the calibration of the analytical expression to the materials studied. This coefficient was determined to provide a close fit between the averaged data for arc channel radius and the analytical expression derived in Chapter 3:

$$a(t) = K_w [\int_0^t W^{\frac{1}{3}} dt]^{\frac{3}{4}} \qquad \text{(B-12)}$$

where a(t) is the arc channel radius and W(t) is the electrical power. The analytical expression for the arc channel expansion may be expressed as $a(t) = k_w * I_w(t)$, where $I_w(t)$ is the value of the integral expression at time t:

$$I_w(t) = [\int_0^t W^{\frac{1}{3}} dt]^{\frac{3}{4}} \qquad \text{(B-13)}$$

Since the determination of K_w requires a comparison of the curve I_w and the data, the error associated with K_w requires knowledge of the error associated with I_w.

The curve I_w is exclusively dependent on the electric power deposition, $W(t)$, which is determined from the product of the current measurement $I(t)$ and the voltage measurement, $V(t)$. The individual analyses below detail the errors for current and voltage first, then combine these errors to provide an error associated with the power profile which is then used to determine the error associated with I_w.

Error Associated with the Integral Expression I_w

The error associated with $I_w(t)$ may be estimated by first reducing the power, $W(t)$, to a constant over the integration, W_0. This simplifies the analysis and is allowable because the power profile may be modeled as a rectangular pulse. So the integral expression for power reduces to:

$$I_w = [W_o^{\frac{1}{3}} t]^{\frac{3}{4}} \tag{B-14}$$

differentiation with respect to W_0 yields:

$$\frac{dI_w}{dW_o} = \frac{1}{4} W_o^{\frac{-3}{4}} t^{\frac{3}{4}} \tag{B-15}$$

and the proportional error may be expressed as follows:

$$\frac{\varepsilon_{Iw}}{I_w} = |\frac{\varepsilon_w}{I_w}(\frac{dI_w}{dW_o})| = |\frac{1}{4}\frac{\varepsilon_w}{W_o}| \tag{B-16}$$

Since the error associated with the power is $\varepsilon_w = (0.0148)W(t)$, the fractional error associated with I_w is one fourth that for the power, i.e., $\varepsilon_{Iw}/I_w = 0.0035$. Hence the percent error is 0.35%.

Error Associated with Calibration of the Coefficient K_w

The average curve for I_w was compared to a linear least squares fit of the last 6 data points. These data existed between 162 and 412 ns after the initial arrival of the discharge pulse. The last six data points were selected for the fit for three reasons: they were represented in every experiment, they existed on a fairly linear portion of the $I_w(t)$ curve, and the time difference among the data were uniform. An average curve for $I_w(t)$ was produced by taking an average of the curves for a given experimental situation, e.g., designated by changes in the material and the charging voltage. Values for K_w were made to match the slope for $K_w*I_w(t)$ to that of a linear least squares fit. The initial value of the arc channel was selected by shifting the curve of $K_w*I_w(t)$ up by a constant value until the two curves overlaid one another. The errors associated with determining K_w are determined by combining the standard deviations of the slope for the least squares fit and the average for I_w and the error above for I_w:

$$\frac{\varepsilon_{kw}}{K_w} = \sqrt{(\frac{\varepsilon_{ft}}{S_{ft}})^2 + (\frac{\varepsilon_{Iw}}{S_{Iw}})^2 + (\frac{\varepsilon_{Iw}}{I_w})^2} \tag{B-17}$$

where ϵ_{kw} is the error associated with K_w, ϵ_{ft} and ϵ_{Iw} are the errors associated with the slopes for the least squares fit and I_w respectively, S_{ft} and S_{Iw} are the respective slopes, and ϵ_{Iw} is the error determined above for I_w.

The slope for I_w was determined by averaging the slopes of the individual I_w for a given scenario. The slope and the standard deviation for the least squares fit came out of the analysis for the fit which was determined by a data manipulation program called VuPoint II.

The data for the propellant and the inert simulant experiments used for these calculations are given in Tables B-3 through B-8. Tables B-3 through B-6 give the values for the radius at the distinct times defined by the camera operation. The data were selected from experiments using F-Stop settings of 4 and 5.6. Table B-7 supplies the data for the initial radius obtained in separate experiments which typically required the use of an F-Stop setting of 2.8. The average values for initial and final channel radii are given with their standard deviations and total errors in Table B-8. The above slopes, standard deviations for the slopes, and the values for K_w and its error are also given in Table B-8.

ERROR ASSOCIATED WITH PREDICTED ARC CHANNEL RADIUS

The fractional error associated with predicted arc channel radius, a_p, is determined by combining the errors for I_w and K_w given above:

$$\frac{\epsilon_{ap}}{a_p} = \sqrt{(\frac{\epsilon_{Iw}}{I_w})^2 + (\frac{\epsilon_{Kw}}{K_w})^2} \qquad \text{(B-18)}$$

where ϵ_{ap} is the error associated with the predicted radius, a_p.

ERROR ASSOCIATED WITH PLASMA DENSITY ESTIMATE

The arc channel plasma density was estimated by assuming the mass of the final arc channel corresponds with that of the binder involved in the initial channel size. It was shown in Chapter 4 that the aluminum in the channel does not evaporate. So the mass and volume of the aluminum must be excluded from the calculation. The mass of the plasma may be determined as follows:

$$m_{plasma} = \rho_B k_{\%B} V_i \qquad \text{(B-19)}$$

where m_{plasma} is the mass of the plasma, ρ_B is the density of the binder, $k_{\%B}$ is the fractional coefficient of the volume percentage of binder in the binder/aluminum matrix, and V_i is the initial volume of the arc channel.

The final density at the end of the discharge may be expressed as follows:

$$\rho_f = \frac{m_{plasma}}{V_f - V_{Al}} = \frac{m_{plasma}}{V_f - k_{\%Al} V_i} \qquad \text{(B-20)}$$

where ρ_f and V_f are the final density and final volume of the plasma respectively, V_{Al} is the volume of aluminum in the channel, $k_{\%Al}$ is the fractional coefficient corresponding to the volume percentage of aluminum in the channel.

Combining Equations B-19 and B-20 yields:

$$\rho_f = \frac{\rho_B k_{\%B} V_i}{V_f - k_{\%Al} V_i} \tag{B-21}$$

This expression may be rewritten as follows:

$$\rho_f = \frac{\rho_B k_{\%B}}{\dfrac{a_f^2}{a_i^2} - k_{\%Al}} \tag{B-22}$$

where a_i and a_f are the respective initial and final radii of the plasma column. Note that the channel length is assumed to be the same at the beginning and end of the discharge.

The various percentages by mass and volume for both materials and their respective binder/aluminum matrix regions are given in Tables 4-3 and 4-4. The volume percentages for the binder and the aluminum were determined from the density and weight percentages for each material. No error was given with the specified values of weight percentage, so no error can be assigned to the volume percentages of constituents in the binder/aluminum matrix. The errors for the initial and final radii are due to the same reason making these non-independent errors associated with estimating the plasma density at the end of the discharge. Hence, the equation for the error is determined from the following:

$$\varepsilon_{pf} = \frac{\partial \rho_f}{\partial a_i} \varepsilon_{ai} + \frac{\partial \rho_f}{\partial a_f} \varepsilon_{af} \tag{B-23}$$

where ϵ_{pf}, ϵ_{ai}, and ϵ_{af} are the errors associated with the plasma density, the initial channel radius, and the final channel radius measurements respectively. The fractional error is as follows:

$$\frac{\varepsilon_{pf}}{\rho_f} = \frac{2\dfrac{a_f^2}{a_i}}{a_f^2 - k_{\%Al} a_i^2} \varepsilon_{ai} - \frac{2a_f}{a_f^2 - k_{\%Al} a_i^2} \varepsilon_{af} \tag{B-24}$$

For example, using the information for the 24 kV experiments for the propellant, the fractional error for the density is 0.44. For this case, the density was determined to be 150 kg/m^3, so the error is $\pm$ 66 kg/m^3.

Appendix C

THEORY FOR EXOTHERMIC REACTION MODELING

Appendix C

THEORY FOR EXOTHERMIC REACTION MODELING

The mathematical theory of exothermic reaction, as discussed by Frank-Kamenetskii,[49] combines the equation of heat transfer and diffusion with an equation which describes the chemical kinetics.

$$c_p \rho \frac{\partial T}{\partial t} = \nabla \cdot (K \nabla T - c_p \rho v T) + \frac{\partial q_c}{\partial t} \qquad \text{(C-1)}$$

where it is typically assumed that the rate of reaction depends more strongly on temperature than any other parameter. Here T is the temperature, ρ is the density of the material, c_p is the heat capacity for constant pressure, K is the thermal conductivity, v is the velocity of the reaction front, and q_c is the heat per unit volume acquired or lost by the material due to chemical decomposition. A heat loss term in dq_c/dt would account for an endothermic phase of the chemical decomposition.

For cases where the medium is stationary and the concept of a moving reaction front is not considered, the velocity term is neglected, i.e., $v = 0$. Furthermore, assuming a constant thermal conductivity, the above equation reduces to:

$$c_p \rho \frac{\partial T}{\partial t} = \lambda \nabla^2 T + \frac{dq_c}{dt} \qquad \text{(C-2)}$$

The manner in which the chemical heating rate term, dq_c/dt, is introduced to the equation depends on the model of reaction. The simplest reaction model describes a unimolecular decomposition.

$$A \rightarrow B + C + Q \qquad \text{(C-3)}$$

The molecule A decomposes thermally into B and other different molecules C, where Q is the heat of reaction per unit mass. The reaction rate usually takes the Arrhenius form which yields the following rate equation:

$$\frac{dN_A}{dt} = -z N_A e^{-\frac{E_a}{RT}} \qquad \text{(C-4)}$$

where N_A is the mass fraction of undecomposed reactant at any point, z is the decomposition rate factor in units of sec^{-1}, E_a is the activation energy in units of J/mol, and R is the gas constant which is equivalent to 8.314 J/(mol-K). The rate at which exothermic energy is released is given by:

$$\frac{dq_c}{dt} = -Q \frac{dN_A}{dt} = Q z N_A e^{-\frac{E_a}{RT}} \qquad \text{(C-5)}$$

C-3

The chemical heating rate can be comprised of more than one term depending on the complexity of the chemistry. An example which illustrates this is the following autocatalytic scheme:

$$A \rightarrow B + C + Q_1$$
$$B + A \rightarrow B + B + C + Q_2 \tag{C-6}$$

where molecules **A** decompose into molecules **B** and other molecules **C**. Then the **B** molecules act as a catalyst for further decomposition of **A** with a different reaction rate and heat of reaction. The corresponding rate equation is:

$$\frac{dN_A}{dt} = -z_1 N_A e^{-\frac{E_1}{RT}} - z_2 N_A N_B e^{-\frac{E_2}{RT}} \tag{C-7}$$

where the subscripts on the various reaction rate parameters correspond to the respective decomposition processes. The rate at which exothermic energy is released is given by:

$$\frac{dq_c}{dt} = Q_1 z_1 N_A e^{-\frac{E_1}{RT}} + Q_2 z_2 N_A N_B e^{-\frac{E_2}{RT}} \tag{C-8}$$

THE CONCEPT OF THE INDUCTION TIME

The exothermic decomposition of the energetic material tends to heat the material which in turn speeds-up the reaction. Opposing this tendency is the flow and loss of heat to cooler surroundings. If the loss of heat dominates, then the ensuing reaction gradually slows as the decomposing material becomes used up. If the chemical reaction dominates, the result is a rapid increase in the temperature. This rapid rise in temperature typically follows a period of self-heating or induction time. This time to exotherm is dependent on the energetic material, the geometry of the sample, and the temperature of the material. During this induction time very little of the reactive material is decomposed. A sudden increase in decomposition yields a steep temperature rise when the induction period is completed.

STEADY STATE CONDITION AND THE CONCEPT OF CRITICAL TEMPERATURE

Frank-Kamenetskii[49] examined the steady state problem, i.e., $dT/dt = 0$, for external heating of a sample. His analysis provides the critical temperature for three symmetric geometries. The critical temperature, T_{cr}, is defined as a limiting value of the temperature of the material which, if exceeded, leads to runaway exothermic reactions (thermal explosion).dimensional symmetry was used so that the conduction process would only depend on a single spacial coor One dinate, i.e.,

$$\nabla^2 = \frac{\partial^2}{\partial \zeta^2} + \frac{n}{\zeta} \frac{\partial}{\partial \zeta}, \tag{C-9}$$

where n = 0, 1, or 2 for planar, cylindrical, or spherical symmetry and ζ refers to the appropriate single spacial coordinate. The critical surface temperature, T_{cr}, for thermal explosion was found to fit the following transcendental expression:

$$T_{cr} = \frac{E_a/R}{\ln(\dfrac{QE_a a^2 \rho z}{\lambda R T_{cr}^2 \delta_{cr}})} \qquad \text{(C-10)}$$

where **a** is the significant dimension of the sample, e.g., the radius or the half thickness, and δ_{cr} is the critical value of a dimensionless parameter equivalent to 3.32 for spheres, 2.0 for cylinders, and 0.88 for slabs. This result provides the ability to determine the threshold temperature for thermal explosion under the steady state condition.

THE STUDY OF THERMAL EXPLOSION

Various experimental techniques have been devised to study thermal explosion. These techniques have used heat baths or some other controlled means to elevate the reactive sample to a given temperature. Robertson[50,51,52] and Rogers[53,54] conducted calorimetry experiments on various energetic materials to determine the kinetic parameters. Plots of $\ln(k)$ vs $1/T_1$, where **k** is the reaction rate and T_1 is the temperature of the bath, were used to determine E_a and **z**. Other investigators have measured the induction time, t_{ind}, or time to exotherm for various temperatures. The data were presented as plots of $\ln(t_{ind})$ vs $1/T_1$. A number of authors, like Henkin and McGill,[55] Wenograd,[56] and Lee et al,[57] have taken the slope of this curve as the apparent activation energy. However, Lisitskii and Merzhanov,[58] and Zinn and Rogers[59] have indicated that the plots of $\ln(t_{ind})$ vs $1/T_1$ do not reflect the true relationship between t_{ind} and the kinetic parameters of the ignition process. They point out that the apparent activation energy calculated from induction time experiments does not necessarily reflect an isolated chemical process. At best it represents a mixture of chemical and thermophysical processes.

In addition, studies by McGuire and Tarver[30] under conditions of full containment and Brill and Brush[60] under conditions of higher temperatures, have indicated that a single Arrhenius term is not sufficient for accurate modeling. These conditions are of interest to the present work because containment of the arc channel has proven to be a critical element in reducing the electrical energy required for ignition.

EFFECT OF CONTAINMENT ON KINETIC PARAMETERS

McGuire and Tarver[61] have conducted experiments with an apparatus which maintains full containment of the material in one-dimensional geometries up to operating pressures of 150 MPa. The apparatus eventually became known as the One Dimensional Time to Explosion (ODTX) test. They reported linear Arrhenius plots of $\ln(t_{ind})$ vs $1/T_1$ for a number of energetic compounds. These data contradict earlier mathematical treatments by Zinn and Rogers,[59] and Zinn and Mader[62] based on a single Arrhenius term which predict significant curvature in Arrhenius plots. The ODTX apparatus measured critical temperatures less than those predicted using kinetic parameters proposed by Rogers[63] in the Frank-Kamenetskii model discussed above. The difference was attributed to the experimental apparatus; the ODTX apparatus used by Tarver et al[64] did not allow the gaseous decomposition products to escape from contact with the remaining solid energetic material. This work indicates that the kinetics of reaction can be enhanced for some materials if the gaseous decomposition products are kept in good thermal contact with themselves and the solid energetic. This suggests that materials displaying a sensitivity to containment generate product gases that are exothermically reactive with themselves and/or with the condensed energetic. Tarver et al[64] demonstrated that a realistic thermal conductivity model coupled with multiple Arrhenius terms to satisfy the various reaction kinetics taking place were required to reach agreement between computational and experimental results.

EFFECTS OF HIGH TEMPERATURE ON KINETIC PARAMETERS

Brill and Brush,[60] experimentally extended the ODTX studies of Tarver et al [64]to higher temperatures for several materials. The lowest temperature studied by Brill and Brush was the highest temperature used in the ODTX experiments. Their apparatus allowed them to simultaneously measure induction times with thermocouples and the gas products evolved from the sample by Fourier transform infrared (FTIR) spectroscopy. The curves of $\ln(t_{ind})$ vs $1/T_1$ were linear except for an abrupt change in the slope which occurred at different temperatures for different materials. Hence, they reported two different activation energies for each material studied. The highest value was always associated with the lowest temperature range. They reported activation energies for ammonium perchlorate to be 199 kJ/mol between 741 and 764 K and 62 kJ/mol between 765 and 827 K. They suggested that at lower temperatures, the activation energy for chemical reactions dominate over heat flow effects, while at higher temperatures, heat flow effects dominate.

Schrader et al[65] have used a different technique, called the Thermal Step Test (TST), to obtain induction time measurements at even higher temperatures. Samples were heated instantaneously to various temperatures up to 1400 K. The TST is a refinement of a technique originally developed by Wenograd.[56] The energetic material is confined in a stainless steel capillary tube. The tube is heated to the desired temperature within 30 μs by passing current through the tube from a capacitive discharge circuit (22 μf). The induction time is defined as the time between the heating pulse and the moment the tube is ruptured. They observe linear plots of $\ln(t_{ind})$ vs $1/T_1$ at relatively low temperatures, which are in agreement with those reported by McGuire and Tarver.[30] At higher temperatures the induction times eventually level off, i.e., longer times were measured in comparison to extrapolated values from the low temperature region. The induction times for secondary explosives did not decrease below the millisecond domain. Some secondaries, e.g., RDX, PETN, and tetryl, displayed a negative temperature coefficient, i.e., the induction time was observed to increase over a range of higher temperatures. Schrader et al[65] suggested that the decreasing trend was due to a slower step in the decomposition process which becomes dominant at higher temperatures. The trend in the TST data follows that reported by Brill and Brush.[60] However, some of the plots given by Schrader et al[65] demonstrate significant curvature of the Arrhenius plots at high temperatures.

REFERENCES

1. Knaur J. A. "Technical Investigation of 11 January 1985 Pershing II Motor Fire," Minutes of the Twenty-Second Explosives Safety Seminar, Vol. 1, Anaheim, CA, 26-28 August, 1005-1013, Department of Defense Explosives Safety Board, 1986.

2. Hodges, R. V. and McCoy, L. E., "Energy Threshold for Electrostatic Discharge Ignition of Propellant," 1989 JANNAF Propulsion Systems Hazards Subcommittee Meeting, San Antonio, TX, 21-24 February, 375. Chemical Propulsion Information Agency Publication 509, Vol 1.

3. Hodges, R. V. and McCoy, L. E. "Threshold Ignition Energy for an Electrical Discharge in Propellant," 1990 JANNAF Propulsion Systems Hazards Subcommittee Meeting, Laurel, MD, 3-5 April, 381, Chemical Propulsion Information Agency. Publication 538, Vol 1.

4. Hodges, R. V. and McCoy, L. E. "Ignition of Solid Propellant by Internal Electrical Discharge," 1991 JANNAF Propulsion Systems Hazards Subcommittee Meeting, Albuquerque, NM, Mar 18-22, 79, Chemical Propulsion Information Agency Publication 562.

5. Hodges, R. V. and McCoy, L. E., "A Fixture to Test ESD Sensitivity of Propellant Under Confinement," 1993 JANNAF Propulsion Systems Hazards Subcommittee Meeting, Fort Lewis, WA, 11-13 May, 531, Chemical Propulsion Information Agency Publication 599.

6. Lee, R. J. and Tasker, D. G. "Electrostatic Initiation Within Cased, Energetic Materials," 1991 JANNAF Propulsion Systems Hazards Subcommittee Meeting, Albuquerque, NM, 18-22 March, 95, Chemical Propulsion Information Agency Publication 562.

7. Covino, J., Graham, K. J., Boyer, L., and Kraeutle, K. J., "Electrostatic Discharge (ESD) Sensitivity of Solid Rocket Propellants at the Naval Weapons Center," 1986 JANNAF Propulsion Systems Hazards Subcommittee Meeting, Monterey, CA, 3-7 March, 311-322, Chemical Propulsion Information Agency Publication 446, Vol. 1.

8. Covino, J. and Hudson, F. E., "Electrostatic Discharge (ESD) Sensitivity of a Selected Number of Solid Rocket Propellants," 1987 JANNAF Propulsion Systems Hazards Subcommittee Meeting, Huntsville, AL, 30 March - 3 April, 335, Chemical Propulsion Information Agency Publication 464.

9. Covino, J., Hudson, F. E., and Wu, F., "NWC Electrostatic Discharge Evaluation Methodology Applied to Inert Propellants," 1988 JANNAF Propulsion Systems Hazards Subcommittee Meeting, Los Angeles, CA, 28-30 March, 223, Chemical Propulsion Information Agency Publication 477.

10. Raun, R. L., "Computer Model of ESD-Induced Ignition," 1991 JANNAF Propulsion Systems Hazards Subcommittee Meeting, Albuquerque, NM, 18-22 March, 101, Chemical Propulsion Information Agency Publication 562.

11. McHugh, S. "A Simple Computational Model to Describe Interactions Between Combustion and Mechanical Deformation in an ESD Event," 1992 Propulsion Systems Hazards Subcommittee Meeting, Silver Spring, MD, 27 April - 1 May, 71, Chemical Propulsion Information Agency Publication 582, Vol. 1.

12. Mellor, A. M. and Stoops, D. R. "Optimization of Spark and ESD Sensitivity Tests," 1988 JANNAF Propulsion Systems Hazards Subcommittee Meeting, Los Angeles, CA 28-30 March, 213, Chemical Propulsion Information Agency, Publication 477, Vol. 1.

13. Raun, R. L., "Effect of Energy Density Assumptions on Computer Simulations of Breakdown-Induced Ignition," 1992 JANNAF Propulsion Systems Hazards Subcommittee Meeting, Silver Spring, MD, 27 April - 1 May, 105, Chemical Propulsion Information Agency Publication 582, Vol. 1.

14. Peters, J. E. and Mellor A. M., "An Ignition Model for Liquid Fuel Sprays," Comb. Flame, 38 (1980) 65.

15. Rich, J. T., McDonald, J. P., Mellor, A. M. "Characteristic Time Modeling of Ignition of Solid Rocket Propellant by Electrostatic Discharge," 1994 JANNAF Propulsion Systems Hazards Subcommittee Meeting, San Diego, CA, 1-4 August, 165, Chemical Propulsion Information Agency Publication 615, Vol. 1.

16. Isom, K. B. and Speed, T. C., "Electrostatic Discharge Effects on Propellant, Observations From Post Test Examination," 1987 JANNAF Propulsion Meeting, Huntsvile, AL, 30 March - 3 April, 415, Chemical Propulsion Information Agency Publication 480, Vol. 1.

17. Hermance, C. E., "A Model of Propellant Combustion Including Surface Heterogeneity and Heat Generation," AIAA J., 4 (1966) 1629.

18. Lee, R. J., Tasker, D. G., Forbes, J. W., Beard B. C., and Sharma, J., "Shock Ignition of an Explosive Due to Electrostatic Discharge (ESD)," Shock Compression in Condensed Matter edited by S. C. Schmidt, 729. Elsevier Science Publishers, Amsterdam and New York, 1989.

19. Lee, R. J., Tasker, D. G., Forbes, J. W., "Shock Ignition of an Explosive due to Electrostatic Discharge (ESD)," 1990 JANNAF Propulsion Systems Hazards Subcommittee Meeting, Laurel MD 3-5 April, 291, Chemical Propulsion Information Agency Publication 538, Vol 1.

20. Walker, F. E. and Wasley, R., "A General Model for the Shock Initiation of Explosives," Propellants and Explosives 1 (1976) 73.

21. Liddiard T. P. and Forbes, J. W., "A Summary Report of the Modified Gap Test and the Underwater Sensitivity Test," Naval Surface Warfare Center, NSWC TR 86-350, 1987.

22. Duvall, G. E. and Fowles, G. R., "Shock Waves," High Pressure Physics And Chemistry Vol. 2, edited by R. S. Bradley, Academic Press, New York, 1953.

23. Tucker, T. J., Allensworth, D. L., and Kennedy, J. E., A Study Of ZPCP Spark Detonators, Sandia National Laboratory, Albuquerque, NM, Research Report SC-RR-70-625, 1970.

24. Tucker, T. J., Kennedy, J. E., and Allensworth, D. L., "Secondary Explosive Spark Detonators," Seventh Symposium on Explosives and Pyrotechnics, Franklin Institute, 1971.

25. Lee, R. J. and Tasker, D. G., "The Acquisition of Definitive ESD Sensitivity Data and a New Test Method," 1987 JANNAF Propulsion Systems Hazards Subcommittee Meeting, Huntsville, AL, 30 March - 3 April, 319-325. Chemical Propulsion Information Agency Publication 480, Vol. 1.

26. Graham, R. A., Bauer, F. Lee, L. M. Reed, R. P., "Standardized Bauer Piezoelectric Polymer Shock Gauge," Shock Wave Compression of Condensed Matter, edited by S. C. Schmidt, Elsevier Science Publishers, Amsterdam and New York, 47-50, 1987.

27. Moore, L. M., Graham, R. A., Reed, R. P., Anderson, M. U., Lee, L. M., Horine, F. M., Bauer, F., Warren, T. W. "PVDF Gauge Applications," PVDF Shock Sensor Workshop Proceedings, Albuquerque NM, 145-178, Sandia National Laboratories, 1990.

28. Lengelle, G., Fourest, B., Godon, J. C., Guin, C. "Condensed-Phase Behavior and Ablation Rate of Fuels for Hybrid Propulsion," AIAA J., (1993) 1-14.

29. Bourham, M., North Carolina State University, Raliegh NC. (private communication), 1996.

30. McGuire, R. R. and Tarver, C. M., "Chemical Decomposition Models for the Thermal Explosion of Confined HMX, TATB, RDX, and TNT Explosives," Proceedings Seventh Symposium (International) on Detonation, Annapolis, MD, 16-19 June, 56-64. Naval Surface Warfare Center. MP 82-334, 1981.

31. Tarver, C. M., Lawrence Livermore Laboratory, Livermore, CA. (private communications), 1996.

32. Jacobs, P. W. M. and Whitehead, H. M. "Decomposition and Combustion of Ammonium Perchlorate," Chemical Review, 69 (1969) 551-590.

33. Hills, M.E. and McBride, W. R., Spectral Transmittance of Single Crystal Ammonium Perchlorate and Deuterated Ammonium Perchlorate, Naval Weapons Center, China Lake, CA NWC TP 5683, 1974.

34. Brill, T. B. and Ariswa, H., "Flash Pyrolysis of Hydroxyl-Terminated Polybutadiene (HTPB) I: Analysis and Implications of the Gaseous Products," To be published in Combustion and Flame, 1996.

35. White, K. J., Katulka, G. L., and Driesen, S., "Electro-Thermal Chemical Plasma Interaction with Propellants," 32nd JANNAF Combustion Subcommittee Meeting, Huntsville, AL, 23-27 October, 113-122. Chemical Propulsion Information Agency Publication 631, Vol 1., 1995.

36. Farmer, R. C., SECA Incorporated, 3313 Bob Wallace Avenue, Suite 202, Huntsville Alabama. (private communication), 1996.

37. Gordon, S., and McBride, B., Computer Program for Calculation of Complex Chemical Equilibrium Compositions, Lewis Research Center, Cincinnati, OH, NASA SP-273, 1971.

38. Baroody, E. and Peters, S., Heat of Explosion, Heat of Detonation, and Reaction Products: Their Estimation and Relation to the First Law of Thermodynamics, Indian Head MD: Naval Ordnance Station. IHTR-1340, 1990.

39. Oxley, J. C., Kaushik, S. M., and Gilson, N. S., "Ammonium Perchlorate Thermal Stability in the Presence of Hydrocarbons," Response of Ammonium Perchlorate to Thermal and Mechanical Shock Stimuli, edited by T. L. Boggs, Naval Weapons Center, China Lake, CA, NWC TP 7053, 1990.

40. Skinner, D., Olson, D., and Block-Bolten, A. "Electrostatic Discharge Ignition of Energetic Materials," Submitted to Propellants, Explosives, and Pyrotechnics, 1996.

41. Price, F. C. "The Modeling of Deflagration-to-Detonation Transition of (1) ammonium Perchlorate (2) Ammonium Perchlorate and Methane," Response of Ammonium Perchlorate to Thermal and Mechanical Shock Stimuli, edited by T. L. Boggs. Naval Weapons Cetner, China Lake, CA, NWC TP 7053, 1990.

42. Atwood, A. I., Price, C. F., Curran, P. O., and Zwierzchowski, N. G., "Ignition and Burn Rate Properties of Ammonium Perchlorate," Response of Ammonium Perchlorate to Thermal and Mechanical Shock Stimuli, edited by T. L. Boggs, China Lake, CA: Naval Weapons Center. NWC, TP-7053, 1990.

43. Brewster, M. Q. and Hardt, B. E., "Selective Radiation Absorption in Aluminized Composite Propellant Combustion" 24th JANNAF Combustion Meeting, Monterey, CA, Chemical Propulsion Information Agency, 157-163, 1987.

44. Braginskii, S. I., "Theory of the Development of a Spark Channel," JETP 34(7) (1958) 1068.

45. Drabkina, S. I, "The Theory of the Development of the Channel of the Spark Discharge," J. Exptl. Theoret. Phys. (U.S.S.R.), 21 (1951) 473.

46. Andreev, S. I., Vanykov, M. P., and Kotolov, A. B., "Growth of the Spark Discharge Canal for A Discharge Circuit with a Rapidly Increasing Current," Sov. Phys. Tech. Phys., 7(1), (1962) 37.

47. Martin, T. H., Seamen, J. F., and Jobe, D. O., "Energy Losses in Switches," Proceeding of the IEEE Pulse Power Conference, Albuquerque, NM, 463, 1993.

48. Andreev, S. I. and Orlov, B. L., "Development of a Spark Discharge I," Sov. Phys. Tech. Phys., 10(8), (1966) 1097.

49. Frank-Kamenetskii, D. A., Diffusion and Heat Transfer in Chemical Kinetics, 2nd edition, Plenum Press, New York, 1969.

50. Robertson, J. B. "The Thermal Decomposition of Explosives, Part I, Ethylenedinitramine and Tetryl," Trans. Faraday Soc., 44 (1948) 677.

51. Robertson, J. B. "The Thermal Decomposition of Explosives, Part II," Cyclotrimethylenetrinitramine and Cyclotetramethylenetetranitramine," Trans. Faraday Soc. 45 (1949) 85.

52. Robertson, J. B. "The Decomposition, Boiling and Explosion of Trinitrotoluene at High Temperatures," Trans. Faraday Soc. 45 (1949) 977.

53. Rogers, R. N. "Differential Scanning Calorimetric Determination of Kinetics Constants of Systems That Melt With Decomposition," Thermochimica Acta 3 (1972) 437.

54. Rogers, R. N. "Simplified Determination of Rate Constants by Scanning Calorimetry," Analytical Chemistry 44(7) (1972) 1336.

55. Henkin, H. and McGill, R., "Rates of Explosive Decomposition of Explosives," Indust. Eng. Chem., 44 (1952) 1391.

56. Wenograd, J. "The Behavior of Explosives at Very High Temperatures," Trans. Farad. Soc. 57 (1961) 1612.

57. Lee, E. L., Sanborn, R. H., and Stromberg, H. D., "Thermal Decomposition of High Explosives at Static Pressures 10-50 Kilobars," Proceedings of the Fifth Symposium (International) on Detonation, Pasadena, CA 18-21 August, 331, Office of Naval Research, ACR-184, 1970.

58. Lisitskii, V. I. and Merzhanov, A. G., Combustion, Explosion, and Shock Waves 2 (1965) 62.

59. Zinn, J., and Rogers, R. N. "Thermal Initiation of Explosives," J. Phys. Chem., 66 (1962) 2646.

60. Brill, T. B., and Brush, P. J., "Chemical Phenomena Associated with the Initiation of Thermal Explosions," Ninth Symposium (International) on Detonation, Portland, OR, 28 August - 1 September, 228, Office of the Chief of Naval Research, OCNR 113291-7, 1989.

61. McGuire, R. R. and Tarver, C. M., "Chemical Decomposition Models for the Thermal Explosion of Confined HMX, TATB, RDX, and TNT Explosives," Proceedings Seventh Symposium (International) on Detonation, Annapolis, MD, 16-19 June, 56-64. Naval Surface Warfare Center. MP 82-334, 1981.

62. Zinn, J., and Mader, C. L., "Thermal Initiation of Explosives," J. Appl. Phys., 31(2) (1960) 323.

63. Rogers, R. N. "Thermochemistry of Explosives," Thermochimica Acta 11 (1975)131.

64. Tarver, C. M., McGuire, R. R., Wrenn, E. W., and Brein, K. R. "The Thermal Decomposition of Explosives with Full Containment in One-Dimensional Geometries," The Seventh Combustion Symposium, Leeds, England, 1978.

65. Schrader, M. A., Leeuw, M. W., van der Steen, A. C., "The Thermal Step Test: A Key to High Temperature Behavior of Explosives," Proceedings of the Ninth International Pyrotechnic Seminar, Colorado Springs, CA, 881, 1984.

DISTRIBUTION

ADMINISTRATOR
DEFENSE TECH INFO CTR
ATTN DTIC-OCP
8725 JOHN J KINGMAN RD STE 0944
FT BELVOIR VA 22060-6218   1

DIRECTOR
DEFENSE NUCLEAR AGENCY
ATTN TECHNICAL LIBRARY
WASHINGTON DC 20305   1

DODESB
ATTN DDESB KT
HOFFMAN BUILDING 1
2461 EISENHOWER AVENUE
ALEXANDRIA VA 22331-0600   1

COMMANDING OFFICER
NAVAL RESEARCH LABORATORY
ATTN TECHNICAL LIBRARY
WASHINGTON DC 20350-5000   1

OFFICE OF THE CHIEF OF NAVAL RESEARCH
ATTN ONR 333 (R MILLER)
800 QUINCY ST BCT1
ARLINGTON VA 22217-5000   1

OFFICE OF THE CHIEF OF NAVAL RESEARCH
ATTN ONR 351 (D SIEGEL)
800 QUINCY ST BCT1
ARLINGTON VA 22217-5000   1

OFFICE OF THE CHIEF OF NAVAL RESEARCH
ATTN ONR 333 (J GOLDWASSER)
800 QUINCY ST BCT1
ARLINGTON VA 22217-5000   1

COMMANDER
NAVAL AIR SYSTEMS COMMAND
ATTN TECHNICAL LIBRARY
1421 JEFFERSON DRIVE
ARLINGTON VA 22243   1

COMMANDER
SPACE AND NAVAL WARFARE SYS COM
ATTN SPAWAR 05
WASHINGTON DC 20363-5100   1

JHU/CPIA
ATTN SECURITY OFFICER
10630 LITTLE PATUXENT PKWY STE 202
COLUMBIA MD 21044-3200   1

COMMANDER
NAVAL SURFACE WARFARE CENTER
ATTN TECHNICAL LIBRARY
CARDEROCK DIVISION
BETHESDA MD 20084-5000   1

COMMANDER
NAVAL UNDERWATER WARFARE CTR DIV
ATTN TECHNICAL LIBRARY
NEWPORT RI 02841-5047   1

COMMANDER
NAVAL AIR WARFARE WEAPONS DIV
ATTN CODE C27A (S DEMAY)
CHINA LAKE CA 93555-6001   1

COMMANDER
NAVAL AIR WARFARE WEAPONS DIV
ATTN CODE C2713 (H JOHN)
CHINA LAKE CA 93555-6001   1

COMMANDER
NAVAL AIR WARFARE WEAPONS DIV
ATTN CODE C0239 (T BOGGS)
CHINA LAKE CA 93555-6001   1

COMMANDER
NAVAL AIR WARFARE WEAPONS DIV
ATTN CODE 474330D (J DAVIS)
CHINA LAKE CA 93555-6001   1

COMMANDER
NAVAL AIR WARFARE WEAPONS DIV
ATTN CODE 47340D (D WOODY)
CHINA LAKE CA 93555-6001   1

COMMANDER
NAVAL AIR WARFARE WEAPONS DIV
ATTN CODE 474330D (P MILLER)
CHINA LAKE CA 93555-6001   1

COMMANDER
NAVAL SURFACE WARFARE CENTER
ATTN LIBRARY
DAHLGREN VA 22448-5000   1

COMMANDER
NAVAL AND COMMAND CONTROL OCEAN
   SURVEILLANCE CENTER
ATTN TECHNICAL LIBRARY
SAN DIEGO CA 92152-5000   1

SUPERINTENDENT
NAVAL POSTGRADUATE SCHOOL
ATTN LIBRARY
MONTEREY CA 93940   1

PRESIDENT
NAVAL WAR COLLEGE
ATTN TECHNICAL LIBRARY
NEEWPOER RI 02841   1

COMMANDER
AF OFC OF SCIENTIFIC RESEARCH
BOLLING AIR FORCE BASE
ATTN T MATUSKO
WASHINGTON DC 20332   1

COMMANDER
AIR FORCE ASTRONAUTICS LAB
ATAL MKPL
ATTN C MERRILL
EDWARDS AFB CA 93521   1

COMMANDER
AIR FORCE ASTRONAUTICS LAB
ATAL MKPL
ATTN F ROBERTO
EDWARDS AFB CA 93521   1

DEPT OF INTERIOR BUREAU OF MINES
PITTSBURG RESEARCH CENTER
ATTN R WATSON
COCHRANS MILL ROAD
PITTSBURGH PA 15236-0070   1

COMMANDER
AFATL MN
ATTN WL MNME (S AUBERT)
EGLIN AFB FL 32542-5434   1

UNIVERSITY OF CALIFORNIA
LAWRENCE LIVERMORE NATIONAL LAB
ATTN J FORBES (L-282)
PO BOX 808
LIVERMORE CA 94550   3

UNIVERSITY OF CALIFORNIA
LAWRENCE LIVERMORE NATIONAL LAB
ATTN A NICHOLS
PO BOX 808
LIVERMORE CA 94550   1

UNIVERSITY OF CALIFORNIA
LAWRENCE LIVERMORE NATIONAL LAB
ATTN C TARVER
PO BOX 808
LIVERMORE CA 94550   1

SANDIA NATIONAL LABORATORY
ATTN DARLENE M LOLL FOR
   TECHNICAL LIBRARY
PO BOX 969
LIVERMORE CA 94550-0096   1

APPLIED RESEARCH LABORATORY
PENNSYLVANIA STATE UNIVERSITY
ATTN LIBRARIAN
PO BOX 30 UNIVERSITY PARK
STATE COLLEGE PA 16804   1

LOS ALAMOS NATIONAL LABORATORY
ATTN B ASAY
PO BOX 1663
LOS ALAMOS NM 87545   1

LOS ALAMOS NATIONAL LABORATORY
ATTN J BDZIL
PO BOX 1663
LOS ALAMOS NM 87545   1

LOS ALAMOS NATIONAL LABORATORY
ATTN J GOFORTH
PO BOX 1663
LOS ALAMOS NM 87545   1

LOS ALAMOS NATIONAL LABORATORY
ATTN S SHEFFIELD
PO BOX 1663
LOS ALAMOS NM 87545   1

NEW MEXICO INSTITUTE OF
  MINING TECHNOLOGY
ATTN DOUG OLSON
CAMPUS STATION
SOCORRO NM 87801   1

NEW MEXICO INSTITUTE OF
  MINING TECHNOLOGY
ATTN V S JOSHI
CAMPUS STATION
SOCORRO NM 87801   1

NEW MEXICO INSTITUTE OF
  MINING TECHNOLOGY
ATTN P PERSSON
CAMPUS STATION
SOCORRO NM 87801   2

ALLIANT TECH SYSTEMS
BACCHUS WORKS
ATTN M KLAKKEN
MAGNA UT 84044   1

ALLIANT TECH SYSTEMS
BACCHUS WORKS
ATTN L LOSEE
MAGNA UT 84044   1

LOCKHEED MISSILES & SPACE CO
ATTN R HODGES
PO BOX 504
SUNNYVALE CA 94086   1

S CUBED
A DIVISION OF MAXWELL LABS INC
ATTN R SEDGWICK
PO BOX 1620
LAJOLLA CA 92038   1

SRI INTERATIONAL
ATTN M COWPERTHAWAITE
333 RAVENSWOOD AVENUE
MENLO PARK CA 94025   1

VANDERBILT UNIVERSITY
ATTN A MELLOR
NASHVILLE TN 37235   1

ENIG ASSOCIATES INC
ATTN J ENIG
SUITE 500
11120 NEW HAMPSHIRE AVENUE
SILVER SPRING MD 20904-2633   1

Internal:

041	1
590D (F VALENTA)	1
8430	1
840L	3
TDE (S MITCHELL)	1
920	1
920C1 (R BERNECKER)	1
920C3 (C COFFEY)	1
9210 (R GUIRGUIS)	1
9210 (H JONES)	1
9210 (F ZERILLI)	1
9220 (RICHARD LEE)	1
9220 (D TASKER)	1
9220 (W WALTON)	1
9220 (W WILSON)	3
9230 (R BAKER)	1
9230 (G CHAMBERS)	1
9230 (R DOHERTY)	5
9230 (H SANDUSKY)	1
9230 (G SUTHERLAND)	1
9240 (B GLANCY)	1
9240 (P GUSTAVSON)	1
9240 (C RICHMOND)	1
9240 (R LEMAR)	1
950 (M SWISDAK)	1
950 (L MONTESI)	1
952 (J LAIB)	1